UNIVERSITY OF CALIFORNIA
RIVERSIDE

# Renormalization Group Analysis of 2+1D Quantum XY Model With Dissipation

A Dissertation submitted in partial satisfaction
of the requirements for the degree of

Doctor of Philosophy

in

Physics

by

Changtao Hou

June 2016

Dissertation Committee:

Dr. Chandra M. Varma, Chairperson
Dr. Vivek Aji
Dr. Shan-Wen Tsai

The Dissertation of Changtao Hou is approved:

---

---

---

Committee Chairperson

University of California, Riverside

## Acknowledgments

Firstly, I would like to thank Professor Chandra Varma for his supervision during these four years of PhD studies. Among his many qualities as a supervisor, I wish to point out his readiness to take off time to guide his students and enthusiastic pursuit of solutions to our problems. His way of thinking problems inspired me to see through the appearance to perceive the essence.

I would also like to express my sincere gratitude to Professor Vivek Aji, and Professor Shan-Wen Tsai for their willingness to serve on the evaluation committee for this thesis as well as on my defence 26 May 2016.

Furthermore, I am grateful to Professor Vivek Aji for very fruitful discussion on parts of this thesis work. The person I have worked most closely with these years is Dr. Lijun Zhu, and I thank him for a most grateful help and discussion. Lijun gave me a much needed crash course in Monte Carlo simulations and and I have also profited from continued use of some of his scripts. At the same time, I may also use this opportunity to thank Ph.D. students Yanmeng Shi and Chi Tang for discussion of experiments and Shanshan Su for reading my thesis.

Finally, special mention must go to my parents and my wife.

# ABSTRACT OF THE DISSERTATION

Renormalization Group Analysis of 2+1D Quantum XY Model With Dissipation

by

Changtao Hou

Doctor of Philosophy, Graduate Program in Physics
University of California, Riverside, June 2016
Dr. Chandra M. Varma, Chairperson

This thesis present the recently theoretical and numerical results on 2D dissipative quantum XY model. The two-dimensional quantum XY model is applicable to the quantum critical properties of several experimental systems, such as superconductor to insulator transitions, ferromagnetic and antiferromagnetic transitions in metals, and loop current order transition in the cuprates. Renormalization group methods are applied to solve the reformulated action of the original model in terms of two type topological excitations: vortices and warps. The calculations explain the extraordinary properties of the model studied through quantum Monte Carlo simulations: the separability of the correlation function in space and time, the correlation length in space proportional to logarithm of the correlation length in time near the transition from disordered phase to ordered phase. The running dynamical critical exponent is introduced to address the anisotropy between time and space. The effects of anisotropy fields have been examined through renormalization group method. The transition from disordered phase to ordered phase of this model has been studied by quantum Monte Carlo. The divergence of temporal correlation length in function of $(K_c - K)/K_c$ is

examined by numerical simulation. The logarithmic relation between temporal correlation length and spacial correlation length is further confirmed. Also, the same logarithmic relation for different correlation function with different space separation is found and implicitly confirmed the separability of correlation function in space and time.

# Contents

# List of Figures

# List of Tables

# Chapter 1

# Introduction

Superconductivity is a phenomenon of a material to sustain a dissipationless current and expel of magnetic fields when cooled below a critical temperature, $T_c$. It was first discovered by Heike Kammerlingh-Onnes in 1911[29]. It wasn't until 1957 that, Bardeen, Cooper, and Schrieffer (BCS)[8] proposed a microscopic theory for understanding this new phase of matter. The BCS theory explained superconducting as the condensation of Cooper pairs, which are pairs of electrons interacting through the exchange of phonons. Until 1986, physicists had believed that BCS theory forbade superconductivity at temperatures above about 30K, which is called McMillan's limit[37]. In that year, Bednorz and Müller[10] discovered superconductivity in a lanthanum-based cuprate material, which had a transition temperature of 35K. It was soon found that in $YBCO$ the critical temperature could be raised to 92K. The high temperature superconductivity demonstrates that the standard BCS theory might have shortcomings in explaining this new class of materials. It is one of the major challenges of theoretical condensed matter physics to explain such phenomenon.

The key clue to understand this problem lies in the common phase diagram and similarity structure of different materials.

## 1.1 Phase Diagram of Cuprates

FiG.1.1(a) shows a unit cell of $YBa_2Cu_3O_7$(YBCO), the first high-$T_c$ superconductor. The unit cell of YBCO consists of three pseudocubic perovskite unit cells. Each perovskite unit cell contains a Y or Ba atom at the center. All corner sites of the unit cell are occupied by Cu, and there are fours possible crystallographic sites for oxygen. One of the key features of the YBCO unit cell is the presence of two layers of $CuO_2$. In YBCO, the Cu-O plane is known to play an important role for high temperature superconductivity. When doping $x \approx 0.15$(refer as optimal doping), $T_c$ in YBCO is maximal. Other cuprate superconductors have similar crystal structures and $CuO_2$ planes. FIG.1.1(b) shows the common two-dimensional layer $CuO_2$ in cuprates high-$T_c$ superconductors materials.

Besides the common crystal structure and $CuO_2$ plane, hole-doped cuprates also share the generic phase diagram. The generic phase diagram is generated by tuning temperature and doping, which is controlled by chemical substitution in the charge reservoirs. In FIG.1.2, we show a typical phase diagram of hole-doped cuprates. The x-axis represents the doping level and the y-axis represents the temperature. Starting at zero doping and low temperature, the system is a strongly correlated insulating antiferromagnetic(AF) in which neighboring Cu spins are oppositely aligned up to a Néel-temperature of $\sim 300K$. When holes are introduced into the cuprate plane, the AF state is depressed and is destroyed completely at $x \sim 0.02$. Subsequently, the superconducting(SC) state is developed at low

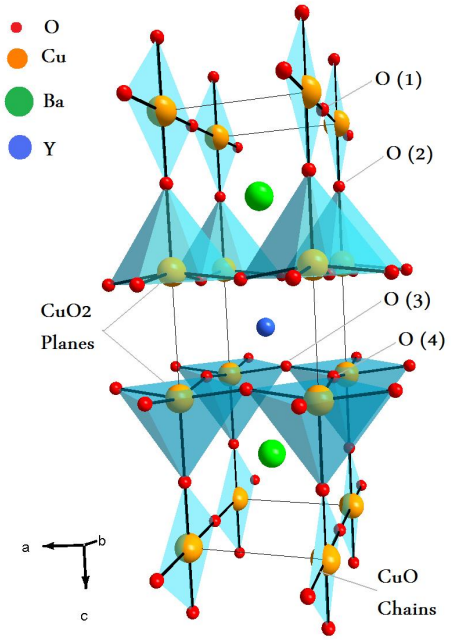


(a) YBCO unit cell

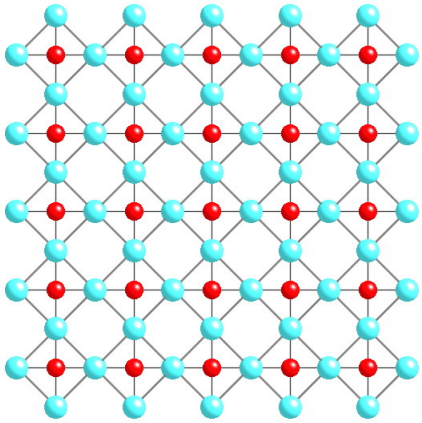

(b) $CuO_2$ plane

Figure 1.1: Crystal structure for the first high-$T_c$ superconductor and the common $CuO_2$ plane in cuprates. (a). A unit cell of YBCO. Y and Ba are stacked in the sequency [Ba-Y-Ba] along the c-axis. Cu occupy corner sites, Cu(1) and Cu(2) in the figure, with respect the oxygen. The role of Y plane is to serve as spacer between two $CuO_2$ planes. (b). $CuO_2$ plane. The light blue sphere represent oxygen and red sphere represent copper.

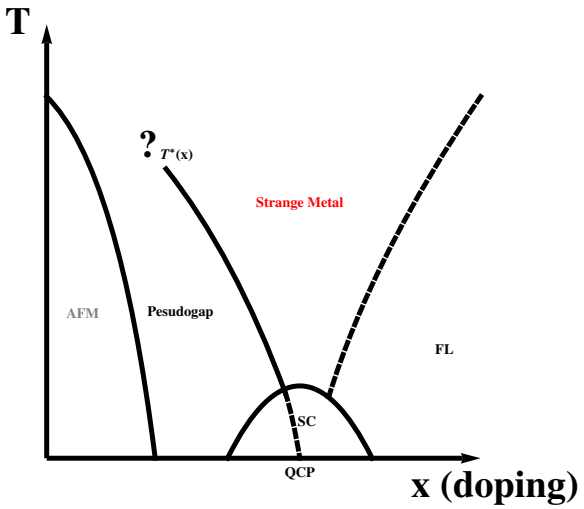


Figure 1.2: Schematic phase-diagram of cuprates on hole-doping side($x > 0$). AF, SC, and FL denotes the antiferromagnetic, superconductivity, and Fermi liquid phase, respectively. The pseudogap line $T^*$ is conjectured to continue into the SC state and terminate at $T = 0$ quantum critical point(QCP). The question mark denotes that how the $T^*$ line will end for zero doping has not been determined.

temperature. The critical temperature reaches its maximum at optimal doping, and the regions to the left and to the right are called under-doped and over-doped, respectively. The under-doped region at non-zero temperature is called the pseudogap region. This region holds several unusual properties and has been the focus of many experiments and theories. Above the superconducting dome is the strange metal (or marginal Fermi liquid) region. At high doping levels, the system can be described by the Fermi liquid theory, which correspond to Fermi liquid(FL) state. The line separating the strange metal region and the Fermi liquid region is believed to be a cross-over line Because of this, the properties change gradually between these two regions.

## 1.2 Marginal Fermi Liquid

At intermediate doping above the critical temperature, one finds the strange metal region. The transport properties[22, 49, 23] in this particular region differ from what is predicted by Fermi liquid theory, and the thermodynamic properties are more similar to those of the Fermi liquids. This metallic state also seems to have a Fermi surface, but it is marginal in the sense that the quasiparticle weight goes to zero logarithmically. One of the anomalies in the transport properties is the linear resistivity $\rho$ above $T_c$, implying a deviant scattering of the charge carries, which contradicts the Fermi liquid theory prediction of $\rho \propto T^2$.

In 1989, Varma proposed the marginal Fermi liquid hypothesis[55], which could explain the transport experiments and possibly the superconductivity at low temperatures. The basic assumption is that the electrons are scattering off a particular kind of bosonic fluctuation spectrum where the energy scale is set only by temperature,

$$-\mathrm{Im}\chi(\boldsymbol{q},\omega,T) \propto \begin{cases} \omega/T & \omega \ll T \\ \text{const} & \omega \ll T \ll \omega_c \end{cases} \tag{1.1}$$

Here $\omega_c$ is a cut-off frequency to be specified by experiments, $T$ is temperature, $\boldsymbol{q}$ is momentum, and $\omega$ is the frequency. The quasiparticle weight can be calculated from these fluctuations, which is given by[55] $z(\omega)^{-1} = [1 - \partial\Sigma_R/\partial\omega] \propto \ln|\omega_c/\omega|$, where $\Sigma_R$ is the real part of the electron self-energy. The proposed fluctuation spectrum causes $z(\omega)$ to vanish logarithmically at the Fermi surface. Also, the fluctuation spectrum is momentum independent, implying the spatial locality of the fluctuations. This kind of fluctuation spectrum suffices to explain all anomalous transport properties of the strange metal region.

## 1.3 Loop Current Model

In the under-doped and decreased temperature region, the material reaches pseudogap phase[50, 19, 58, 43, 44], which is characterized by the opening of a highly anisotropic excitation gap. That is, below the temperature $T^*$ but above the critical temperature $T_c$, there are regions in the momentum space where gapless excitations exist and other regions where the excitations are gapped. The are two classes of theories to explain the origin of this gap. One is that it is associated with a precursor state of superconductivity where Cooper pairs are formed but do not have global phase coherence. Alternatively, it could be associated with another form of order that is distinct from superconductivity. If the pseudogap line $T^*(x)$ is a phase transition line, it is likely that it terminates at $T = 0$ in a quantum critical point. This thesis mainly focues on this scenario because it could explain strange metal by the fluctuations of the order parameter in the pseudogap state and could also explain the superconducting pairing in terms of quantum critical fluctuations.

Varma[52, 53, 56] proposes that the pseudogap region represents a phase that breaks the time-reversal symmetry through a spontaneous ordering of loop-currents or orbital currents but preserve translation symmetry of the cuprate lattice. In this way, the $T^*(x)$ line represents a true phase transition separating the pseudogap phase, where the loop currents are ordered in a specific pattern, from the strange metal phase, where the loop currents are fluctuating. FIG.1.3 illustrates four possible orientations of the loop current pattern within each unit cell in the psedugap phase. The quantum critical fluctuations in the strange metal phase are the fluctuations of the four possible patterns within each unit cell.

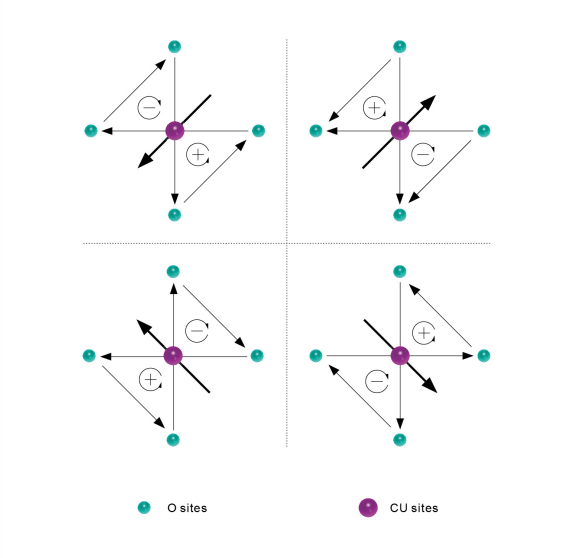


Figure 1.3: The loop current pattern which break time-reversal symmetry spontaneously at $T^*$. The loops are generated by currents running through the copper sites and oxygen sites. The magnetic moments induced by those loop currents are shown as +/-. The arrow located at copper site show the pseudospin that represent those current patterns.

## 1.4 Experiments

The pseudogap phase and the strange metal phase have been extensively studied. Many experiments confirm the prediction of the marginal Fermi liquid theory in the strange metal phase as well as loop currents in the pseudogap phase. In this section, we list some of those key experiments.

### 1.4.1 Polarized Neutron Scattering

In 2004, Mook et el[39] performed a neutron scattering experiment in $YBa_2Cu_3O_{6.45}$ and found the data to be consistent with a small, largely c-axis-directed moment, found below about $200K$. Later in 2006, Frauqué et el[18] used polarized elastic neutron diffraction to give direct evidence of a magnetic order parameter. This order parameter characteries the pseudogap phase in high-$T_c$ cuprates and preserves translations symmetry of the lattice. The symmetry of this unusual magnetic order in cuprates samples corresponds to the expected symmetry of the orbital moments emanating from a loop current state[55, 52, 51]. They studied five different samples—four samples in the underdoped regime and one in the overdoped regime. They found the magnetic intensity increases below a certain temperature, $T_{\text{mag}}$, in the four underdoped samples, whereas no magnetic signal is observed in the overdoped sample. In 2010, Balédent, et al[7] found the magnetic order associated with the pseudogap phase in the archetypal cuprate $La_{2-x}Sr_xCuO_4$(LSCO) system when hole doping $x = 0.085$. Li, et al[34] revealed a fundamental collective magnetic order associated with the pseudogap through inelastic neutron scattering experiment in $HgBa_2CuO_{4+\delta}$. This further confirm the idea of the loop current model in underdoped curprates.

### 1.4.2 Angle-resolved Photoemission Spectroscopy

Angle-resolved photoemission spectroscopy (ARPES)[59], is a direct experimental technique used to observe the distribution of density of single-particle electronic excitations in the reciprocal space of solids. ARPES could give information on the direction, speed and scattering process of valence electrons in the sample being studied. In another sense, both the energy and momentum information of an electron can be obtained from this experiment, resulting in detailed studies of Fermi surface and band dispersion. Kaminski, et al[28] reported that left-circularly polarized photons give a different photocurrent from right-circularly polarized photons in the pseudogap state of $Br_2Sr_2CaCu_2O_{8+\delta}$. This shows that time-reversal symmetry is spontaneously broken below $T^*$, which therefore corresponds to a phase transition. They observed such differences only in the underdoped sample below $T^*$, and not in the overdoped samples. They also showed that, for underdoped samples, the breaking of time-reversal symmetry persists into the superconducting state.

Recently the single-particle self-energies in the pairing and the full lattice symmetry have been deduced directly from the high resolution laser based ARPES data[13] on underdoped and overdoped samples of $Br_2Sr_2CaCu_2O_{8+\delta}$. Jin et al[13] deduced the magnitude and frequency dependence of the effective interactions both in the full symmetry of the lattice $\epsilon_N(\boldsymbol{k},\omega)$ and in the pairing symmetry $\epsilon_p(\boldsymbol{k},\omega)$. Near $T_c$, the attractive interactions $\epsilon_p(\boldsymbol{k},\omega)$ are identical to the repulsive interactions $\epsilon_N(\boldsymbol{k},\omega)$, except for a weak repulsive part near about 50 meV within the experimental uncertainty. Both are independent of $\boldsymbol{k}$ and

their major part is consistent with the quantum-critical fluctuations of the form given by

$$\mathrm{Im}\chi(\boldsymbol{q},\omega,T) = -\chi_0 \tanh(\frac{E}{\sqrt{(2T)^2+\xi_\tau^{-2}}})\frac{1}{\boldsymbol{q}^2+\xi_r^{-2}} \tag{1.2}$$

where $\xi_\tau$ are correlation time and $\xi_r$ are correlation length.

### 1.4.3 Magneto-optic Kerr Effect

The magneto-optic Kerr effect describes the change of the polarization states of light when reflected at a magnetic material. Therefore linearly polarized light experiences a rotation of the polarization plane, called Kerr rotation $\theta_K$. A phase difference between the electric field components perpendicular and parallel to the plane of the incident light occurs as described by the Kerr ellipticity $\epsilon_K$.

A high resolution optical Kerr effect measurements of $YBa_2Cu_3O_{6+x}$ crystals with various hole doping $x$ has been done[62]. Xia et al identified a sharp phase transition at a temperature of $T_s(x)$, below which there is a nonzero Kerr angle of order $\sim 1\mu$rad. This indicates the existence of a phase with broken time reversal symmetry. Also, they found the Kerr effect crosses the superconducting dome to appear below $T_c$ for a near optimally doped sample. Later, Aji, et al[1] give a qualitative explanation based on the loop currents model in the pseudogap region, which further confirm the magnetic order in this regime.

A similar measurement of $Pb_{0.55}Bi_{1.5}Sr_{1.6}La_{0.4}CuO_{6+\delta}$ (Bi2201)[24] has also reported the same Kerr rotation. Furthermore, this experiment confirm the line $T^*$ is coincident with three different measurements—ARPES, polar Kerr effect, and time-resolved reflectivity. The strong and analogous temperature dependences of the ARPES, polar Kerr effect, and time-resolved reflectivity data seen between $T_c$ and $T^*$ are most naturally un-

derstood if $T^*$ is associated with a real phase transition.

## 1.5 Microscopic Model

The experiments evidence strongly support the time-reversal and inversion symmetry breaking order in the pseudogap region and the predictions of the marginal Fermi liquid theory. Aji, et al[2] proposed a microscopic model which generalized the Ashkin-Teller[6] model by including kinetic energy term and dissipation term. The spectrum of the quantum-critical fluctuations of this quantum generalization model is of the same form postulated in 1989 to give the marginal Fermi liquid properties.

The four possible loop current configurations in each unit-cell in FIG.1.3 can be represented by four vectors with arrows representing time reversal symmetry and orientation representing the only plane of reflection symmetry. The Ashkin-Teller model for such a pair of Ising degrees of freedom is:

$$H = -\sum_{\langle i,j\rangle} J_2(\sigma_i\sigma_j + \tau_i\tau_j) + J_4(\sigma_i\tau_i\sigma_j\tau_j) \tag{1.3}$$

where $\sigma_i$ and $\tau_i$ are Ising spins. With the transformation $\cos(\theta_i) = (\sigma_i + \tau_i)/2; \sin(\theta_i) = (\sigma_i - \tau_i)/2$, the Ashkin-Teller model becomes

$$H = \sum_{\langle i,j\rangle} 2J_2\cos(\theta_i - \theta_j) + J_4\cos 2(\theta_i - \theta_j) + h_4\cos 4\theta_i. \tag{1.4}$$

For a quantum theory of the model, two additional terms should be included: the kinetic energy of the $\theta$ variables and the dissipation. Notice that the current between sites $i$ and $j$ is proportional to $(\theta_i - \theta_j)$. The linear couple between this current and the incoherent fermion current and decays of this current into fermion current provide the dissipation for

the collective modes. This process is identical to that derived by Caldeira and Leggett[15] for decay of Josephson currents into incoherent fermion currents. After integrating out the fermion degree of freedoms leads to the Caldeira-Leggett dissipative term in the action of

$$S_{\rm diss} = \frac{\alpha}{2}\int_0^\beta \int_{-\infty}^{\infty} d\tau' \sum_{\langle ij\rangle} \frac{\pi^2}{\beta^2} \frac{[(\theta_i(\tau)-\theta_j(\tau))-(\theta_i(\tau')-\theta_j(\tau'))]^2}{\sin^2(\frac{\pi|\tau-\tau'|}{\beta})} \tag{1.5}$$

where $\alpha = \frac{1}{4\pi^2}\sigma R_q$ with $R_q = h/4e^2$ is the quantum resistance and $\sigma$ is the conductivity between sites.

For $|J_4|/J_2 < 1/2$, $J_4$ is irrelevant and we could start with $J_4 = 0$ for simplicity. The final quantum model is given by

$$\begin{aligned} S &= -2J_2 \sum_{\langle ij\rangle} \int_0^\beta d\tau \cos[\theta_i(\tau)-\theta_j(\tau)] + \frac{C}{2}\sum_i \int_0^\beta d\tau (\frac{d\theta}{d\tau})^2 \\ &+ \frac{\alpha}{2}\int_0^\beta \int_{-\infty}^{\infty} d\tau' \sum_{\langle ij\rangle} \frac{\pi^2}{\beta^2} \frac{[(\theta_i(\tau)-\theta_j(\tau))-(\theta_i(\tau')-\theta_j(\tau'))]^2}{\sin^2(\frac{\pi|\tau-\tau'|}{\beta})} \end{aligned} \tag{1.6}$$

where $C$ serves as the moment of inertia in the kinetic energy term.

# Chapter 2

# Classical and Quantum Phase Transition

Phase transition, especially second-order phase transition(also called continuous phase transition), attracts many physicists work on it. Continuous phase transition are characterized by a divergent susceptibility, an infinite correlation length, and power-law decay correlation function near critical point. There has lots of second-order phase transition example, such as, ferromagnetic transition, superconducting transition, and superfluid transition. In this chapter, we will first discuss classical continuous phase transition. The Landau mean field model will be used as an example to illustrate the critical exponents and scaling hypothesis. Then the renormalization group method will be briefly discussed. In the second part, we will discuss the quantum phase transition and dynamical scaling. The Hertz-Millis-Moriya theory will be mentioned in the last part.

## 2.1 Classical Phase Transition

### 2.1.1 Introduction

Phase transitions are defined as points in the parameter space where the thermodynamic potential becomes non-analytic. Such a non-analytical can arise only in thermodynamic limit, when the size of the system is assumed to be infinite. Macroscopic systems typically contain $\sim 10^{23}$ degrees of freedom, and as such are very close to being in the thermodynamic limit. In many classical phase transitions, we could identify a parameter to distinguish different phases. This parameter will be called order parameter. For example, the average density is the order parameter in liquid-gas transition; superfluid density is the order parameter in superconductor-metal transition; magnetization is the order parameter in ferromagnet-paramagnet transition.

Most phase transitions in nature are discontinuous. But continuous phase transitions attracted most people's attention due to many completely different physical systems share the same properties near the critical point, at which the thermodynamical potential will become non-analytical. The macroscopic properties of a system near a continuous phase transition appear to be independent of the microscopic interactions between particles. It turns out that the macroscopic properties only depend on some characteristics like dimensionality, symmetry, and presence or absence of long-range interactions. The phenomenon of different systems exhibiting the same critical behavior is called universality. We can classify systems into different universality classes according to the critical exponents of their thermodynamical observations near the critical point.

To clarify the basic idea behind continuous phase transition, we will study a very

simple model and calculate critical exponents near the critical point to show that the continuous phase transitions actually have system independent properties.

### 2.1.2 Landau Mean Field Theory

In the following, we study a simple spin model in two dimension. The spin $\boldsymbol{s} = (\cos\theta, \sin\theta)$, in which the amplitude of spin has been fixed to be 1 for simplicity. The order parameter can be defined as

$$\boldsymbol{m} = \frac{1}{v}\sum_i \boldsymbol{s}_i, \tag{2.1}$$

where $v$ is the coarse graining region around a given spin and the summation is defined over all spins in the coarse grain region. By symmetry, the most simplest and nontrivial Hamiltonian for the order parameter one can come up with is the Landau-Ginzburg Hamiltonian:

$$\beta H = \beta F_0 + \int d^2x [\frac{K}{2}(\nabla \boldsymbol{m}(\boldsymbol{x}))^2 + \frac{t}{2}\boldsymbol{m}(\boldsymbol{x})\cdot\boldsymbol{m}(\boldsymbol{x}) + u(\boldsymbol{m}(\boldsymbol{x})\cdot\boldsymbol{m}(\boldsymbol{x}))^2 - \boldsymbol{h}\cdot\boldsymbol{m}(\boldsymbol{x})], \tag{2.2}$$

where $\boldsymbol{h}$ is in-plane magnetic field. The partition function of this Hamiltonian is

$$Z = \int \mathcal{D}\boldsymbol{m}(\boldsymbol{x})\exp\{-\beta H\}. \tag{2.3}$$

The mean field or saddle point solution of this partition function is a uniform magnetization $\boldsymbol{m}$. The corresponding mean field free energy is

$$\beta F = \beta F_0 + V(\frac{t}{2}\boldsymbol{m}^2 + u(\boldsymbol{m}^2)^2 - \boldsymbol{h}\cdot\boldsymbol{m}), \tag{2.4}$$

where $V$ is the volume of the system. The mean filed magnetization satisfy

$$t\boldsymbol{m} + 4u\boldsymbol{m}^2\boldsymbol{m} - \boldsymbol{h} = 0. \tag{2.5}$$

### 2.1.3 Critical Exponent

The solution of $\boldsymbol{m}$ will depend on parameter $t$, $u$, and $h$. Near the critical point, we can expand $t$ in power of $T - T_c$ and the coefficients are determined from experiment. We will have

$$t = a(T - T_c), \tag{2.6}$$

with $a > 0$. $u > 0$ is needed to get a stable solution. Under zero external magnetic field we have a solution for e.q.(2.5)

$$m(h = 0) = \begin{cases} 0 & \text{for } T > T_c \\ \sqrt{\frac{a}{4u}}(T_c - T)^{1/2} & \text{for } T < T_c \end{cases} \tag{2.7}$$

So we get our first universal exponent near the critical point and there is a spontaneous magnetization at low temperature that vanishes with exponent $\beta = 1/2$. At the critical point, $t = 0$, we can get the relation between magnetization and external field,

$$m(T = T_c) = (\frac{h}{4u})^{1/3}, \tag{2.8}$$

i.e. $h \propto m^\delta$ with $\delta = 3$. The static magnetic susceptibility can be derived from eq.(2.5) as

$$\chi = (\frac{\partial m}{\partial h})|_{h=0} = t + 12um^2 = \begin{cases} \frac{1}{t} & \text{for } T > T_c \\ -\frac{1}{2t} & \text{for } T < T_c \end{cases}, \tag{2.9}$$

so $\chi \sim |t|^{-\gamma}$ with $\gamma = 1$. The free energy for $h = 0$ is given by

$$\beta F = \beta F_0 + V \begin{cases} 0 & \text{for } T > T_c \\ -\frac{t^2}{16u} & \text{for } T < T_c \end{cases}. \tag{2.10}$$

From the free energy we can calculate the heat capacity,

$$C(h = 0) = -T\frac{\partial^2 F}{\partial T^2} \approx C_0 + Vk_B a^2 T_c^2 \times \begin{cases} 0 & \text{for } T > T_c \\ \frac{1}{8u} & \text{for } T < T_c \end{cases}. \tag{2.11}$$

It is obvious from the above equation that heat capacity is discontinuous at the critical point and $C \sim |T_c - T|^{-\alpha}$ with $\alpha = 0$. Now we can consider the correlation length of the order parameter. The term $K(\nabla \boldsymbol{m})^2$ is included for this purpose. Expanding $\boldsymbol{m}$ near its mean field solution, $\boldsymbol{m} = \sqrt{\frac{-t}{4u}} + \boldsymbol{\phi}$ for $T < T_c$ and $\boldsymbol{m} = \boldsymbol{\phi}$ for $T > T_c$, we have

$$\beta H = -V\frac{t^2}{16u} + \frac{K}{2}\int d^2x[(\nabla\phi)^2 + \xi^{-2}\phi^2], \tag{2.12}$$

where,

$$\xi^{-2} = \begin{cases} t & \text{for } T > T_c \\ -2t & \text{for } T < T_c \end{cases}. \tag{2.13}$$

Therefore the two-point correlation function is

$$G(\boldsymbol{q}) = < \phi(\boldsymbol{q})\phi(-\boldsymbol{q}) > = \frac{1}{K(q^2 + \xi^{-2})}. \tag{2.14}$$

By using Fourier transformation, we can get

$$G(\boldsymbol{x}) \sim \begin{cases} \frac{1}{x^{(d-1)/2}}\exp(-x/\xi) & \text{for } x \gg \xi \\ \frac{1}{x^{d-2+\eta}} & \text{for } x \ll \xi \end{cases}, \tag{2.15}$$

for d-dimension. If $d = 2$, we have $\eta = 0$. Near the critical point, the correlation function decays as $1/x^{d-2}$. $\xi$ introduced above now has the meaning as correlation length. In the region $x \ll \xi$, the correlation function behaves as a power law function. On the other hand, in the region $x \gg \xi$, the correlation function decays exponentially. From above calculation, we have $\xi \sim \xi_0|t|^{-\nu}$, where $\nu = 1/2$. There is another interesting result which is the integration of correlation function will result in bulk susceptibilities. This is related to fluctuation-dissipation theorem which will not be explored here. In our example, by integrating the correlation function, we will have

$$\chi \propto \int d^2x G(\boldsymbol{x}) \propto \int_0^{\xi} d^2x log(x) \propto \xi^2 \sim t^{-1}, \tag{2.16}$$

which has the same scaling from we got before.

### 2.1.4 Scaling Hypothesis and Renormalization

In the previous section, we derived the critical exponents near the critical point for Landau-Ginzburg model. Since the various thermodynamic quantities are related, the critical exponents can not be independent of each other. The divergence of the correlation length in the vicinity of the critical point implies that the correlation length $\xi$ is the most relevant length scale in the system. It will responses for the singularities of the thermodynamic quantities. The divergence of the correlation length also induces a interesting property of critical system. If we take a snapshot of the critical system and then blow the snapshot up by a factor $\lambda$, the new snapshot will be statistically similar to the old one. This property of the critical system is called self-similarity. The critical behavior is dominated by self-similarity up to the scale $\xi$. By successively eliminating the correlated degrees of freedom of length scale $x \ll \xi$, we could get a relatively simple, uncorrelated degree of freedom at scale $\xi$. This procedure is called renormalization group(RG) and it is a very powerful tool to study both classical and quantum continuous phase transition.

RG normally includes three steps: (1). Coarse graining: In real system, it often has a natural short length cutoff, $a$, which is the lattice constant in condensed matter physics. The first step of RG is to decrease resolution by changing this cutoff to $ba(b > 1)$, which effectively integrates out high energy degrees of freedom. The coarse graining field is defined by

$$m(\boldsymbol{x}) = \frac{1}{b^d} \int_{\text{Cell centered at } \boldsymbol{x}} d^d x' m(\boldsymbol{x}'), \tag{2.17}$$

where $d$ is the dimension of the system.(2). Rescaling: In the second step, we decrease all length scales by factor $b$ to restore original short length cutoff, i.e., set $\boldsymbol{x}_{\text{new}} = \boldsymbol{x}_{\text{old}}/b$. (3). Renormalizing: After rescaling, the new field under the new scale will actually be different from the original fluctuated field. We need to introduce a change of contrast by factor $\zeta$, through defining a renormalized fluctuated field,

$$m_{\text{new}}(\boldsymbol{x}_{\text{new}}) = \frac{1}{\zeta b^d} \int_{\text{Cell centered at } b\boldsymbol{x}_{\text{new}}} d^d x' m(\boldsymbol{x}'). \tag{2.18}$$

After doing the three steps, we will get a new partition function which will look close to the original one but with new coupling constants. This is guaranteed by the self-similarity of the critical system near the critical point.

In essence, the RG is to rescale the system and then observes how the parameters of the system, $t, h$, change if one requires the description of the system in terms of the rescaled parameters to remain unchanged, $t \to t' = b^{y_t} t$, $h \to h' = b^{y_h} h$.

Now we can investigate the consequence of RG steps, i.e.

$$Z = \int \mathcal{D}m \mathrm{e}^{-\beta H(m)} = \int \mathcal{D}m' \mathrm{e}^{-\beta H(m')} = Z'. \tag{2.19}$$

Hence $\ln Z = \ln Z'$, which implies the free energy is related by

$$V f(t, h) = V' f(t', h'). \tag{2.20}$$

In $d$ dimension, the volume of the system is rescaled by a factor of $b^d$, so

$$f(t, h) = b^{-d} f(b^{y_t} t, b^{y_h} h). \tag{2.21}$$

From some simple assumption of the critical system, we could get the a homogenous function form for the free energy of the critical system. Even though we use a very simple to illustrate

the idea of RG, the above procedure can be generalized to very complicated system to get very prominent results.

One can find the relation between different critical exponents from the above scaling form of the free energy. By choosing a rescaling factor $b$ such that $b^{y_t}$ is constant, i.e., $b = t^{-1/y_t}$, we could get

$$f(t,h) = t^{d/y_t} g_f(h/t^{y_h/y_t}). \tag{2.22}$$

From the free energy, we can get heat capacity $C \sim -\frac{\partial^2 f}{\partial t^2} \sim |t|^{d/y_t - 2}$ for $h \to 0$ and magnetization $m(t, h=0) = \frac{\partial f}{\partial h} \sim t^{d/y_t - y_h/y_t}$. Therefore we have

$$\beta = 2 - \alpha - \Delta, \tag{2.23}$$

where $\Delta = y_h/y_t$. $m(t=0,h) \sim |t|^{d/y_t - \Delta}(\frac{h}{|t|^\Delta})^p$ and this limit be should independent of $t$, we must have $p\Delta = d/y_t = 2 - \alpha - \Delta$. Hence

$$\delta = \Delta/(2 - \alpha - \Delta) = \Delta/\beta. \tag{2.24}$$

The susceptibility is computed as $\chi(t,h) \sim \frac{\partial m}{\partial h} \sim |t|^{d/y_t - 2\Delta} g_\chi(h/|t|^\Delta)$, so $\chi(t, h=0) \sim |t|^{d/y_t - 2\Delta}$ and

$$\gamma = 2\Delta - 2 + \alpha. \tag{2.25}$$

Following the same argument, one can get the scaling form for the correlation length $\xi \sim |t|^{-\nu} g(h/|t|^\Delta)$. Closing to the critical point, the correlation length is the most important length scale in the system. Since $\ln Z$ is extensive and dimensionless, it must take the form $\ln Z = (\frac{L}{\xi})^d g_s + \ldots$, where $L$ is the size of system. The leading singular part of free energy then should have the form $f(t,h) \sim \frac{\ln Z}{L^d} \sim \xi^d \sim |t|^{-d\nu} g_f(h/|t|^\Delta)$, which implies

$$d/y_t = 2 - \alpha = d\nu. \tag{2.26}$$

As discussed in the previous section, the correlation function falls off as $G(\boldsymbol{x}) \sim \frac{1}{|\boldsymbol{x}|^{d-2+\eta}}$. The response function can be obtained by integrating correlation function, $\chi \sim \int d^d x G(\boldsymbol{x}) \sim \xi^{2-\eta} \sim |t|^{-\nu(2-\eta)}$, so we get another relation between critical exponent,

$$\gamma = (2-\eta)\nu. \tag{2.27}$$

We can see that there are only two independent critical exponents from above five equations and we derived those relations by only using very simple scaling invariant assumption. In this sense, RG is really helpful to study critical phenomena.

### 2.1.5 Fix Point

As shown in previous section, RG defines a successive transformation in the parameter space, denoted by $\boldsymbol{g}$. From the definition of RG, we could see this transformation, denoted as $R_b$, actually form a semi-group, which does not inverse element.

It could be very complicated to study the general properties of this transformation, but the self-similarity of Hamiltonian must correspond to fixed point $\boldsymbol{g}^*$, such that $R_b \boldsymbol{g}^* = R_b \boldsymbol{g}^*$. Since the correlation length is decreased by $b$ under RG operation, i.e. $\xi(\boldsymbol{g}) = b\xi(R_b \boldsymbol{g})$, the correlation length at a fixed point must be zero or infinity. A fix point with $\xi(\boldsymbol{g}^*) = 0$ describes independent fluctuations at each point and corresponds to complete order, or complete disorder phases. A fix point with $\xi(\boldsymbol{g}^*) = \infty$ describes a critical point, at which the free energy becomes singular. To study the stability of a fix point, we could linearize the RG equations around this fix point,

$$R_b \boldsymbol{g} = R_b(\boldsymbol{g} - \boldsymbol{g}^* + \boldsymbol{g}^*) \approx W_b(\boldsymbol{g} - \boldsymbol{g}^*), \tag{2.28}$$

where $W_b = \frac{\partial R_b}{\partial \boldsymbol{g}}|_{\boldsymbol{g}=\boldsymbol{g}^*}$. Because of the group property,it is easy to see that $R_b R_{b'} = R_{bb'}$.

To explore the properties of the RG flow, we could diagonalize $W$ with eigenvalues $\lambda_\alpha(b)$, and eigenvectors $\phi_\alpha$, $\alpha = 1, 2, \ldots, N$, where $N$ is the number of parameters in the Hamiltonian, i.e., $W_b\phi_\alpha = \lambda_\alpha(b)\phi_\alpha$. The property $R_bR'_b = R_{bb'}$ implies $W_bW'_b = W_{bb'}$. Therefore $\lambda_\alpha(b)\lambda_\alpha(b') = \lambda_\alpha(bb')$. Together with initial condition $\lambda_\alpha(1) = 1$, the above equation implies,

$$\lambda_\alpha(b) = b^{y_\alpha}. \tag{2.29}$$

We can clarify the eigenvalues according to its eigenvalues as following,

(1). If $y_\alpha > 0$, $g_\alpha$ increases under scaling and the corresponding eigenvector is a relevant scaling field.

(2). If $y_\alpha < 0$, $g_\alpha$ decreases under scaling and the corresponding eigenvector is a irrelevant scaling field.

(3). If $y_\alpha = 0$, $g_\alpha$ is invariant under scaling and the corresponding eigenvector is a marginal scaling field.

The distinction of three scaling fields in turn implies a classification of different type of fix points.

(I). Stable fixed points: all the scaling fields are irrelevant or marginal. These points define what we might call stable phases of matter.

(II). Unstable fixed point: all the scaling fields are relevant.

(III). Critical point or critical surface: both relevant and irrelevant scaling fields are exist. At critical point, system will have divergence correlation length. A small deviation from the critical point will lead the system flow to its stable fix point. Therefore critical point is related to the phase transition point in real system.

## 2.2 Quantum Phase Transition

### 2.2.1 Introduction

Quantum phase transition is a phase transition between different quantum phases at zero temperature. Unlike classical phase transition, quantum phases transition only takes place at zero temperature and can only be accessed by tuning a physical parameter. This parameter could be magnetic field, pressure, and doping in the parent compound of a high-$T_c$ superconductor. A typical phase diagram is shown in the figure,

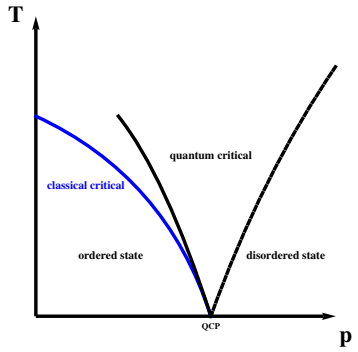


Figure 2.1: Phase diagram of quantum phase transition. QCP denotes the quantum critical point and $p$ is come parameter in the Hamiltonian.

Due to thermal fluctuations will not play any role at zero temperature, the quantum phase transition can only be driven by quantum fluctuations with an energy scaly of $\hbar\omega$. Similar to classical second order phase transition, a continuous quantum phase transition also has a critical point, which is called quantum critical point(QCP). The quantum fluctuations become scale invariant in space and time at the QCP. At finite temperature, quantum fluctuation will compete with thermal fluctuations with energy scale $k_BT$. This competition

will lead much more rich properties in quantum phase transition. For $\hbar\omega > k_B T$, the quantum fluctuation will dominate the system's properties. Even for high temperature, when $p \to p_c$, this condition can still be satisfied, which corresponds the quantum critical region in Fig.2.1. At high enough temperature and far away from QCP, the system is in disorder phase and is purely classical. Around the classical phase transition, the system is governed by thermal fluctuations. There are many system show quantum critical properties.

(1). The Superconductor-insulator transition in two-dimensional thin films by either changing film thickness or magnetic field. This is a very simple example of quantum phase transition.

(2). In High-$T_c$ superconductor, the exotic phase diagram is driven by QCP when tuning doping in the parent compund.

(3). Quantum Hall effect, it is a property of a two-dimensional electron system placed in a strong transverse magnetic field, $B \sim 10T$. As one changing magnetic field under very low temperature, the transverse conductivity $\sigma_{xy}$ becomes quantized $\sigma_{xy} = n\frac{e^2}{h}$, where $n$ is an integer. When varying magnetic field, one can get different $n$ and each corresponds a plateau in transverse conductivity plot or quantum Hall(QH) phase. The universal properties of transition between different QH phases can be captured by quantum phase transition.

### 2.2.2 Quantum-to-classical Mapping

It turns out that many quantum phase transitions can be described as classical transitions with one additional time-like dimension. We start with partition function $Z = \sum_n \langle n|e^{-\beta H}|n\rangle$. Notice that if we identify $\beta \to it$ with $\hbar = 1$, we could treat partition function as time-evolution operator $e^{-iHt}$. In this form, we can write partition function in

the language of Feynman's path-integral formulation. Dividing time into small slice each with length $\delta\tau = \beta/N$, where $N$ is the number of intervals, we have

$$e^{-\beta H} = [e^{-\delta\tau H}]^N, \tag{2.30}$$

and

$$Z = \sum_n \sum_{m_1,m_2,\ldots,m_N} \langle n|e^{-\delta\tau H}|m_1\rangle\langle m_1|e^{-\delta\tau H}|m_2\rangle \ldots \langle m_N|e^{-\delta\tau H}|n\rangle, \tag{2.31}$$

where $\{m_i\}$ are sets of complete states. By transforming partition function in this rather complex form, we can think each term as a transfer matrix and imaginary time as an additional spatial dimension. In essence, we transform the original $d$-dimension problem into a $d+1$ dimension problem. The extra dimension is finite with size $\beta$ in units of $\tau_c = \frac{1}{T_c}$, which is ultra-violet cutoff.

As an example, we consider quantum XY model in two-dimension. The Hamiltonian is,

$$H = \frac{E_c}{2}\sum_i (-i\frac{\partial}{\partial\theta_i})^2 - J\sum_{\langle ij\rangle}\cos(\theta_i - \theta_j), \tag{2.32}$$

where $\langle ij\rangle$ refers nearest neighbor sites. The first term is kinetic energy and the second term is potential energy. We use $T$ and $V$ to denote them, separately. For very small $\delta\tau$, one can make the approximation

$$e^{-\delta\tau H} \approx e^{-\delta\tau T}e^{-\delta\tau V}. \tag{2.33}$$

Inserting a complete set of angular-momentum eigenstates $|\{m_k\}\rangle$(defined by $\langle\theta_k|m_k\rangle = e^{im_k\theta_k}$) can lead the transform matrix take the form,

$$M = \sum_m e^{-\delta\tau/2E_c\sum_k m_k^2} e^{im_k[\theta_k(\tau_{j+1}-\theta_k(\tau_j)]} e^{\delta\tau J\sum_k \cos[\theta_k(\tau_{j+1})-\theta_k(\tau_j)]}. \tag{2.34}$$

By using Poisson summation we have

$$\sum_m e^{-\delta\tau/2E_c\sum_k m_k^2} e^{im_k[\theta_k(\tau_{j+1}-\theta_k(\tau_j)]} = \sqrt{(\pi/\delta\tau E_c)}\sum_n e^{-1/2E_c\delta\tau(\theta+2\pi n)^2}. \tag{2.35}$$

The Villain approximation can be applied to get $e^{1/E_c\delta\tau\cos(\theta)}$. If we choose $\delta\tau = 1/\sqrt{E_c J}$, one could get the equivalent classical three-dimensional XY model,

$$H_{XY} = \frac{1}{K}\sum_{\langle ij\rangle}\cos(\theta_i - \theta_j), \tag{2.36}$$

with $K = \sqrt{J/E_c}$.

### 2.2.3 Dynamical Scaling

The divergence of the correlation length in classical continuous phase transition near the critical points immediately tells us that the correlation length and correlation time will also diverge near QCPs. Besides correlation length, $\xi$, in classical system, one also need introduce correlation length in time direction, denoted as $\xi_\tau$. Generally, at $T = 0$ and as $p \to p_c$, both $\xi$ and $\xi_\tau$ will diverge in the manner,

$$\begin{aligned} \xi &\sim |p - p_c|^{-\nu}, \\ \xi_\tau &\sim \xi^z. \end{aligned} \tag{2.37}$$

Here we introduce dynamical-scaling exponent $z$ to take the anisotropy of time and space into account. For example, in previous section we proved that the quantum 2-$D$ XY model could be mapped to classical 3-$D$ XY model. Therefore $z = 1$ in the quantum 2-$D$ XY model. In general, as pointed out by Hertz[25], the dynamical-scaling exponent $z \neq 1$ near quantum critical points.

The homogeneity hypothesis should also be applied to continuous quantum phase transition if one follows the same renormalization group argument. One needs to be careful about the extra imaginary time dimension because it will not scale exactly the same way as space. First, we consider $T = 0$, which lead the time dimension become infinite $L_\tau = \infty$. Viewed at rescaled length $r' = r/b$ and time $\tau' = \tau/b^z$, the rescaled free energy density will be $f' = b^{d+z} f$. This will give the scaling equation

$$f(t, h) = b^{-(d+z)} f(b^{y_t}|t|, b^{y_h} h), \tag{2.38}$$

where $|t| = |p - p_c|/p_c$ indicates a dimensionless control parameter in the system. Again, we can extract information by choosing $b = t^{-1/y_t}$,

$$f(t, h) = t^{(d+z)/y_t} g_f(h/|t|^{\Delta}), \tag{2.39}$$

with $\Delta = y_h/y_t$. Following the same procedure as in classical phase transition, one could get different critical exponents in terms of the scaling dimensions $y_t$ and $y_h$. The critical exponents, $\alpha$, $\beta$, and $\gamma$ can be written in terms of $y_t$ and $y_h$ as,

$$\begin{aligned} \alpha &= 2 - \frac{d+z}{y_t}, \\ \beta &= \frac{d+z-y_h}{y_t}, \\ \gamma &= \frac{2y_h - d - z}{y_t}. \end{aligned} \tag{2.40}$$

From these equations, one could easily verify that

$$\begin{aligned} \beta &= 2 - \alpha - \Delta, \\ \gamma &= 2\Delta - 2 + \alpha, \\ 2 - \alpha &= (d+z)\nu. \end{aligned} \tag{2.41}$$

We could also generalize the classical correlation function to quantum case to get the scaling form

$$G(r,\tau) = b^{-(d+z-2+\eta)} G(r/b, \tau/b^z), \tag{2.42}$$

where $\eta$ is the anomalous dimension of the correlation function. By choosing scaling factor $b = r$, $b = \tau^{1/z}$, respectively, we could get

$$\begin{aligned} G(r,\tau) &= 1/r^{d+z-2+\eta} \mathcal{G}_1(\tau/r^z), \\ G(r,\tau) &= 1/\tau^{(d+z-2+\eta)/z} \mathcal{G}_2(r/\tau^{1/z}). \end{aligned} \tag{2.43}$$

The susceptibility can be calculated through the correlation function,

$$\chi = \int_0^{L_\tau} d\tau \int_0^L \int d^d r G(r,\tau). \tag{2.44}$$

where $L_\tau = \beta$ and $L$ is the size of system. Near the critical point, we could consider $r \ll \xi$ due to the correlation function is exponential decaying out of this region. Therefore we get

$$\chi \sim \int_0^{L_\tau} d\tau \int_0^L d^d r 1/r^{d+z-2+\eta} \mathcal{G}_1(\tau/r^z). \tag{2.45}$$

By choosing the infinitesimal space-time shells, we could integrate over in such a way that $\tau \propto r^z$. In this way, the scaling function $\mathcal{G}_1(\tau/r^z)$ is constant, and the integral is simplified to

$$\chi \sim \int_0^{\xi} dr r^z r^{d-1} 1/r^{d+z-2+\eta} = \xi^{2-\eta}. \tag{2.46}$$

We can identify another scaling law,

$$\gamma = (2-\eta)\nu. \tag{2.47}$$

### 2.2.4 Finite Size Scaling at $T \neq 0$

As zero temperature cannot be accessed in experiment, we need to understand how to modify the scaling form for $T \neq 0$. Two things could happen for nonzero temperature: first, the quantum phase transition of a system can only happen at zero temperature and its finite-temperature physics is purely classical; second, the transition persists to $T \neq 0$ but crosses over to a different universality class. The 2-$D$ XY model follows this form. At $T = 0$, the QCP for the transition from order to disorder phases is characterized by the exponent of the 3D XY model. However, at $T \neq 0$ the system is effectively two dimensional and undergoes a Kosterlitz-Thoules transition. For $p \to p_c$, there exists a crossover region which separates $k_B T > \hbar\omega$ and $k_B T < \hbar\omega$. So there exists a finite temperate region near QCP in which quantum fluctuate will dominate and this open a door to detect quantum criticality experimentally.

For finite temperature, the extra imaginary time dimension is finite with size $L_\tau = \hbar\beta$. We also know that, near the QCP, the correlation length $\xi$ and correlation time $\xi_\tau$ are only two relevant length scales for the system. Naturally, if $\xi_\tau \sim L_\tau$, the system will know it is effective $d$ dimensional; on the other hand, for $\xi_\tau \ll L_\tau$, the system will effectively know it is in $d+1$ dimension and its characteristic fluctuation frequencies obey $\hbar\omega \gg k_B T$.

The form of the finite size scaling is given by Privman[46]

$$\mathcal{O}(k, \omega, p, T) = L_\tau^{d_\mathcal{O}/z} \mathcal{O}(k L_\tau^{1/z}, \omega L_\tau, L_\tau/\xi_\tau). \tag{2.48}$$

As discuss previously, $L_\tau = \hbar\beta$ defines the size of imaginary time dimension to a characteristic length $\sim L_\tau^{1/z}$, which associate with the temperature. $L$ is the characteristic length

to measure the wave vector k, and $L_\tau$ is the characteristic time to measure frequency $\omega$. The distance to the zero-temperature critical coupling is measured via the ratio of $L_\tau$ to zero-temperature correlation time $\xi_\tau$.

## 2.3 Hertz-Millis-Moriya Theory

The quantum criticality of itinerant ferromagnet has been studied extensively, pioneered by Moriya [40], Hertz [25], Béal-Monod and Maki [9] and by others [38, 11]. None of these could explain the extraordinary resulting in strange metal region of cuprates, in which (1) the correlation function is separated in momentum and frequency, (2) the correlation length in space is proportional to the logarithm of the correlation length in time, this may imply a infinity $z \to \infty$ dynamical critical exponent. This result cannot be obtained by just simply setting $z \to \infty$ in the conventional theories.

In the context of strongly correlated electron systems, one is mainly interested in magnetic phase transitions in metals. The effective action may be derived from the Hamiltonian integral representation by integrating out the electron degrees of freedom [25] or by more conventional techniques [40]. The resulting action could be written as[25, 36]

$$S = \frac{1}{2}\sum_{\boldsymbol{q},\omega}(r_0 + q^2 + \frac{|\omega|}{\gamma(\boldsymbol{q})})|\phi(\boldsymbol{q},\omega)|^2 + u_0\int_0^\beta d\tau d^d r[\phi(\boldsymbol{r},\tau)]^4, \tag{2.49}$$

where $\phi(\boldsymbol{r},\tau)$ is the order parameter after integrating out the itinerate fermion degree of freedom and the second term is the self-interaction of order parameter. The dynamic contribution $|\omega|/\gamma(\boldsymbol{q})$ is the damping of fermions by particle-hole paris excited across the Fermi level. Their phase space increases linearly with $\omega$. For a ferromagnetic transition, $\gamma(\boldsymbol{q}) = v_F q$ as $q \to 0$, i.e., the damping rate diverges due to the abundance of particle-hole

pairs with small momentum. This will lead to a theory with dynamical exponent $z = 3$. For an antiferromagnetic transition, the damping $\gamma(\boldsymbol{q}) \sim \gamma_0$, is independent of $q$, yielding $z = 2$.

The model defined by the action (2.49) has been studied near its critical point using the perturbative RG. To define a RG transformation, one investigates how a change of the cutoff (both in momentum and in frequency) and its subsequent rescaling can be absorbed in a redefinition of the coupling constants. The schema used in Hertz's paper is simultaneously changing the cutoff in momentum space, $\Gamma_q \to \Gamma_q/b$, and frequency space, $\Gamma_\omega \to \Gamma_\omega/b^z$, where dynamical exponent $z$ is introduced to take the anisotropy of scaling in momentum and frequency into account.

The detail of the RG steps is not interesting in this thesis, one could refer to Hertz's[25] and Millis's[38] paper for detail calculations. Over here, the scaling of several thermodynamic quantities are summarized in Table (2.1).

| | d=2,z=2 | d=3,z=2 | d=2,z=3 | d=3,z=3 |
|---|---|---|---|---|
| $\alpha$ | $\ln \ln \frac{1}{T}$ | $T^{1/2}$ | $\ln \frac{1}{T}$ | $T^{1/3}$ |
| $C$ | $T \ln \frac{1}{T}$ | $-T^{3/2}$ | $T^{2/3}$ | $T \ln \frac{1}{T}$ |

Table 2.1: Results for Landau-Guizburg-Wilson quantum critical point in the quantum critical regime $T \gg |r|^{z/2}$. $\alpha$ is the thermal expansion and $C$ is specific heat[36].

The static susceptibility for a ferromagnet is $\chi \approx \chi_0 - DT$ in $d = 2, z = 2$ with nonuniversal constants $\chi_0$ and $D$. $\chi \approx \chi_0 - D'T^{3/2}$ in $d = 3$. For a quantum phase transition driven by a magnetic field $B$, the susceptibility $\chi = \partial M/\partial B = -\partial^2 F/\partial B^2$ has the scaling form $\chi \propto T^{(d+z-2/\nu)/z}$ in the quantum critical regime.

# Chapter 3

# Monte Carlo Simulation

Monte Carlo method is a very useful tool for simulating system with large number of degrees of freedom. In statistical physics, it is very hard to find the exact form of the partition function for most systems. Monte Carlo can be used in studying the phase transition by repeatedly drawing sample with a probability determined by partition function and calculating statistical average based on large samples. By using law of large number, the accuracy of Monte Carlo simulation follows $\sim \frac{1}{\sqrt{N}}$, where $N$ is the number of samples draw by predefined procedure. The Metropolis algorithm is the most popular method to be used to draw samples, which is also the foundation of our implementation of quantum Monte Carlo simulation. This chapter will cover some basics idea of Monte Carlo. Then, two applications of Monte Carlo simulation in real physics systems will be discussed and some novel results will presented.

## 3.1 The basics of Monte Carlo simulations

In statics physics, one of the most important quantities is partition function $Z$,

$$Z = \sum_s \mathrm{e}^{-\beta H(s)} \tag{3.1}$$

where $s$ is possible state and $H(s)$ is the Hamiltonian of the system. Then, the probability of a given state $s$ is given by

$$P(s) = \frac{\mathrm{e}^{-\beta H(s)}}{Z} \tag{3.2}$$

After getting the distribution of state, one could easily calculate the thermal average of any physics quantity by taking average over all states,

$$\langle O \rangle = \sum_{\{s\}} O(s) P(s) \tag{3.3}$$

Here, the Boltzmann factor $P(s)$ acts as a weight factor determining the relative contribution of each configuration to the average. The total number of configurations $|\{s\}|$ will be denoted by $N_{\text{config}}$.

A very straightforward way to calculate the thermal average numerically is by taking a large number of subsample $S \subset \{s\}$ with size $|S| = N$. Then the sample average

$$\bar{O} = \frac{1}{N} \sum_{s \in S} O(s) P(s) \tag{3.4}$$

will be a good estimation of the thermal average of $O$ as long as $N$ is fairly large enough. In practice, however, the number $N_{\text{config}}$ becomes extremelly large even for small system sizes. As a example, for a Ising system with $M$ spins, the total configuration will be $N_{\text{config}} = 2^M$, which grows exponentially with system size. When system is in equilibrium, only states near

equilibrium will have important contribution to the average. The straightforward method will draw many samples with very small contribution, so it is very inefficient. The solution is importance sampling, where the sampled configurations are no longer the uniformly distributed set $S$, but instead a set $S'$ selected according to some chosen distribution. An naturally choosing is the Boltzmann distribution $P(s)$ itself, which will ensure that the dominated configurations will be sampled more often than those only have low weight. If one can generate such subsample $S'$, the estimator reduces to the simple average

$$\bar{O} = \frac{1}{N} \sum_{s \in S'} O(s) \tag{3.5}$$

The next challenge is to sample configurations from the Boltzmann distribution. Generally, sample from the Boltzmann distribution is as hard as computing partition function directly. The way in Monte Carlo is Markov Chain sampling, in which one needs to construct a Markov chain that has the desired distribution as its equilibrium distribution. The state of the chain after a number of steps is used as a sample of the desired distribution. The idea is that if a configuration $s$ is selected from the equilibrium distribution, one may find rules to generate a new configuration $s'$ in a random fashion from the previous one. The rules should make sure that $s'$ does not differ too much from $s$ than it could have been sampled directly from the same distribution.

When using Markov chains in Monte Carlo sampling, two conditions need to be satisfied: ergodicity and detailed balance. The sampling is ergodic if any other configuration can be reached starting from an arbitrary configuration by a Markov chain with a finite number of steps. This property will make sure that the sampling method can draw samples from the entire configuration space. The detailed balance condition is to ensure that a

Markov chain sampling equilibrium configurations will remain in equilibrium. This can be written in the following condition,

$$P(s)p(s \to s') = P(s')p(s' \to s) \tag{3.6}$$

where $P(s)$ is the Boltzmann probability distribution and $p(s \to s')$ is the probability for transitioning from configuration $s$ to $s'$.

The last question is that in general the equilibrium distribution is not known at the beginning of simulation. But, it can be shown that detailed balance will ensures that a Markov chain on average will approach equilibrium as it moving on, irrespective of where the starting configuration. In practice, one could run the Monte Carlo sampling for several steps to start the simulation. In this way, the simulation will loss the information of where it start and reach the equilibrium configurations.

### 3.1.1 The Metropolis algorithm

Metropolis algorithm is a way to generate Markov chain from the configuration $s$ by changing a single degree of freedom at a time. For example, we will flip a spin in Ising model at each sampling step. The following steps describe the Metropolis algorithm in general. Let $f(x)$ be a function that is proportional to the desired probability distribution $P(x)$.

1. Initialization: Choose an arbitrary point $s_0$ to be the first sample, and choose an arbitrary probability distribution $Q(s'|s)$ which gives the distribution for next sample $s'$ condition on the previous sample $s$. For Metropolis algorithm, $Q$ must be symmetric, i.e. $Q(x|y) = Q(y|x)$. The function $Q$ is called jumping distribution.

2. For each iteration t:

- Generate a candidate $s'$ for the next sample by sampling from the distribution $Q(s'|s_t)$.
- Calculate the acceptance ratio $r = f(s')/f(s_t)$. This ratio will be used to decide whether to accept or reject the candidate. Because $f$ is proportional to distribution of $P$, one have $r = P(s')/P(s_t)$.
- If $r \geq 1$, accept the new sample by setting $s_{t+1} = s'$. Otherwise, accept this candidate with probability $r$. If the candidate is rejected, set $s_{t+1} = x_t$.

In statistical physics, we can choose $Q(s'|s_t) = \mathrm{e}^{-\Delta S}$. $\Delta S = S(s') - S(s)$ is the change in the action. Then one can get the probability of transition from configuration $s$ to $s'$ as

$$p(s \to s') = min(1, \mathrm{e}^{-\Delta S}) \tag{3.7}$$

In practice, one could update the configuration through the lattice in a sequential way, proposing a randomly chosen new state of the state at each site. In another words, the step from one configuration to the next is a local update of the configuration. When one has visited all sites on the lattice, one performed one Monte Carlo sweep. After each sweep, we could record the observable at that configuration.

## 3.2 Quantum Monte Carlo Method

Quantum Monte Carlo[60] includes a large number of computational methods whose purpose is to study the complex quantum systems. In many-body physics, one typi-

cally needs to find many-body wave function to solve the Shcródinger equation for a given system. The challenge is that the many-body wave function has an exponentially large size, which in many case is not feasible. Traditionally, people approximate the many-body wave function as an symmetric or antisymmetric function of one-body orbitals. This method has several drawbacks, one is that this simple wave function does not include quantum many-body correlations; another is that the convergence is very slow.

Quantum Monte Carlo is a way to directly study the many-body wave function beyond simple approximations. In some circumstance, quantum Monte Carlo could give an exact solution of many-body problem, while in other case quantum Monte Carlo could give very good approximation of the ground state for the many-body system. For more detail discussion, one could read textbooks[33, 12] and review article[21]

As we discussed in chapter 2, a d-dimensional quantum action could be mapped to (d+1)-dimensional classical problem in the path integral formulation. In this sense, quantum version of Markov Chain Monte Carlo works the same as classical Monte Carlo by generating a set of samples through Markov Chain Monte Carlo sampling.

## 3.3 Phase diagram of Quantum 2+1d XY Model with Dissipation

### 3.3.1 Monte Carlo Simulation

The quantum Monte Carlo can be applied to the action[1.6] to study the phase diagram of this model[63, 48]. In quantum Monte Carlo simulation, we choose a 2D square lattice with $N \times N$ lattice sites. The imaginary time axis $[0, \beta]$ is discretized into $N_\tau$

slices. Periodic boundary conditions are imposed along $x$, $y$, and $\tau$ directions. The (2+1)D quantum XY model could be written in this discretized lattice as

$$\begin{aligned} S &= -K \sum_{\langle \boldsymbol{x},\boldsymbol{x}'\rangle,\tau} \cos(\Delta\theta_{\boldsymbol{x},\boldsymbol{x}',\tau} + \frac{K_\tau}{2} \sum_{\boldsymbol{x},\tau} (\theta_{\boldsymbol{x},\tau} - \theta_{\boldsymbol{x},\tau-1})^2 \\ &+ \frac{\alpha}{2} \sum_{\langle \boldsymbol{x},\boldsymbol{x}'\rangle,\tau} \frac{\pi^2}{N_\tau^2} \frac{[\Delta\theta_{\boldsymbol{x},\boldsymbol{x}',\tau} - \Delta\theta_{\boldsymbol{x},\boldsymbol{x}',\tau'}]^2}{\sin^2(\frac{\pi|\tau-\tau'|}{N_\tau})} - h_4 \sum_{\boldsymbol{x},\tau} \cos(4\theta_{\boldsymbol{x},\tau}) \end{aligned} \tag{3.8}$$

where $K_\tau = C/\Delta\tau$,$K = 2J_2\Delta\tau$, $h_4 = h_4\Delta\tau$, $\Delta\tau = \beta/N_\tau$, and $\Delta\theta_{\boldsymbol{x},\boldsymbol{x}',\tau} = \theta_{\boldsymbol{x},\tau} - \theta_{\boldsymbol{x}',\tau}$. In this way, $K$, $K_\tau$, $\alpha$, and $h_4$ are all dimensionless variables. The ultra-violet cut-off $\Delta\tau$ is fixed and set to 1. The temperature is controlled by $N_\tau^{-1}$. As $N_\tau \to \infty$, we could in principal approach the quantum limit $T \to 0$.

The same numerical procedure as in [48] is used for the Monte Carlo simulations. Discretized $\theta_{\boldsymbol{x},\tau} = n2\pi/32$ is used to speed up the simulation rather than a continuous variable. The typical system size is $N = 50$ and $N_\tau = 200$.

The simulation starts from a random configuration of $\{\theta_{\boldsymbol{x},\tau}\}$. Each Monte Carlo sweep is done by update all angles at each site locally from $\theta_{\boldsymbol{x},\tau}$ to $\theta_{\boldsymbol{x},\tau} + \theta'$, where $\theta'$ is a random angle between $-2\pi$ and $2\pi$. The parallel tempering is used to speed up the relaxation. In the simulation, first $10^4$ sweeps are dropped and take $10^6$ measurements for all observables.

The following quantities are calculated to characterize the different phases and phase transition among them.

1. Action susceptibility. The action susceptibility is defined as

$$\chi_S = \frac{1}{N^2 N_\tau} (\langle S^2 \rangle - \langle S \rangle^2) \tag{3.9}$$

where $\langle \cdots \rangle$ denotes the average over the Monte Carlo measurements. In classical system,

$S = \beta H$, $\chi_S$ is related to specific heat. As $T \to 0$, it measures zero-point fluctuations which are expected to be singular at the critical point. Therefore it is used to identify the critical point in this QMC simulation.

2. Helicity Modulus. The helicity modulus or stiffness measures the change of energy resulting from small twist of spins along the spatial direction,

$$\Upsilon_x = \frac{1}{N^2 N_\tau}\left\langle \sum_{\langle \boldsymbol{x},\boldsymbol{x}'\rangle}\sum_{\tau}\cos(\Delta\theta_{\boldsymbol{x},\boldsymbol{x}',\tau})\right\rangle - \frac{K}{N^2 N_\tau}\left\langle\left(\sum_{\langle \boldsymbol{x},\boldsymbol{x}'\rangle}\sum_{\tau}\sin(\Delta\theta_{\boldsymbol{x},\boldsymbol{x}',\tau})\right)^2\right\rangle \quad (3.10)$$

3. Order parameter. For XY spins, the order parameter $\boldsymbol{M}(\boldsymbol{x},\tau) = (\cos\theta_{\boldsymbol{x},\tau}, \sin\theta_{\boldsymbol{x},\tau})$. The magnetization is defined as

$$M = \frac{1}{N^2 N_\tau}\left\langle\left|\sum_{\boldsymbol{x},\tau} e^{i\theta_{\boldsymbol{x},\tau}}\right|\right\rangle. \quad (3.11)$$

The two dimensional magnetization is also calculated to find the 2D order in the plane at a given time $\tau$ and then average over $\tau$, which is given by

$$M_{2D} = \frac{1}{N^2 N_\tau}\left\langle\sum_{\tau}\left|\sum_{\boldsymbol{x}} e^{i\theta_{\boldsymbol{x},\tau}}\right|\right\rangle \quad (3.12)$$

4. Correlation Function of the Order Parameter. The correlation function is

$$G_\theta(\boldsymbol{x},\tau) = \frac{1}{N^2 N_\tau}\sum_{\boldsymbol{x}',\tau'}\langle e^{i(\theta_{\boldsymbol{x}'+\boldsymbol{x},\tau'+\tau} - \theta_{\boldsymbol{x}',\tau'})}\rangle \quad (3.13)$$

$G_\theta(\boldsymbol{x}\to\infty,\tau\to\infty) \to M^2$ while $G_\theta(\boldsymbol{x}\to\infty,\tau=0) \to M_{2D}^2$.

5. Vortices and warps: densities and correlations. The vortices and warps could be identify numerically from the four link variables of a plaquette,

$$\rho_v(\boldsymbol{x},\tau) = \frac{1}{2\pi}(\nabla\times\boldsymbol{m})_{i,j,\tau} = (m^x_{i,j,\tau} + m^y_{i+1,j,\tau} - m^x_{i+1,j+1,\tau} - m^y_{i,j+1,\tau})/(2\pi), \quad (3.14)$$

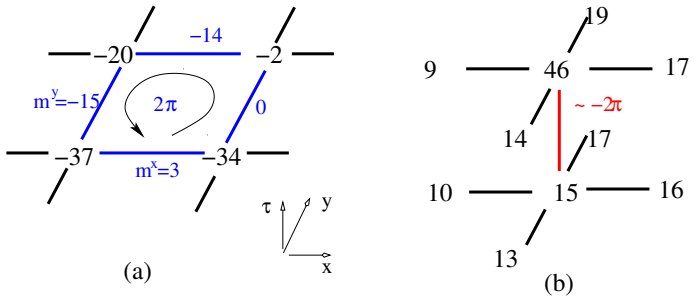


Figure 3.1: Examples of vortex (a) and warp (b) in Monte Carlo simulation. The numbers at the lattice site are $\theta$'s in units of $2\pi/32$ and are non-compact variables. The numbers in the links are the velocity fields. (a) For the number shown, the vortex is 1. (b), the change of $(\nabla \cdot \boldsymbol{m})_{i,j,\tau}$ for two neighboring time slices is close to $-2\pi$, is identifying as an antiwarp[63].

where $m^{x,y}$ are restricted to be within $(-\pi, \pi)$. $\rho_v(\boldsymbol{x}, \tau) = \pm 1$ if $(\nabla \times \boldsymbol{m})_{i,j,\tau} = \pm 2\pi$. Similarly, the warps can be calculated as following, first calculate divergence of vector field

$$(\nabla \cdot \boldsymbol{m})_{i,j,\tau} = (m^x_{i,j,\tau} - m^x_{i-1,j,\tau} + m^y_{i,j,\tau} - m^y_{i,j-1,\tau})/4 \tag{3.15}$$

Then warps are calculated as

$$\begin{aligned} \rho_w(\boldsymbol{x}, \tau) &= 1, \text{if}(\nabla \cdot \boldsymbol{m})_{i,j,\tau+1} - (\nabla \cdot \boldsymbol{m})_{i,j,\tau} > 2\pi - \delta\theta \\ \rho_w(\boldsymbol{x}, \tau) &= -1, \text{if}(\nabla \cdot \boldsymbol{m})_{i,j,\tau+1} - (\nabla \cdot \boldsymbol{m})_{i,j,\tau} > -2\pi + \delta\theta \end{aligned} \tag{3.16}$$

where $\delta\theta \ll 2\pi$ to accommodate small angle changes due to spin waves. Examples of vortices and warps are shown in FIG.3.1 The densities of vortices and warps are computed

$$\begin{aligned} \rho_v &= \frac{1}{N^2 N_\tau} \sum_{\boldsymbol{x},\tau} \langle |\rho_v(\boldsymbol{x}, \tau)| \rangle, \\ \rho_w &= \frac{1}{N^2 N_\tau} \sum_{\boldsymbol{x},\tau} \langle |\rho_w(\boldsymbol{x}, \tau)| \rangle \end{aligned} \tag{3.17}$$

Also their correlation functions are computed

$$
\begin{aligned}
G_v(\boldsymbol{x},\tau) &= \frac{1}{N^2 N_\tau}\sum_{\boldsymbol{x}',\tau'}\langle\rho_v(\boldsymbol{x}'+\boldsymbol{x},\tau'+\tau)\rho_v(\boldsymbol{x}',\tau')\rangle, \\
G_w(\boldsymbol{x},\tau) &= \frac{1}{N^2 N_\tau}\sum_{\boldsymbol{x}',\tau'}\langle\rho_w(\boldsymbol{x}'+\boldsymbol{x},\tau'+\tau)\rho_w(\boldsymbol{x}',\tau')\rangle. \qquad (3.18)
\end{aligned}
$$

### 3.3.2 Phase Diagram

The dissipative quantum XY model without the four-fold anisotropic field $h_4$ has been studied. The phase diagram for small $K_\tau = 0.01$ has been obtained through Monte Carlo simulation and is shown in FIG.(3.2). From the simulation, three distinct phases are identified, "Disordered" phase, "Quasi-ordered" phase, and "Ordered" phase. The properties of all the three phases are summarized in Table(3.1). In the following three subsection, the properties of the phase transition will be illustrated.

| Quantity | Disordered | Quasi-ordered | Ordered |
|---|---|---|---|
| M | 0 | $\lim_{N\to\infty} M \to 0$ | finite |
| $\rho_v$ | O(1) | $\ll 1$ | $\ll 1$ |
| $G_v(x)$ | exponential decay | power law | power law |
| $\rho_w$O(1) | O(1) | $\ll 1$ | |
| $G_w(\tau)$ | $1/\tau^2$ | $1/\tau^2$ | $1/\tau^\alpha(\alpha > 2)$ |
| $\Upsilon_x$ | 0 | finite,jump at transition | finite, no jump at transition |
| $G_\theta(x,0)$ | exponential | quasi-long range | long range |
| $G_\theta(0,\tau)$ | exponential | exponential | long range |

Table 3.1: Properties of three phases of the dissipative quantum 2+1D XY model[63].

### 3.3.3 Phase transition from disordered to quasi-ordered phase

By fixing $\alpha = 0.01$ and varying $K$, the phase transition from disordered phase to quasi-ordered phase is obtained. Several static observables are used to identify the

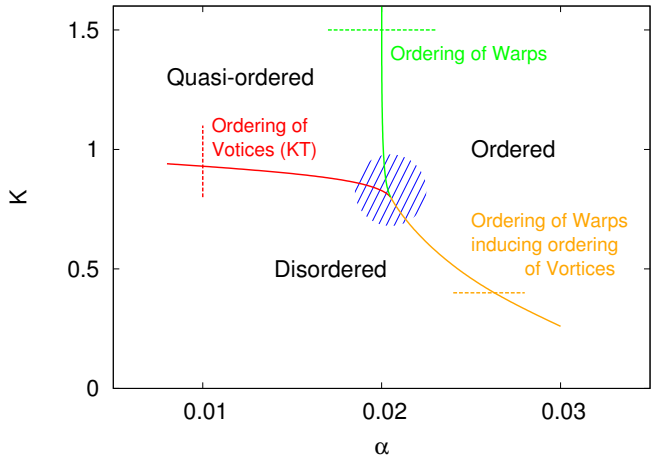


Figure 3.2: Phase diagram for the quantum 2+1D XY model with dissipation in $\alpha - K$ plane for $K_\tau = 0.01$. The transition lines are determined through non-analyticity of several static observables with a lattice size $N = 50$, $N_\tau = 200$. The dashed line denote the way to change of parameters. The phase diagram is obtained by several ways to change parameters[63].

transition point, as shown in FIG.(3.3). The characteristics of this phase transition can be described by Kosterlitz-Thouless transition, in which a quasi long-range spatial order is developed when $K$ increase. The helicity modulus $\Upsilon_x$ becomes finite in the quasi-ordered phase. The correlation functions for vortices and warps are shown in FIG.(3.4). When $K$ increases, $G_v(x, 0)$ changes from an exponential decay in the disordered phase to a power-law decay in quasi-ordered phase. The warp correlation function $G_w(0, \tau)$ remains unchanged in both sides and follows the asymptotic form $\propto 1/\tau^2$. This confirms that the transition from disordered phase to quasi-ordered phase is consistent with the Kosterlitz-Thouless transition.

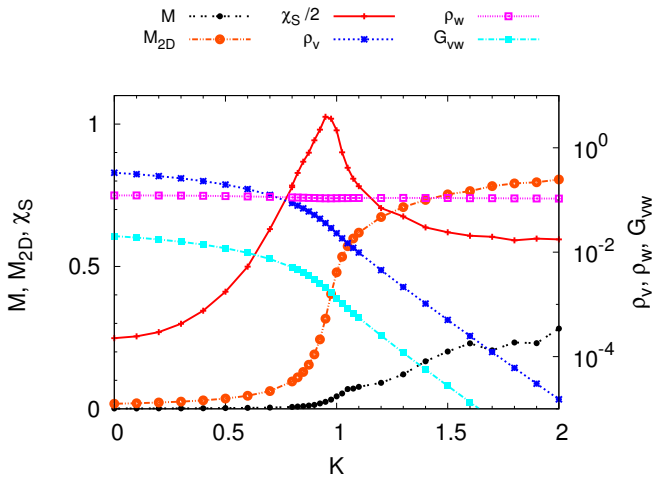


Figure 3.3: Static properties of phase transition from disordered phase to quasi-ordered phase. The phase transition point $K_c$ can be identified as the non-analytical point in the figure. Here, $K_\tau = 0.01$,$\alpha = 0.01$, and $K$ is varies. The lattice size is $N = 50$ and $N_\tau = 200$[63].

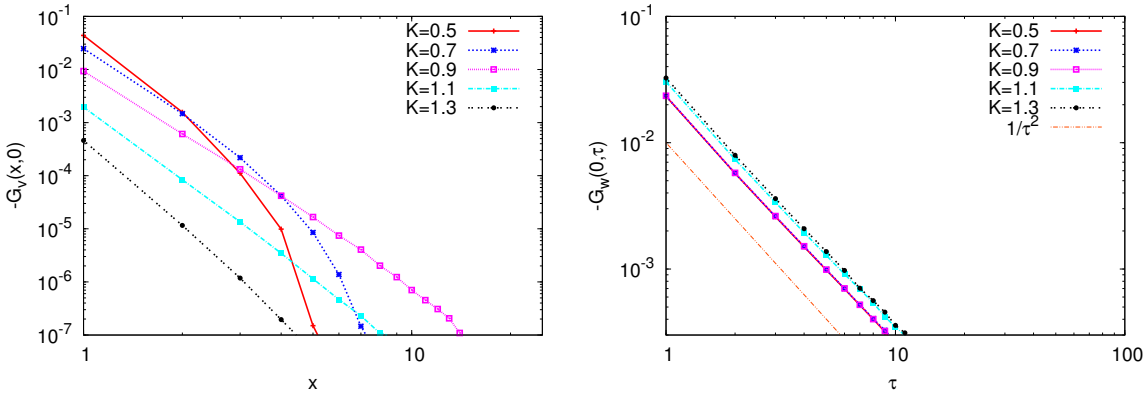


Figure 3.4: Correlation function of warps and vortices of phase transition from disordered phase to quasi-ordered phase. Here, $K_\tau = 0.01$,$\alpha = 0.01$, and $K$ is varies. The lattice size is $N = 50$ and $N_\tau = 200$[63].

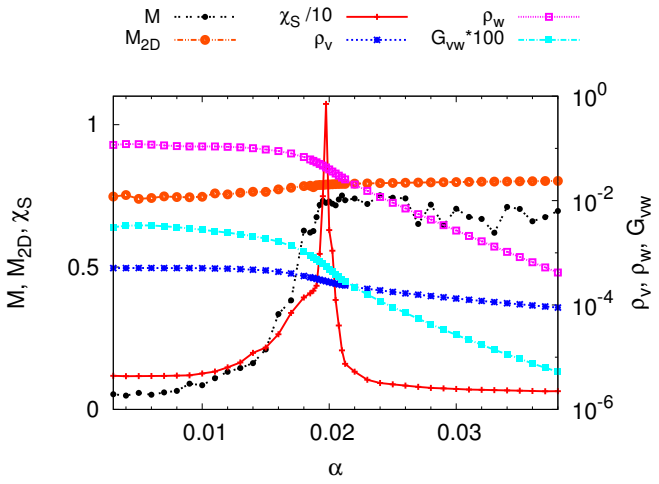


Figure 3.5: Static properties of phase transition from quasi-ordered phase to ordered phase. The phase transition point $\alpha_c$ can be identified as the non-analytical point in the figure. Here, $K_\tau = 0.01$,$K = 1.5$, and $\alpha$ is varies. The lattice size is $N = 50$ and $N_\tau = 200$[63].

### 3.3.4 Phase transition from quasi-ordered phase to ordered phase

For fixed $K > K_c$, one could tune the transition from quasi-ordered phase to ordered phase by varying $\alpha$. Various static properties are shown in FIG.(3.5) and critical value $\alpha_c$ is read from the non-analytical point. The spatial properties, such as $M_{2D}$, $\rho_v$, and $\Upsilon_x$ have small non-analytic change at the critical point $\alpha_c$. The density of warps, on the other hand, changes its slope at $\alpha_c$ and decrease exponentially as $\alpha$ increase. The correlation function, as shown in FIG.(3.6) also confirms that this phase transition is mainly driven by warps. The warp correlation function change from $1/\tau^2$ in the quasi-ordered phase to $1/\tau^a (a \sim 3$ for $\alpha = 0.023)$ in the ordered phase. Near $\alpha_c$, $1/\tau$ decay is observed and is consistent with analytical analysis[2, 3]. From the figures, one could also see the correlation function of vortices has no change from quasi-ordered phase to ordered phase.

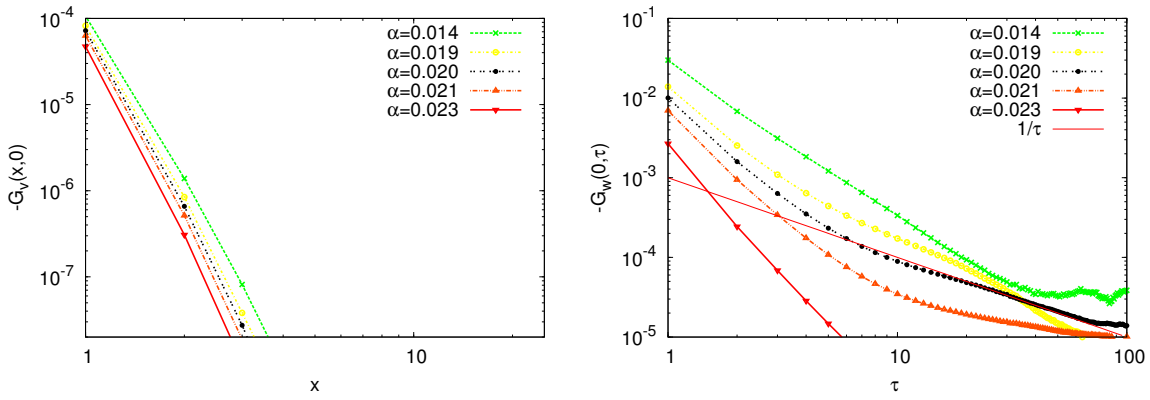


Figure 3.6: Correlation function of warps and vortices of phase transition from quasi-ordered phase to ordered phase. Here, $K_\tau = 0.01$,$K = 1.5$, and $\alpha$ is varies. The lattice size is $N = 50$ and $N_\tau = 200$[63].

### 3.3.5 Phase transition from disordered phase to ordered phase I

This phase transition is particularly interesting as it gives the quantum critical fluctuation spectrum as proposed in[55]. To study this phase transition, $K = 0.4$ has been chosen and $\alpha$ is varied. First, we exam the static properties of this phase transition and the results are shown in FIG.(3.7). The helicity modulus $\Upsilon_x$ and magnetization $m$ become finite for $\alpha > \alpha_c$. Both vortex and warp densities change their slope across $\alpha_c$. In another word, long range order develop simultaneously along spatial and temporal directions. One also should noticed that the density of warps decay faster than vortex density across the critical point. Through the vortices and warps correlation function, as shown in FIG.(3.8), one could notice the change of warps correlation is more drastic than change of vortex correlation.

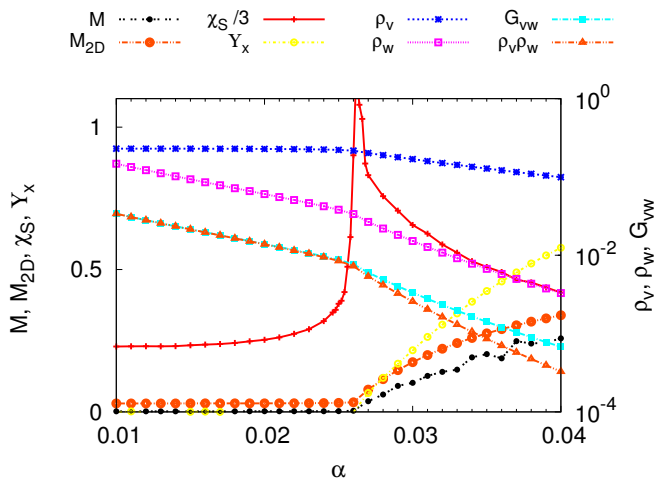


Figure 3.7: Static properties of phase transition from disordered phase to ordered phase. The phase transition point $\alpha_c$ can be identified as the non-analytical point in the figure. Here, $K_\tau = 0.01$,$K = 0.4$, and $\alpha$ is varies. The lattice size is $N = 50$ and $N_\tau = 200$[63].

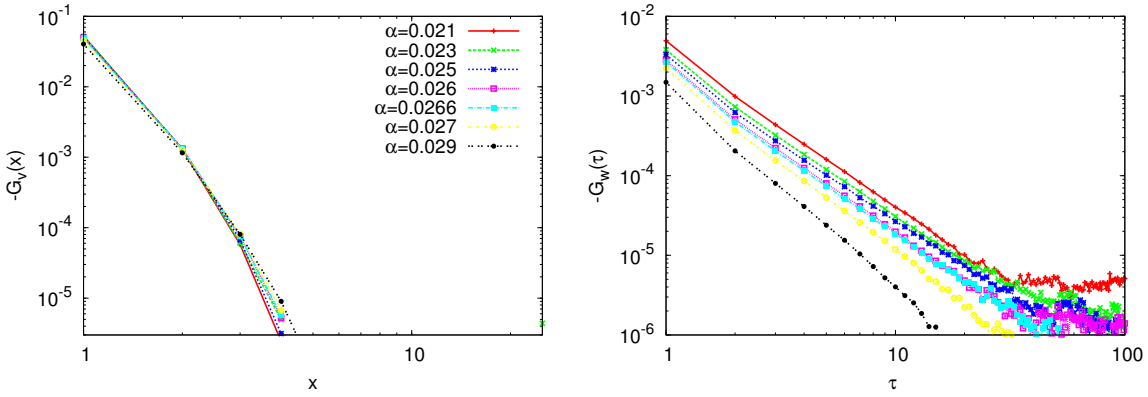


Figure 3.8: Correlation function of warps and vortices of phase transition from quasi-ordered phase to ordered phase. Here, $K_\tau = 0.01$,$K = 0.4$, and $\alpha$ is varies. The lattice size is $N = 50$ and $N_\tau = 200$[63].

The most important and novel results are revealed by order parameter correlation function. In FIG.(3.9), the order parameter correlation functions have been shown. From the figure, one could see that $G_\theta(x,\tau)$ could be separated into two parts for a fixed $x$ and for a fixed $\tau$. For $\alpha < \alpha_c$, they tend to go to zero for large $\tau$ or $x$, and for $\tau > \tau_c$, they approach to a constant value for large $x$ and $\tau$. From the numerical simulation, the asymptotic behavior of $G_\theta(x,\tau)$ turns out to be a separable function in $x$ and $\tau$ as

$$G_\theta(x,\tau) = \frac{A}{\tau^{1+\eta_\tau}} e^{-(\tau/\xi_\tau)^{1/2}} \frac{1}{x^{\eta_x}} e^{-x/\xi_x}, \tag{3.19}$$

where $\xi_x$ and $\xi_\tau$ are correlation length along spatial and temporal direction, respectively. The anomalous exponent $\eta_\tau \approx 0$. By fitting the correlation functions for different $\alpha$ to the scaling form in Eq.(3.19), $\xi_x$ and $\xi_\tau$ as a function of $\alpha$ could be obtained. The results are shown in FIG.(3.10). In the fluctuation regime, the behavior of $\xi_\tau$ is in the same form as in the theoretical prediction, which is given by

$$\xi_\tau(\alpha - \alpha_c) = \tau_c e^{a\sqrt{\alpha_c/(\alpha_c-\alpha)}}, \tag{3.20}$$

where $a$ is a constant of $O(1)$ and $\tau_c \approx 0.12$ from the simulation. The estimated $\tau_c$ is also consistent with theoretical estimation which is given by $\tau_c = 1/\sqrt{K/K_\tau} = 0.16$ with $K = 0.4$ and $K_\tau = 0.01$. The relation of $\xi_x$ and $\xi_\tau$ also illustrates in FIG.(3.10). Numerically, one could fit the data in the form $\xi_x \propto \xi_\tau^{1/z}$ with $z > 8$. But $z = \infty$ is more reasonable due to it is consistent with $z = \infty$ in [2]. Within numerical uncertainty, we have

$$\xi_x/\xi_0 \approx \ln(\xi_\tau/\tau_c). \tag{3.21}$$

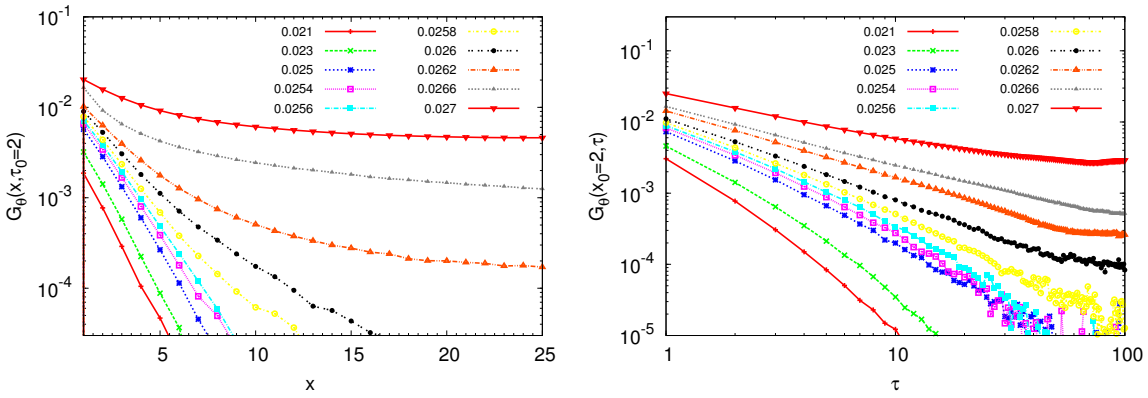


Figure 3.9: The order parameter correlation function $G_\theta(x,\tau)$ for phase transition from disordered phase to ordered phase. The lattice size is $N = 50$ and $N_\tau = 200$. $G_\theta(x = 2,\tau)$ and $G_\theta(x,\tau = 2)$ are shown to demonstrate spatial and temporary party of the correlation function[63].

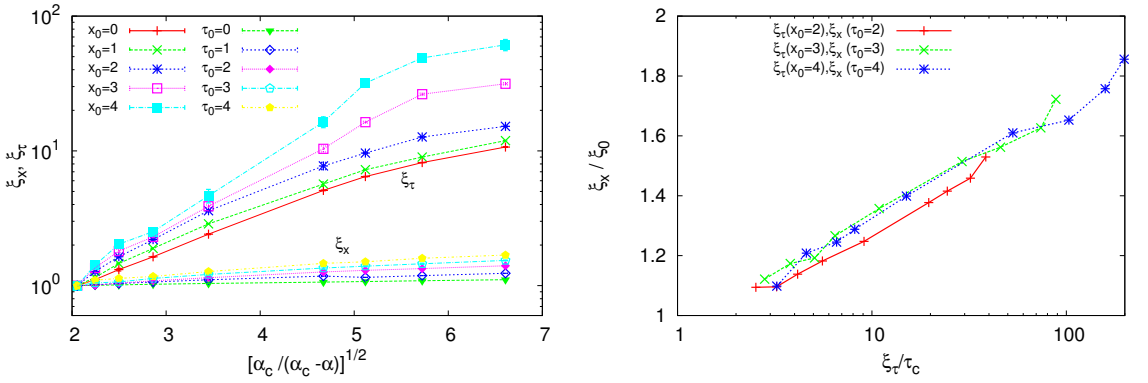


Figure 3.10: The left panel show $\xi_\tau$ and $\xi_x$ as functions of $[\alpha_c/(\alpha_c - \alpha]^{1/2}$ with $\alpha_c = 0.026$. For $x = 0$,$\xi_\tau$ can be fitted as $\tau_c \exp[0.62\sqrt{\alpha_c/(\alpha_c - \alpha)}]$. The right panel shows the relation between $\xi_x(\alpha)$ and $\xi_\tau(\alpha)$. Within numerical uncertainty, $\xi_x/\xi_0 \sim \ln(\xi_\tau/\tau_c)$. This relation appears to be independent of $x$ and $\tau$ at large $x$ and $\tau$[63].

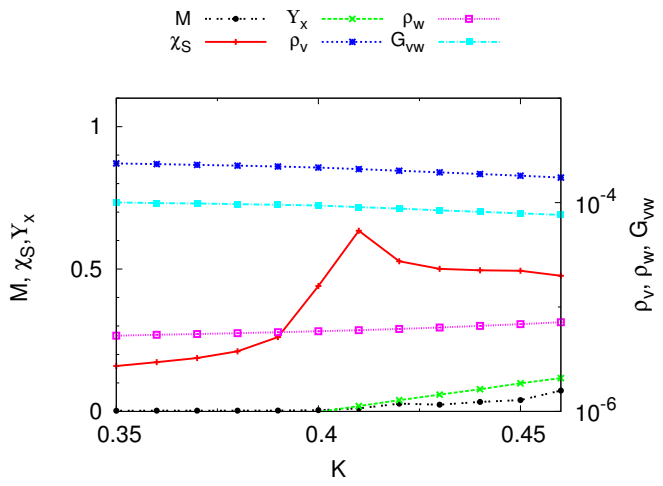


Figure 3.11: Static properties of phase transition from disordered phase to ordered phase. The phase transition point $\alpha_c$ can be identified as the non-analytical point in the figure. Here, $K_\tau = 0.01$,$K = 0.4$, and $\alpha$ is varies. The lattice size is $N = 50$ and $N_\tau = 200$.

### 3.3.6 Phase transition from disordered phase to ordered phase II

The phase transition from disordered phase to ordered phase can also be examined by fixing $\alpha$ and changing $K$. The statistic to identify the phase transition is shown in FIG.(3.11). The order parameter correlation function is shown in FIG.(3.12). From which, we can extract the correlation length as a function of $(K_c - K)/K_c$, which is shown in FIG.(3.13). The left graph shows the correlation length in time as a function a $(K_c - K)/K_c$ for different $x = 3, 4$. By fitting the line, we get the exponent around 0.5 0.6. The lines for $x = 3$ and $x = 4$ tending to collapse each other implies the separation between time and space. The right graph verifies that $\xi_x/\xi_0 \approx \ln(\xi_\tau/\tau_c)$.

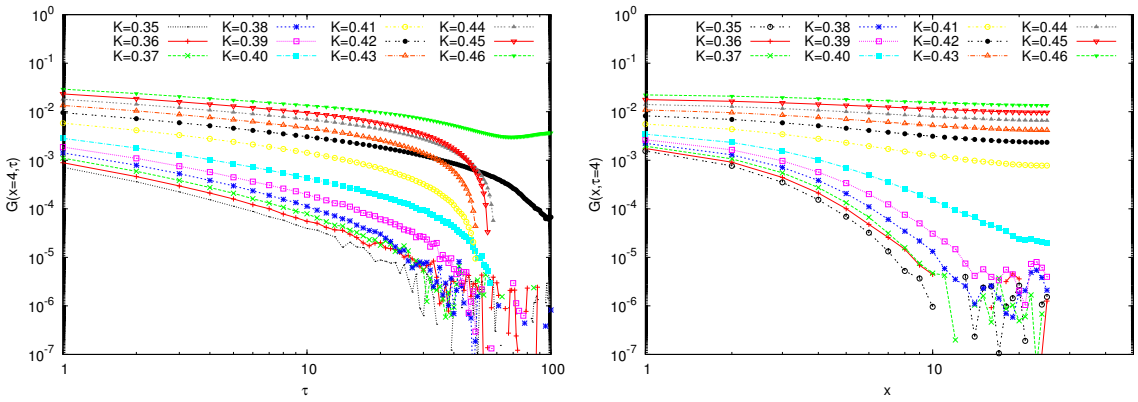


Figure 3.12: Order parameter correlation function for $K_\tau = 0.01$, $\alpha = 0.026$, and varying $K$. The lattice size is $N = 50$ and $N_\tau = 200$. (a). Order parameter correlation function for fixed $x = 4$ and varying $\tau$. (b). Order parameter correlation function for fixed $\tau = 4$ and varying $x$.

### 3.3.7 Magnetic Susceptibility

The measured thermodynamic properties in $YFe_2Al_10$[61], $C_v(T)$, $\chi(T)$, $M(B,T)$ have been fit by the scaling ansatz for the free-energy near a quantum critical point, which takes the form(one can refer chapter 2 for more detail)

$$f(T,B) = T^{(d+z)/y_t} f_F(B/T^{y_b/y_t}) = B^{(d+z)/y_b} \widetilde{f}_F(T/B^{y_t/y_b}), \tag{3.22}$$

where $T$ is the temperature and $B$ is the in-plane magnetic filed which can tune the transition to $B = 0$, $T = 0$ and introduce a cross-over from quantum critical properties to Fermi liquid properties. $z$ is the dynamical critical exponent. The scaling dimension satisfy $y_t = z$. The experiments give $\chi(T) \propto T^{-\gamma}$ with $\gamma \approx 1.4$ from $T \approx 20$ to about 2K. This quasi-2D metallic system is well described by the 2D dissipative quantum XY model, which

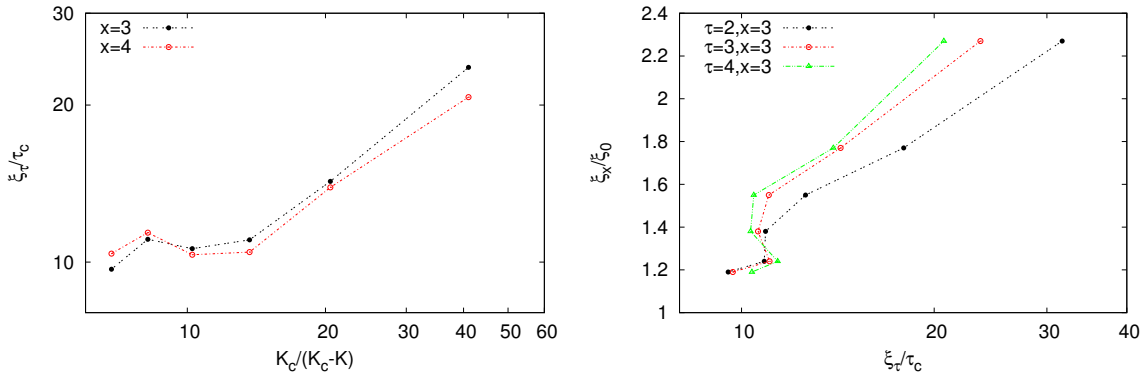


Figure 3.13: Correlation length in time and correlation length in space for $K_\tau = 0.01$, $\alpha = 0.026$, and varying $K$. The lattice size is $N = 50$ and $N_\tau = 200$. (a). Correlation length in time as a function of $(K_c - K)/K_c)$ by fitting the correlation function in the form $G_\theta(\tau) \sim \frac{1}{\tau} e^{-\tau/\xi_\tau}$ for two different $x = 3$ and $x = 4$. The two lines tend to have the same function form and the slope can be estimate to be about 0.5 0.6. (b). Correlation length in space as a function of correlation length in time. The x-axis is in log-scale. When $\xi_\tau$ increase about a decade, $\xi_x$ only increase about 50%.

give us an opportunity to compare the Monte Carlo simulation of magnetic susceptibility of 2D dissipative quantum XY model with the experimental measurement.

From both the analytical and numerical calculations, the order parameter correlation function has the form in the quantum critical regime,

$$G(r,\tau) = \chi_0 \log(r_0/r) e^{-r/\xi_r} \frac{1}{\tau} e^{-\tau/\xi_\tau}, \tag{3.23}$$

with $\xi_\tau = \tau_c e^{\sqrt{\alpha_c/(\alpha_c-\alpha)}}$ and $\xi_r/\xi_0 = \ln(\xi_\tau/\tau_c)$. The static magnetic susceptibility can then be found by integrating the order parameter correlation function over $r$ and $\tau$,

$$\begin{aligned}
\chi(0,0) &= \chi_0 \int d^2r_1 d^2r_2 \int d\tau_1 d\tau_2 \log(r_0/|\boldsymbol{r}_1 - \boldsymbol{r}_2|) e^{-|\boldsymbol{r}_1-\boldsymbol{r}_2|/\xi_r} \frac{1}{|\tau_1-\tau_2|} e^{-|\tau_1-\tau_2|/\xi_\tau} \\
&= \chi_0 \int d^2R d^2r \int d\tau' d\tau \log(r_0/|\boldsymbol{r}|) e^{-|\boldsymbol{r}|/\xi_r} \frac{1}{\tau} e^{-|\tau|/\xi_\tau} \\
&\approx V\chi_0 \xi_r^2 \xi_\tau \log(\xi_\tau),
\end{aligned} \tag{3.24}$$

where $\boldsymbol{R} = (\boldsymbol{r}_1 + \boldsymbol{r}_2)/2$, $\boldsymbol{r} = \boldsymbol{r}_1 - \boldsymbol{r}_2$, $\tau' = (\tau_1 + \tau_2)/2$, $\tau = \tau_1 - \tau_2$, and $V$ is the volume of the system. Considering the scaling $T\xi_\tau = 1$ and $\xi_r \sim \log(\xi_\tau)$, the scaling of magnetic susceptibility could be written as

$$\chi(0,0) \sim T^{-1} \log(T)^3. \tag{3.25}$$

In quantum Monte Carlo, the magnetization is defined as in 3.11. The static susceptibility can be calculated as

$$\chi = \frac{1}{N^2 N_\tau} (\langle M^2 \rangle - \langle M \rangle^2. \tag{3.26}$$

By changing $N_\tau$, which effectively change the temperature for $50 \times 50$ lattice, we could get the finite size scaling of $\chi$. In this calculation, we fixed $K_\tau = 0.01$, $K = 0.4$ and sweep $\alpha$. The $N_\tau$ is chosen from 50 up to 200. In unit of $\tau_c$, this will give result of temperature in

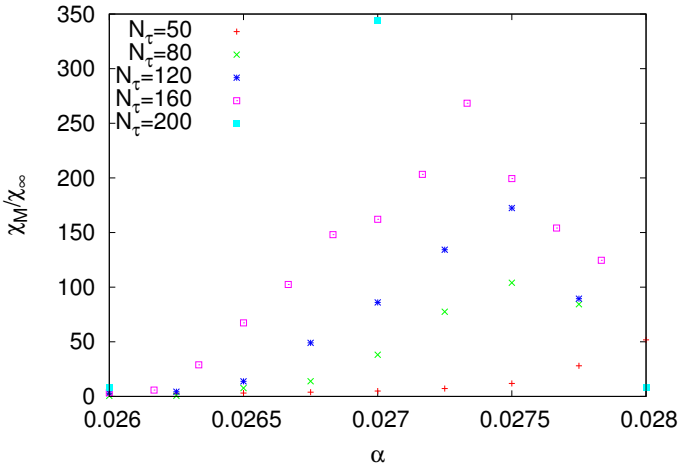


Figure 3.14: The static magnetic susceptibility for different $N_\tau$. The peaks of $\chi$ are identified as the critical value for each $N_\tau$ and those peak values are used to find the scaling of $\chi$ as a function of temperature. Here, $K_\tau = 0.01$,$K = 0.4$, and $\alpha$ is varies. The lattice size is $50 \times 50$ with different $N_\tau$.

range from $0.02\tau_c$ to $0.005\tau_c$. With $\tau_c \approx 20K$, the lowest temperature is about $0.1K$. So it is suitable to compare with experiments.

The finite size scaling for $\chi$ is shown in FIG.(3.14) and FIG.(3.15). From the graph, the experiment ansatz form $T^{-1.4}$ and theoretical expression $T^{-1}(\log T)^2$ can both fit the quantum Monte Carlo equally good.

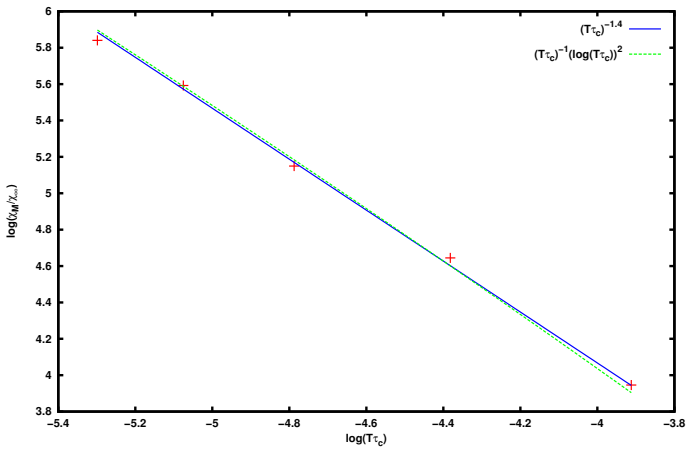


Figure 3.15: The scaling of static magnetic susceptibility. We use both the experimental ansatz form $T^{-1.4}$ and theoretical expression $T^{-1}(\log T)^2$ to fit the points and it turns out both of them can fit these points equally good.

# Chapter 4

# Renormalization Group Analysis of 2+1D Quantum XY Model with Dissipation

## 4.1 Introduction

The dissipative quantum XY model (1.6) is introduced [16, 17] to understand the superconductor to insulator transitions in 2 D films as a function of the normal state resistance [35]. The model is directly applicable to quasi-2D metallic ferromagnets with strong XY anisotropy. A realization of this model has been found with remarkable properties in the quantum-critical region [61]. It has also been shown recently that quasi-2D metallic anti-ferromagnets, with commensurate or incommensurate planar order and incommensurate uni-axial order also map to the dissipative XY model [54]. Metallic anti-ferromagnets

are of great experimental interest; they are realized by the Fe-based compounds, where superconductivity occurs in a region around the antiferromagnetic quantum-critical point, and in several heavy-fermion compounds. The same model also describes the statistical mechanics of the loop-current order proposed for under-doped cuprates [53] ending in a quantum-critical point in a region of doping of the highest $T_c$. In the Fe-compounds, in the heavy-fermions and in the cuprates, the normal state singular Fermi-liquid properties in the quantum-critical region, for example the resistivity and the entropy, have the same functional dependence on temperature. This motivated the idea that although the microscopic physics for these materials is quite different, the statistical mechanical model may be the same. Several new properties and a new phase has been discovered recently for the transitions in 2D superconducting films [47], which are not well understood. The dissipative quantum XY model has also been invoked [30] for the plateau transitions in quantum Hall effect. These diverse interesting problems call for a thorough understanding of the phase diagram and the correlation functions of the order parameter near the transitions of this model.

The classical XY model in 2D does not belong to the Landau-Ginzburg-Wilson (LGW) class of models for phase transition. The renormalization to zero of the fugacity of the vortices leads to a phase transition in which there is no order parameter but a discontinuity in the long-wavelength order parameter stiffness. The kinetic energy in the pure quantum XY model make the model Lorentz invariant. Therefore the quantum-transition and the associated critical fluctuations are the same as in the classical 3D XY model near its classical transition, which is in the LGW class. However, by including dissipation, the

model has a much richer phase diagram [48, 63]. The form of the order parameter correlation functions discovered [63] are quite unlike the form expected in extensions of the LGW theories to quantum-critical phenomena [40, 25]. The dissipative quantum XY model can be transformed [2, 3] to a much simpler model in which the properties are governed by topological excitations, two-dimensional vortices and 'warps'. Warps are instantons of monopole anti-montpole combinations with zero net charge as well as dipole. We use the re-expression of the dissipative quantum XY model in terms of warps and vortices and perform renormalization group calculations, which has some interesting new technical aspects, to reproduce the principal features of the phase diagram and of the essential aspects of the correlation functions discovered in the Monte-Carlo calculations. This leads to a deeper understanding of the results obtained by numerical methods.

The action of the (2+1)D quantum dissipative XY model of the angle $\theta(\mathbf{x},\tau)$ at space-imaginary time point $(\mathbf{x},\tau)$ is

$$\begin{aligned} S &= -J\sum_{\langle \mathbf{x},\mathbf{x}'\rangle}\int_0^\beta d\tau\cos(\theta_{\mathbf{x},\tau}-\theta_{\mathbf{x}',\tau})+\frac{C}{2}\sum_{\mathbf{x}}\int_0^\beta d\tau\left(\frac{d\theta_{\mathbf{x}}}{d\tau}\right)^2 \\ &+ \frac{\alpha}{2}\sum_{\langle \mathbf{x},\mathbf{x}'\rangle}\int d\tau d\tau'\frac{\pi^2}{\beta^2}\frac{\left[(\theta_{\mathbf{x},\tau}-\theta_{\mathbf{x}',\tau})-(\theta_{\mathbf{x},\tau'}-\theta_{\mathbf{x}',\tau'})\right]^2}{\sin^2\left(\frac{\pi|\tau-\tau'|}{\beta}\right)}, \end{aligned} \tag{4.1}$$

$\tau/2\pi$ is periodic in $\beta$, the inverse of temperature $1/(k_BT)$. $\langle \mathbf{x},\mathbf{x}'\rangle$ denotes nearest neighbors. The first term is the spatial coupling term as in classical XY model. The second term is the kinetic energy where $C$ serves as the moment of inertia. The third term describes quantum dissipations of the ohmic or Caldera-Leggett type [15]. The last term describes effects of anisotropy on a lattice with four-fold anisotropy.

## 4.2 Mapping to warps and vortics

In Refs.[2, 3], it is shown that after making a Villain transformation [57] and integrating over the small oscillations or spin-waves, the action is expressed in terms of link variables which are differences of $\theta$'s at nearest neighbor sites. Here we briefly work through the main steps to derived the final results. The Villain transform involves expanding the periodic function in terms of a periodic Gaussian,

$$\exp\Big[-\beta J\sum_{\langle ij\rangle}(1-\cos(\theta_i-\theta_j))\Big]\approx\sum_{m_{ij}}\exp\Big[-\beta J\sum_{\langle ij\rangle}(\theta_i-\theta_j-2\pi m_{ij})^2/2\Big] \tag{4.2}$$

where $m_{ij}$ are integers that live on the links of the square lattice. On a square lattice one can choose each site as $i=(x,y)$. One could combine $m_{x,y;x+1,y}$ and $m_{x,y;x,y+1}$ into a two components vector $\boldsymbol{m}_{x,y}$. Keeping the leading quadratic term $\theta_{x,y}-\theta_{x+1,y}\approx -a\nabla_x\theta_{xy}$, where $a$ is the lattice constant we have

$$(\theta_{xy}-\theta_{x+1,y}-2\pi m^x_{x,y})^2\approx a^2(\nabla_x\theta_{xy})^2+4\pi a\nabla_x\theta_{xy}m^x_{x,y}+4\pi^2m^{x2}_{x,y} \tag{4.3}$$

where $m^x_{x,y}$ is the x component of the vector field $\boldsymbol{m}_{xy}$. In Fourier space, this term can be written as

$$\begin{aligned}&\sum_{m_{ij}}\exp\Big[-\beta J\sum_{\langle ij\rangle}(\theta_i-\theta_j-2\pi m_{ij})^2/2\Big]\\ =\;&\sum_{\boldsymbol{m}}\exp\Big[\frac{J}{2}\sum_{\omega,\boldsymbol{k}}(a^2k^2\theta(\omega,\boldsymbol{k})^2+4\pi ia\theta(\omega,\boldsymbol{k})\boldsymbol{k}\cdot\boldsymbol{m}(\omega,\boldsymbol{k})+4\pi^2\boldsymbol{m}(\omega,\boldsymbol{k})\cdot\boldsymbol{m}(\omega,\boldsymbol{k}))\Big]\end{aligned} \tag{4.4}$$

The dissipation term can also be written in Fourier space as

$$S_{\rm diss}=\alpha\sum_{\omega,\boldsymbol{k}}|\omega|k^2\theta(\omega,\boldsymbol{k})^2. \tag{4.5}$$

Combing the dissipation term with the kinetic term and integrating out the $\theta$ fields, the effective model is now written as

$$\begin{aligned} Z &= \sum_{\boldsymbol{m}} \exp\Big[\sum_{\boldsymbol{k},\omega} -4\pi^2 J\boldsymbol{m}\cdot\boldsymbol{m} + \frac{4\pi^2 J^2 c(\boldsymbol{k}\cdot\boldsymbol{m})^2}{(C/c)\omega^2 + Jck^2 + \alpha|\omega|k^2}\Big] \\ &= \sum_{\boldsymbol{m}} \exp\Big[\sum_{\boldsymbol{k},\omega} -4\pi^2 J\frac{Jc|\boldsymbol{k}\times\boldsymbol{m}|^2}{(C/c)\omega^2 + Jck^2 + \alpha|\omega|k^2} - 4\pi^2 J\frac{\omega^2\boldsymbol{m}\cdot\boldsymbol{m}(C/c + \alpha k^2/|\omega|)}{(C/c)\omega^2 + Jck^2 + \alpha|\omega|k^2}\Big] \end{aligned} \tag{4.6}$$

where we redefined $J \to Ja^2\Delta\tau$, $C \to Ca^2/\Delta\tau$, $\alpha \to \alpha a^3$, $\boldsymbol{m} \to \boldsymbol{m}/a$, and $c = a/\Delta\tau$ with $\Delta\tau$ is the slice of imaginary time dimension.

The vector field $\boldsymbol{m}$ can be written as a sum of a longitudinal, $\boldsymbol{m}_l$, and a transverse component, $\boldsymbol{m}_t$ which by definition satisfy $\nabla\times\boldsymbol{m}_l = 0$ and $\nabla\cdot\boldsymbol{m}_t = 0$. The vorticity field $\rho_v(\boldsymbol{r},\tau)$ is then related to the transverse component alone and is given by

$$\nabla\times\boldsymbol{m}_t(\boldsymbol{r},\tau) = \rho_v(\boldsymbol{r},\tau) = \rho_{vc}\sum_{i,\mu}\delta(\boldsymbol{r}-\boldsymbol{r}_i)\delta(\tau-\tau_\mu), \tag{4.7}$$

where $(\boldsymbol{r}_i,\tau_\mu)$ is the location of the vortices and $\rho_{vc}$ is the charge of the vortex.

Unlike the 3D XY model, a new topological excitation is introduced to take the longitudinal component into account. This new topological excitation is given by a warp field $\rho_w(\boldsymbol{r},\tau)$ defined through a nonlocal relation in space,

$$\frac{d\boldsymbol{m}_l(\boldsymbol{r},\tau)}{d\tau} = \int d^2\boldsymbol{R}\rho_w(\boldsymbol{R},\tau)\frac{\boldsymbol{r}-\boldsymbol{R}}{|\boldsymbol{r}-\boldsymbol{R}|^3} \tag{4.8}$$

$\rho_w$ is event where the longitudinal component changes. One can see FIG.(4.1) for a warp in time dimension.

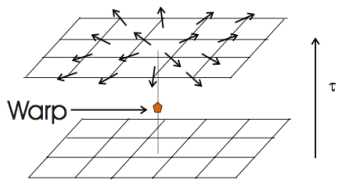


Figure 4.1: A warp defined in the time dimension in which the divergence of $\boldsymbol{m}$ field changes[3].

In terms of the $\boldsymbol{m}$, the Fourier transformed warp field $\rho_w(\boldsymbol{k},\omega)$ is

$$\frac{i\omega}{ck}\boldsymbol{k}\cdot\boldsymbol{m}(\boldsymbol{k},\omega)=\rho_w(\boldsymbol{k},\omega). \tag{4.9}$$

In terms of $\rho_v$, $\rho_w$, the action, in the continuum limit, could be split into three parts: $S=S_v+S_w+S'_w$,

$$\begin{aligned}
S_v &= \frac{1}{L^2\beta}\sum_{\boldsymbol{k},\omega}\frac{J}{k^2}|\rho_w(\boldsymbol{k},\omega)|^2,\\
S_w &= \frac{1}{L^2\beta}\sum_{\boldsymbol{k},\omega}\frac{\alpha}{4\pi|\omega|}|\rho_w(\boldsymbol{k},\omega)|^2,\\
S'_w &= \frac{1}{L^2\beta}\sum_{\boldsymbol{k},\omega}G(\boldsymbol{k},\omega)\left(JC-\frac{\alpha C|\omega|}{4\pi c}-\frac{\alpha^2k^2}{16\pi^2}\right)|\rho_w(\boldsymbol{k},\omega)|^2,
\end{aligned} \tag{4.10}$$

where $G(\boldsymbol{k},\omega)=\frac{1}{Jck^2+(C/c)\omega^2+\alpha|\omega|k^2}$.

## 4.3 Failure of Wilson RG and Hertz Theory

To study the quantum critical properties of this transformed action, one could use Wilson renormalization group method and Hertz's procedure to introduce fixed dynamical critical exponent. The predictions follow this procedure turns out not consistent with neither numerical simulation nor experimental results. In the following, the Wilson renormalization group method is given for the action of warps.

The action for the warps is

$$S_w = \frac{1}{L^2\beta}\sum_{\boldsymbol{k},\omega}\frac{\alpha}{4\pi|\omega|}|\rho_w(\boldsymbol{k},\omega)|^2 + \frac{\Delta_w}{T}\sum_i \rho_w(\boldsymbol{r}_i,\tau_i)^2 \tag{4.11}$$

where $\Delta_w$ is the core energy of warps. The $S'_w$ is neglected for a moment and will include in later discussion. One could follow the same procedure in [41] to get a transformed action through using the Stratonovich-Hubbard transformation,

$$S_w = \sum_\omega \frac{\alpha}{4\pi}|\omega|\phi(\omega)\phi(-\omega) - y_w\int_0^\beta \cos(\phi)d\tau \tag{4.12}$$

Following the standard Wilson RG procedure, one could split $\phi$ field into fast mode and slow mode,

$$\phi(\omega) = \phi_s(\omega) + \phi_f(\omega) \tag{4.13}$$

where,

$$\phi_s(\omega) = \begin{cases} \phi(\omega) & \text{if } |\omega| < \Lambda - d\Lambda \\ 0 & \text{otherwise} \end{cases} \tag{4.14}$$

and

$$\phi_f(\omega) = \begin{cases} \phi(\omega) & \text{if } \Lambda - d\Lambda < |\omega| < \Lambda \\ 0 & \text{otherwise} \end{cases} \tag{4.15}$$

with $\Lambda$ be the upper cut-off of the frequency. Then one could obtain an effective action for the slow modes by integrating the fast modes. This effective action with slow modes will have a cut-off $\Lambda - d\Lambda$ instead of $\Lambda$. To get back the original action, one should rescale the cut-off by $d\Lambda/\Lambda$. Finally, the renormalization group equations are read by compare the rescaled action with the original action. We will get the following RG equations, the detail

calculation could be found in the book [41]

$$\begin{aligned} \frac{dy_w}{d\ln\Lambda} &= (\frac{1}{\alpha}-1)y_w, \\ \frac{d\alpha}{d\ln\Lambda} &= 0 \end{aligned} \tag{4.16}$$

These turn out not quite right for warps problem. The right way to do the renormalization group calculation is given in [4, 5]. It could also be found in the appendix due to it is very important for this thesis.

Another issue is more critical for quantum dissipative XY model. As mentioned in quantum Monte Carlo simulation, the correlation function of this model can be separated into space and time, which is quite different with Hertz's theory. The three distinct parts of the phase diagram cannot be explained through the way by introducing fixed dynamical critical exponent. Without the $S'_w$ term, the problem is completely two independent degree freedoms which lives in space and time, respectively. Then one will predict that there are four different phases, which correspond the combinations of order and disorder of warps and vortices. To address this problem, we need to include the $S'_w$ term and generalize the Hertz's idea by considering the running dynamical critical exponent to take the anisotropy of space and imaginary time into account, which will be discussed in detail in the following chapter.

## 4.4 Renormalization Group Equations

As shown in last section, the renormalization group analysis must be done in real space, keeping the relevant terms, the action of the model can be written in space and in

imaginary time as,

$$
\begin{aligned}
S &= \alpha \sum_{i \neq j} \rho_w(\boldsymbol{r}_i, \tau_i) \ln \frac{|\tau_i - \tau_j|}{\tau_c} \rho_w(\boldsymbol{r}_j, \tau_j) \\
&\quad + g \sum_{i \neq j} \rho_w(\boldsymbol{r}_i, \tau_i) \frac{1}{\sqrt{|\boldsymbol{r}_i - \boldsymbol{r}_j|^2 + v^2(\tau_i - \tau_j)^2}} \rho_w(\boldsymbol{r}_j, \tau_j) \\
&\quad + \frac{J}{2\pi} \sum_{i \neq j} \rho_v(\boldsymbol{r}_i, \tau_i) \ln \frac{|\boldsymbol{r}_i - \boldsymbol{r}_j|}{a_c} \rho_v(\boldsymbol{r}_j, \tau_j) + \ln y_w \sum_i |\rho_w(\boldsymbol{r}_i, \tau_i)|^2 + \ln y_v \sum_i |\rho_v(\boldsymbol{r}_i, \tau_i)|^2.
\end{aligned}
\tag{4.17}
$$

The integration over $\mathbf{r}, \mathbf{r}'$ is over all space points over imaginary time $\tau$ from 0 to $1/T$. Here $g = \sqrt{JC}/4\pi$, $v^2/c^2 = J/C$, $C = C/\tau_c$ are dimensionless variables, and $c = a/\tau_c$, $a$ is the lattice constant and $\tau_c$ is the short time cut-off.

The first term in (4.17) is the action of the *classical* vortices interacting with each other through logarithmic interactions in space but the interactions are local in time. The second term describes the warps interacting logarithmically in time but locally in space. The third term is the action for a (anisotropic) Coulomb field between warps, which if present alone for the isotropic case is known [45] will not to cause a transition; it will be seen to be marginally relevant in the present problem in which the space-time anisotropy is required to flow. The short distance core-energy of the warps and vortices is taken care of by the final terms in which $y_v$ and $y_w$ are the fugacities of the vortices and the warps, respectively.

The warp and the vortex variables in the first two terms are orthogonal since they are related respectively to the divergence and rotation of a vector field. With just these two terms alone, the problem is easy. If the first term dominates, one expects a transition of the class of the classical Kosterlitz-Thouless transition through the renormalization of

the fugacity of vortices to 0. But the ordered phase would have bound vortex-anti-vortex pairs in space with nothing to correlate them in time. If the second term dominates, there is a quantum transition to a phase with binding of warp-antiwarp pairs in time but not in space. Four distinct phases would therefore be found in the $\alpha - KK_\tau$ plane. This is unlike the phase diagram of Fig. (3.2). We will show that given the growth of correlations due to the renormalization of the density of isolated vortices or of isolated warps $\rightarrow 0$, the actual critical points are determined by the third term. The third term scales time and space differently, depending on the flow due to the first two terms. This leads to ordering at $T = 0$ both in time and space to a state with symmetry of the 3D XY model over most of the phase diagram but an interesting region in which the system is spatially ordered for small times but disordered at larger times persists. The transformation to the topological model relies on a finite dissipation coefficient $\alpha$. One cannot take the limit $\alpha \rightarrow 0$ and expect to get back the properties of the (2+1) d quantum XY model without dissipation, which should have a quantum transition of the class of 3d classical XY model.

The Renormalization Group (RG) equations for the coupling $J$ and the vortex fugacity $y_v$ may be obtained following the same procedure of Kosterlitz [31] or Jose et al.[26]. The renormalization of these quantities can be obtained by scaling the spatial length scale $\ell_r = \ln(r/a)$, where $a$, the lattice constant serves as the short-distance cut-off are,

$$dJ = -\pi y_v^2 J^2 d\ell_r \tag{4.18}$$

$$dy_v = (2 - \frac{J}{4\pi}) y_v d\ell_r \tag{4.19}$$

To derive the RG equation for the parameters for the warps, we consider the

effective interaction between two warps at a point in space and separated by time $\tau > \tau_c$. This pair will be modified by the screening due to the creation of a virtual pair, at times $\tau'$ and $\tau''$, $\tau_c < |\tau' - \tau''| < \tau_c e^{d\ell_\tau}$, where $\ell_\tau = \ln(\tau/\tau_c)$ and $\tau_c$ is the short-time cutoff. We integrate over the coordinates of the two virtual warps to get a renormalized interaction between the real pair. The RG equations for $\alpha$ can be derived by scaling $\ell_\tau$ in this way. But the fugacity of warps is renormalized by both rescaling $\ell_\tau$ and, due to the third term in the action (4.17), by rescaling $\ell_r$. Therefore we must also consider the renormalization of the parameters $g$ and $v$. A scale dependent $v = d|r|/d\tau$ is equivalent to allowing a scale-dependent dynamical critical exponent,

$$z \equiv d\ell_\tau / d\ell_r. \tag{4.20}$$

The renormalization procedure for $y_w$, $g$ and $v$ is given in the appendix. The results are

$$d\alpha = -2\alpha y_w^2 d\ell_\tau, \tag{4.21}$$

$$dy_w = y_w\big((1-\alpha)d\ell_\tau + (2-g)d\ell_r\big), \tag{4.22}$$

$$dg = -g d\ell_r - \frac{8\pi^3}{3}\frac{g^2 y_w^2}{v a_c}\left((\frac{1}{4}+\frac{v^2}{2})dl_\tau + (1+\frac{v^2}{3})dl_r\right), \tag{4.23}$$

$$dv = \big(d\ell_\tau - d\ell_r\big)v. \tag{4.24}$$

These equations may be written as scaling equations either with respect to $\ell_r$ or $\ell_\tau$ by using $z$ defined by Eq. (4.20). For example, (4.24) may be written as

$$\frac{dv}{d\ell_\tau} = (1-y)v; \quad y = z^{-1} \tag{4.25}$$

It is obviously redundant to keep both $y$ and $v$. We note the identity

$$\frac{dy}{d\ell_\tau} - y = \frac{\tau}{r}\frac{dv}{d\ell_\tau} - (\frac{\tau}{r})^2 v^2 \tag{4.26}$$

Using the above equation, (4.25) can be re-written as

$$\frac{dy}{dl_\tau} = 2y(1-y). \tag{4.27}$$

## 4.5 RG Flow analysis

We now have a complete set of RG equations. First, we note that Eq. (4.27) will give the fixed points $y^* = 1, \infty, 0$, in which $y^* = 1$ is a stable fixed point. From Eq. (4.25), we note that near $y^* = 1$, the velocity has a stable fixed point at its initial value. The $z^* = \infty$ fixed point is unstable, corresponding to the unstable fixed point for velocity at $v^* = \infty$. The $z^* = 0$ fixed point is also unstable, corresponding to the unstable fixed point at $v^* = 0$. These results are in accordance with the investigations on expansion about isotropy of the classical anisotropic coulomb gas model in 3D [32], i.e. the model with only the third term in (4.17). We find that the 2D limit, (i.e. $v^* = 0$) as well as the 1D limit ($v^* = \infty$) is unstable (i.e. has critical points) towards the stable isotropic problem. We now consider the regimes of initial parameters in which the three different regions in the phase diagram in (3.2) are obtained, and calculate the correlation lengths in time and space about the critical points separating them:

I. $J/2\pi \lesssim 4, \alpha \lesssim 1$: Looking at the first two terms of the transformed action, (4.17), or the RG Eqs. (4.18, 4.21), the fugacity of both vortices and warps is large in this region. Therefore the model is in its quantum disordered state in this region, corresponding to region A in the phase diagram in Fig.(3.2).

II. $J/2\pi \lesssim 4$ and $\alpha \approx 1$: In this region, we must first analyze the equations for the warps, Eqs.(4.21, 4.22, 4.23). We note from Eqs. (4.21, 4.22) that for $z^* \to \infty$, and the initial $\alpha > 1$, $\alpha$ flows asymptotically to $\to$ const for long time. $y_w$ will flow to 0, provided $g$ remains finite or zero. For initial $\alpha < 1$, $\alpha$ flows asymptotically to 0 and $y_w$ to $+\infty$ at long times. Therefore $\alpha^* = 1$ is an unstable critical point. We note from (4.23) that near the $\alpha^* = 1$ fixed point, as $z \to \infty$ and $y_w \to 0$, $g$ flows to zero, consistent with the above requirement.

We expand near the unstable $\alpha = 1^-$ fixed point to find

$$y_w \propto \left(e^{-\tau/\xi_\tau} - 1\right); \quad \xi_\tau \propto e^{(b_0/(\alpha-1))^{1/2}}. \tag{4.28}$$

$b_0$ is a coefficient of $O(1)$. Let us study $J$ and $y_v$ near this point. To do so, we convert all scaling in terms of $\ell_\tau$ by using Eqs. (4.20,4.27). The flow of the vortex parameters $J$ and $y_v$ is now given by

$$\begin{aligned} \frac{dJ}{dl_\tau} &= -\frac{1}{z}\pi y_v^2 J^2 \\ \frac{dy_v}{dl_\tau} &= \frac{1}{z}(2 - \frac{J}{4\pi})y_v \end{aligned} \tag{4.29}$$

We also have the equation

$$\frac{dy_v}{dy_w} = \frac{1}{z(1-\alpha)}(2 - \frac{J}{4\pi})\frac{y_v}{y_w} \tag{4.30}$$

Near the critical point $z^* \to \infty$, but $(1-\alpha) \to 0$. From Eq. (4.27), one finds the leading behavior of $1/z = 0 + O(\tau^{-2})$. But $\alpha$ approaches its fixed point of 1 exponentially slowly with $\tau^{-1}$. Therefore the $(1-\alpha)$ term is not important compared to $z$. If $(2 - J/4\pi)$ does

not flow, as is found self-consistently, then we will get

$$y_v \propto y_w^{1/z}, \text{ i.e. } for\ 1/z \to 0,\ y_v \propto \ln y_w. \tag{4.31}$$

We can get the correlation length in space from the relation, $k \propto \omega^{1/z}$. For $1/z \to 0$, this gives that the spatial correlation length $\xi_r$ is proportional to logarithm of the temporal correlation length $\xi_\tau$. We can also get the same result explicitly from $d\ell_r = (1/z)d\ell_\tau$ and the result that $1/z \propto \tau^{-2}$ near this fixed point.

The same results for the RG flows are also obtained from the numerical solution of the equations near this critical point. The critical point corresponds to the quantum-disordered (A) to 3D ordered transition (B) in Fig.(3.2). The correlation lengths in time and space deduced above have been found in extensive Monte-carlo calculations [63]. We understand now that the physical region of the conjecture made in Ref. (Lijun that the freezing of warps drives the freezing of vortices. It is that the growing fugacity of warps drives a flow of the space-time metric parameter $z$ so that the fugacity of the vortices, Eq. (**??**) becomes time-dependent even for values of $J$ below the critical Kosterlitz-Thouless value of $8\pi$.

III. $\alpha \lesssim 1$ and $J/4\pi \approx 2$: In this region, it is appropriate to start the analysis with examination of Eqs. (4.18) for flow of $J$ and $y_v$. Eqs. (4.18) have the standard KT flow with the KT point $J^* = 8\pi$ near which $y_v \to 0$. For $J > 8\pi$, $y_w$ flows towards 0 and $J$ flows to *const*. Following Nelson and Kosterlitz, the spatial stiffness has a jump at the transition. Now we examine whether this is changed by the action of warps. We start by assuming that such a fixed point corresponds to the $z \to 0$ unstable fixed point. We will soon check that this is consistent. From Eq. (4.25), $z \to 0$ leads to $v \to 0$ at the fixed point.

Let us study how warps are affected by this. From Eq. (4.23), $g$ flows to 0. The equations (4.21), (4.22) may be written in terms of the scale length $\ell_r$ as

$$\frac{d\alpha}{d\ell_r} = -2z\alpha y_w^2 \tag{4.32}$$

$$\frac{dy_w}{d\ell_r} = y_w\big(z(1-\alpha)+2\big). \tag{4.33}$$

We note that neither the fugacity $y_w$ nor $\alpha$ flow in this case. So warps remain completely unaffected by the vortex freezing. There is no development of correlation in time, as we can check directly. This is consistent with the assumption that this fixed point corresponds to $z^* = 0$. We have a phase in which the spatial correlations become of the ordered Berezinsky-Kosterlitz-Thouless phase but there are no correlations in time. This corresponds to the transition from the quantum-disordered phase A to the quasi-ordered phase C in Fig. (3.2). The results are consistent with the Monte-carlo calculations, which give that the transitions at $T \to 0$ in this regime of parameters is a pure Kosterlitz-Thouless transition with a jump of spatial stiffness, with the correlations of the order parameter unchanged from those in the disordered phase. The phase transition A-C may well correspond to the superconductor to a Normal metal transition found in superconducting films [14]. If so, phase C must be an unusual metal. This matter requires further investigations.

IV. $J/4\pi \gtrsim 2, \alpha \to 1^-$: As discussed in III, for these values of $J$, $y_v \to \infty$ and isolated vortices are frozen for $\alpha < 1$. As $\alpha \to 1^-$, $y_v$ remains stable at this value and the RG equations for $\alpha$ and $y_w$ are simply (4.21) and (4.22), respectively. So $y_w \to 0$ as $\alpha \to 1$ and density of isolated warps tends to 0 rapidly for $\alpha > 1$. For $\alpha > 1$, long-range correlations develop in time as well as space and the ordered state is similar to that obtained directly from the quantum disordered state discussed in II above.

## 4.6 Summary

The above analysis leads to the flow diagrams, as shown in FIG.(4.2). From the two flow diagrams, one could easily identify three stable fix points, which are correspond to the three distinct phases in Monte Carlo simulations. The different behavior of flows for $\alpha > 1$ and $\alpha < 1$ imply $\alpha = 1$ is a critical point. Another critical poing $J/4\pi = 2$ is also identified from $\alpha < 1$ flow diagram.

In FIG.(4.3), we plot the phase diagram based on renormalization group analysis. From the quantum Monte Carlo simulations, we know that the quantum critical point weakly depend on $J$. But from first order RG calculations, the quantum critical point is $\alpha = 1$, which independent of $J$. The dependent of $J$ is believed to arise only under high order RG calculations. The key result, $\xi_r \sim \ln \xi_\tau$, is reproduced from RG calculation by introduce running dynamical critical exponent $z$.

## 4.7 Correlation Function

The correlation function for the order parameter following the same procedure as we do the Villain transformation. The correlation function is given by

$$C_{i\mu,j\nu} =< \mathrm{e}^{i\theta_{i\mu}} \mathrm{e}^{-i\theta_{j\nu}} >\equiv \frac{\int \mathcal{D}\theta \mathrm{e}^{-\bar{S}}}{\int \mathcal{D}\theta \mathrm{e}^{-S}} \tag{4.34}$$

where $\bar{S} = S + i(\theta_{i\mu} - \theta_{j\mu} - 2\pi \sum_{\mathrm{path}} \boldsymbol{m})$, the last term will not change the evaluation because all $\boldsymbol{m}$ are integers. This is added to reproduce the non-dissipation result. Using the usual Villain transformation with the definition of new auxiliary field $\vec{\eta}$ which live on the site of the space lattice. $\eta_x$ is 1 or 0 depending on whether or not the path include the

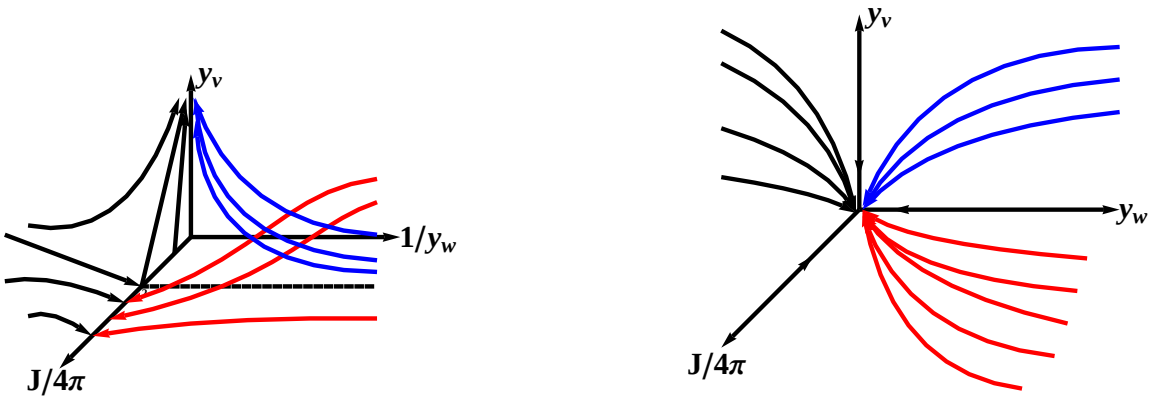


Figure 4.2: The sketch of the flows of the coupling constants based on expansion around the fix points. The left panel shows the flow diagram for $\alpha < 1$. The right panel shows the flow diagram for $\alpha > 1$.

link $xy\mu$ to $(x+1y\mu)$. The same definition for $\eta_y$. Similarly we define $\eta^0$ which is 1 or 0 depending on whether or not the path include the link $xy\mu$ to $(xy\mu+1)$. We get

$$\begin{aligned}\bar{S} = S \quad &+ \quad \frac{1}{L^2\beta}\sum_{ln}(2\pi J)G(\boldsymbol{k}_l,\omega_n)\Big\{(-i\omega_n\eta^{0*}/2)(i\boldsymbol{k}_l\cdot\boldsymbol{m}) + (-i\boldsymbol{k}_l\times\vec{\eta}^*)\cdot(i\boldsymbol{k}_l\times\boldsymbol{m}) + c.c. \\ &+ \quad \Big[(C/c)\omega_n^2 + \alpha|\omega_n|k^2\Big](\boldsymbol{m}\cdot\vec{\eta}) + |\omega_n\eta^0/2 + \boldsymbol{k}_l\cdot\vec{\eta}^*/2|^2\Big\} \qquad (4.35)\end{aligned}$$

with

$$S = \sum_{ln}\left[4\pi^2 J\boldsymbol{m}\cdot\boldsymbol{m} - \frac{4\pi^2J^2c(\boldsymbol{k}_l\cdot\boldsymbol{m})^2}{(C/c)\omega_n^2 + Jck_l^2 + \alpha|\omega|k_l^2}\right] \qquad (4.36)$$

and $G(\boldsymbol{k}_l,\omega_n) = \frac{1}{Jck_l^2+(C/c)\omega_n^2+\alpha|\omega_n|k_l^2}$. With the relation between $\boldsymbol{m}$ field and vortex and warp density

$$\boldsymbol{m} = \rho_v\frac{i\boldsymbol{k}\times\hat{z}}{k^2} + \rho_w\frac{c}{i\omega}\hat{k} \qquad (4.37)$$

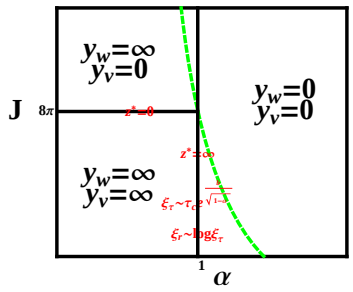


Figure 4.3: The sketch of the phase diagram from the renormalization group analysis. The blue dash line is obtained from the quantum Monte Carlo simulations.

we have

$$\begin{aligned}\bar{S} = S_v + S_w &+ \frac{1}{L^2\beta}\sum_{ln}(2\pi J)G(\boldsymbol{k}_l,\omega_n)\Big\{(-i\omega_n\eta^{0*}/2)(i\boldsymbol{k}_l\cdot\boldsymbol{m}) \\ &+ \frac{C+c\alpha k_l^2/|\omega_n|}{ik_l}(\boldsymbol{k}\cdot\vec{\eta})\rho_w + c.c. \\ &+ |\omega_n\eta^0/2+\boldsymbol{k}_l\cdot\vec{\eta}^*/2|^2\Big\} \\ &+ \frac{1}{L^2\beta}\sum_{ln}\left[\frac{2\pi J}{k^2}(-i\boldsymbol{k}\times\vec{\eta}^*)\cdot\hat{z}\rho_v + c.c.\right] \end{aligned} \tag{4.38}$$

Due to warps and vortices are completely decoupled, we could calculate the correlation function contributed from those two objects and spin wave separately and the final result will be the product of those three functions. So we write

$$C_{i\mu,j\nu} = C^v_{i\mu,j\nu}C^w_{i\mu,j\nu}C^{\rm sw}_{i\mu,j\nu} \tag{4.39}$$

with

$$\begin{aligned} C^v_{i\mu,j\nu} &= \frac{\int\mathcal{D}\theta \mathrm{e}^{-\bar{S}_w}}{\int\mathcal{D}\theta \mathrm{e}^{-S_w}}, \\ C^w_{i\mu,j\nu} &= \frac{\int\mathcal{D}\theta \mathrm{e}^{-\bar{S}_v}}{\int\mathcal{D}\theta \mathrm{e}^{-S_v}}, \\ C^{\rm sw}_{i\mu,j\nu} &= e^{-\frac{1}{L^2\beta}\sum_{ln}(2\pi J)G(\boldsymbol{k}_l,\omega_n)|\omega_n\eta^0/2+\boldsymbol{k}_l\cdot\vec{\eta}^*/2|^2} \end{aligned} \tag{4.40}$$

where

$$\begin{aligned}
\bar{S}_w &= S_w + \frac{1}{L^2\beta}\sum_{ln}(2\pi J)G(\boldsymbol{k}_l,\omega_n)\Big\{(-i\omega_n\eta^{0*}/2)(i\boldsymbol{k}_l\cdot\boldsymbol{m}) \\
&\quad + \frac{C+c\alpha k_l^2/\omega_n}{k_l}(\boldsymbol{k}\cdot\vec{\eta})\rho_w + c.c.\Big\} \\
\bar{S}_v &= S_v + \frac{1}{L^2\beta}\sum_{ln}\left[\frac{2\pi J}{k^2}(-i\boldsymbol{k}\times\vec{\eta}^*)\cdot\hat{z}\rho_v + c.c.\right]
\end{aligned} \tag{4.41}$$

The detail calculation of the correlation function can be found in the appendix, the final result is given in the following

$$\begin{aligned}
C_{i\mu,j\nu} &= \frac{c_0}{[1-\cos(2\pi\tau T)]^{1/2\alpha}}\left(\frac{a_c}{|\boldsymbol{r}_i-\boldsymbol{r}_j|}\right)^{-J^2y_v^2}\exp\Big(-2\pi T\sum_{n=1}^{+\infty}\frac{1-\cos(\omega_n\tau))}{|\omega_n|+(\alpha/4\pi\Delta_w)^{-1}}\Big) \\
&\times \exp\Big(-\int_{-\infty}^{\infty}\frac{d\omega}{2\pi}\int\frac{d\boldsymbol{k}}{(2\pi)^2}\frac{\mathrm{e}^{i\boldsymbol{k}\cdot\boldsymbol{r}-i\omega\tau}}{Jck^2+(C/c)\omega^2+\alpha|\omega|k^2}\Big)
\end{aligned} \tag{4.42}$$

# Chapter 5

# Effects of Anisotropic Fields in Dissipative Quantum 2+1D XY Model

## 5.1 Introduction

In the previous chapter, we show that the phase diagram of dissipative quantum 2+1D XY model will be reproduced by one loop renormalization group calculation. To derive the results, we introduced a scale-dependent dynamical critical exponent. To fully understand the quantum criticality for this model, we need include the symmetry breaking term, which arisen naturally in the loop current model to describe that loop current patterns can take one of the four possible configurations in the pseudogap region. In classical two dimensional XY model, such symmetry breaking terms has been studied[26]. Jose, et

al found that the four-fold symmetry-broken term is irrelevant in the fluctuation region but is highly relevant in the order state. In the two dimensional quantum XY model with dissipation, Aji [2, 3] proved that the four-fold anisotropy will only renormalize the dissipation strength $\alpha$ and change the position of the quantum critical point. Later, Lijun [63] used quantum Monte Carlo simulation to show that the four-fold anisotropic field will weakly change the position of quantum critical point but keep all the quantum criticality, such as separability of correlation function, scale-invariant fluctuation spectrum.

In this chapter, we will use renormalization group method to study the effect of the $p$-fold anisotropic fields. We will show that in the quantum critical region, the $p$-fold symmetry-broken fields will be relevant if the anisotropy exceed a certain strength. We will also demonstrate that, in the 2D limit, our results will go back to the results in two dimensional classical XY model with anisotropic fields.

## 5.2 Symmetry Breaking Term

We now analyze the effect of the anisotropy field on the local quantum-critical point in action (4.1). For the four-fold symmetry broken term, $p = 4$. To handle such a term in the action we use the following approximation:

$$e^{h_p \cos(p\theta_i)} \approx \sum_{q_i} e^{\ln(y_p) q_i^2 + ipq_i\theta_i}, \tag{5.1}$$

where $q_i$ is an integer field that lives at each site and $y_p = h_p/2$. For large value of $y_p$ the approximation is reliable as the sum will be dominated by the terms $q_i = 0, \pm 1$. Use the

same procedure by integrating out the phase variable, one could arrive the following action,

$$\begin{aligned} S = S_v + S_w + S'_w &+ \frac{1}{L^2\beta}\sum_{\omega,\boldsymbol{k}} Gc^2\left(2p\pi J\frac{k}{\omega}\rho_w(\boldsymbol{k},\omega)q(-\boldsymbol{k},-\omega) + p^2|q(\boldsymbol{k},\omega)|^2\right) \\ &+ \frac{1}{L^2\beta}\sum_{\omega,\boldsymbol{k}} \ln(y_p)|q(\boldsymbol{k},\omega)|^2, \end{aligned} \tag{5.2}$$

$S_v$, $S_w$, and $S'_w$ are given in 4.10. The symmetry broken term will introduce a new type of integer charge which is linearly coupled with warp. For convenient, we called this new charge as p-charge. In real space, this term can be written as

$$\begin{aligned} S_p &= \frac{c^2p^2}{4g}\sum_{i\neq j}\rho_q(\boldsymbol{r}_i,\tau_i)\frac{1}{\sqrt{|\boldsymbol{r}_i-\boldsymbol{r}_j|^2+v^2(\tau_i-\tau_j)^2}}\rho_q(\boldsymbol{r}_j,\tau_j) + \ln(y_p)\sum_i|\rho_q(\boldsymbol{r}_i,\tau_i)|^2 \\ &- \frac{icp}{2}\sum_{i\neq j}\rho_w(\boldsymbol{r}_i,\tau_i)\frac{sign(\tau_i-\tau_j)}{|\boldsymbol{r}_i-\boldsymbol{r}_j|}\rho_q(\boldsymbol{r}_j,\tau_j) \end{aligned} \tag{5.3}$$

The renormalization equations can be derived by following the same procedure as before, see appendix for more detail, we get

$$\begin{aligned} dy_p &= \left[d\ell_\tau + (2-\frac{c^2p^2}{4g})d\ell_r\right]y_p, \\ dg &= -\frac{8\pi^3}{3}\frac{g^2y_w^2}{vg^2\tau_c}\left[(\frac{1}{4}+\frac{v^2}{2})d\ell_\tau + (1+\frac{v^2}{3})d\ell_r\right] \\ &\quad +\frac{2\pi^3}{3}\frac{c^2p^2y_p^2}{v\tau_c}\left[(\frac{1}{4}+\frac{v^2}{2})d\ell_\tau + (1+\frac{v^2}{3})d\ell_r\right], \end{aligned} \tag{5.4}$$

the first term in $g$ comes from the Coulomb interaction for warps and the second term comes from the interaction between warps and p-charges. In the supplementary we also show there is a duality between warps and p-charges. This duality will leads to the scaling equation for $g$, which derived by Jose[26] for two dimensional XY model with anisotropy

fields. We have the following renormalization group equations for all coupling constants.

$$\begin{aligned}
d\alpha &= -2\alpha y_w^2 dl_\tau, \\
dg &= -\frac{8\pi^3}{3}\frac{g^2 y_w^2}{v\tau_c}\left[(\frac{1}{4}+\frac{v^2}{2v_c^2})dl_\tau + (1+\frac{v^2}{3v_c^2})dl_r\right] \\
&\quad +\frac{2\pi^3}{3}\frac{c^2p^2y_p^2}{v\tau_c}\left[(\frac{1}{4}+\frac{v^2}{2v_c^2})dl_\tau + (1+\frac{v^2}{3v_c^2})dl_r\right], \\
dy_w &= \left\{(1-\alpha)dl_\tau + (2-g)dl_r\right\}y_w, \\
dy_p &= \left\{dl_\tau + (2-\frac{c^2p^2}{4g})dl_r\right\}y_p, \\
dv &= (dl_\tau - dl_r)v, \\
dJ &= -\pi y_v^2 J^2 dl_r, \\
dy_v &= (2-\frac{J}{4\pi})y_v dl_r. \qquad (5.5)
\end{aligned}$$

Firstly, we notice that the scaling equation for velocity $v$ remain the same, which imply that the scaling equation for $z$ remain the same. Solve the equation $dz/d\ell_\tau = 0$ will give three fix points $z = 0, \infty$, and 1. Expanding around these fix points, one could easily verify that $z = 0$(2D limit) and $z = \infty$(1D limit) are unstable fix points and $z = 1$ is the stable fix point.

Secondly, if we change $h_p$ to $-h_p$ in the original action, the effective action will not change after integrating spin-wave fluctuations. This symmetry require that our renormalization equations also have this symmetry. One could easily check our renormalization equations satisfy this symmetry. This symmetry requirement also imply to first order calculation, the critical point will not change.

## 5.3 Properties near the quantum critical point

Near the quantum critical point $\alpha = 1$, the quantum dissipative XY model without anisotropic term is mainly control by the behavior of warps. The dynamical critical exponent will approach to infinity in this case. One could focus mainly on the renormalization group equations of warps and p-charges, which are given by

$$\begin{aligned}
\frac{d\alpha}{d\ell_\tau} &= -2\alpha y_w^2, \\
\frac{dy_w}{d\ell_\tau} &= y_w\left[(1-\alpha)+\frac{1}{z}(2-g)\right], \\
\frac{dy_p}{d\ell_\tau} &= \left[1+\frac{1}{z}(2-\frac{c^2p^2}{4g})\right]y_p, \\
\frac{dg}{d\ell_\tau} &= -\frac{8\pi^3}{3}\frac{g^2y_w^2}{\tau_c}f(v)+\frac{2\pi^3}{3}\frac{c^2p^2y_p^2}{\tau_c}f(v), \\
\frac{dv}{d\ell_\tau} &= (1-\frac{1}{z})v. \qquad (5.6)
\end{aligned}$$

where $f(v) = \frac{1}{4v}+\frac{v}{2v_c^2}+\frac{1}{vz}+\frac{v}{3v_c^2z}$. We will show later that $f(v) \sim v \sim \sqrt{z}$ near $z = \infty$ critical point. Expanding around the unstable fixed point $\alpha = 1^{-1}$, we still have $1/z = 0 + \tau^{-2}$. Therefore, $v = v_0 e^{\ell_\tau}$ for large $z$. This equality means $v \sim \tau \sim \sqrt{z}$. Setting $dg/d\ell_\tau = 0$, one could find four fix points (1). $y_w = 0, y_p = 0, g =$ constant, $\alpha =$ constant; (2). $y_w = \infty, y_p = 0, g = 0, \alpha = 0$; (3). $y_w = 0, y_p = \infty, g = \infty, \alpha =$ constant; (4). $gy_w = \frac{1}{2}cpy_p$. Expanding around these fix points, one could study the stability of the fix points. We will show that the first one is a unstable fix point, the second and third one are stable fix points, and the last one is a critical point.

### 5.3.1 Stability of $y_w = 0, y_p = 0, g = \textbf{constant}, \alpha = \textbf{constant}$

We expand around this fix point by writing $y_w = \delta y_w, y_p = \delta y_p, g = g^* + \delta g, \alpha = \alpha^* + \delta\alpha$. We have

$$\begin{aligned}
\frac{d\delta\alpha}{d\ell_\tau} &= -2\alpha^*\delta y_w^2, \\
\frac{d\delta y_w}{d\ell_\tau} &= (1 - \alpha^* - g^*/z)\delta y_w, \\
\frac{d\delta y_p}{d\ell_\tau} &= [1 - c^2p^2/(4zg^*)]\delta y_p, \\
\frac{d\delta g}{d\ell_\tau} &= \frac{8\pi^3}{3\tau_c}(-g^{*2}\delta y_w^2 + \frac{1}{4}c^2p^2\delta y_p^2)\sqrt{z}.
\end{aligned} \tag{5.7}$$

We substitute $f(v) \sim \sqrt{z}$ in the above equations. Notice $z \sim \tau^2$, we can simplify the above equations for $\delta y_w$ and $\delta y_p$ to get $d\delta y_w/d\ell_\tau = (1 - \alpha^*)\delta y_w$ and $d\delta y_p/d\ell_\tau = \delta y_p$. The second equation immediately tells us $y_p$ will flow away from 0 as $\delta y_p = e^{\ell_\tau} \sim \tau$. This proves that the fix point $y_w = 0, y_p = 0, g = \text{constant}, \alpha = \text{constant}$ is unstable.

### 5.3.2 Stability of $y_w = \infty, y_p = 0, g = 0, \alpha = 0$

Expanding around this fix point, we have $y_w^{-1} = \delta y_w, y_p = \delta y_p, g = \delta g, \alpha = \delta\alpha$. This expansion will lead to

$$\begin{aligned}
\frac{d\delta\alpha}{d\ell_\tau} &= -2\delta\alpha\delta y_w^{-2}, \\
\frac{d\delta y_w^{-1}}{d\ell_\tau} &= (1 - \delta\alpha - \delta g/z)\delta y_w^{-1}, \\
\frac{d\delta y_p}{d\ell_\tau} &= [1 - c^2p^2/(4z\delta g)]\delta y_p, \\
\frac{d\delta g}{d\ell_\tau} &= \frac{8\pi^3}{3\tau_c}(-\delta g^2\delta y_w^{-2} + \frac{1}{4}c^2p^2\delta y_p^2)\sqrt{z}.
\end{aligned} \tag{5.8}$$

We will show that this fix point is stable consistently as long as $gy_w > \frac{1}{2}cpy_p$ and $\alpha < 1$. If $gy_w > \frac{1}{2}cpy_p$ or $\delta g\delta y_w^{-1} > \frac{1}{2}cp\delta y_p$, the first term in $d\delta g$ will dominate. We will prove

that this inequality will always be satisfied as long as the initial condition does. Neglecting the second term, which we will show that the second term will approach to zero, we have $d\delta g/d\ell_\tau = -\frac{8\pi^3}{3\tau_c}\delta g^2 \delta y_w^{-2}\sqrt{z}$. As long as $\delta g \to 0$ and $\delta\alpha \to 0$, $\delta y_w^{-1}$ will also flow to $\infty$ as $\tau^1$. Therefore $d\delta g/d\ell_\tau \sim -\delta g^2\tau^3$ and this will lead $\delta g \sim \tau^{-3}$. As $\delta y_w^{-1} \to \infty$, $\delta\alpha$ will leads $\alpha$ flow to zero. Therefore, $\delta g \sim \tau^{-3}$ for large $\tau$. $z\delta g \sim \tau^{-1}$ will results in $d\delta y_p/d\ell_\tau \sim -c^2p^2\tau/4\delta y_p$. From this we see that $\delta y_p \to 0$ as $e^{-c^2p^2\tau/4}$, which is fast than $\delta g\delta y_w^{-1} \sim \tau^{-2}$. This discussion shows that $\delta g\delta y_w^{-1} > \frac{1}{2}c\delta y_p$ will always be satisfied along the flows. We conclude that $y_w = \infty, y_p = 0, g = 0, \alpha = 1$ is a stable fix point if $gy_w > \frac{1}{2}cpy_p$ and $\alpha < 1$.

### 5.3.3 Stability of $y_w = 0, y_p = \infty, g = \infty, \alpha =$ constant

We expand around this fix point by writing $y_w = \delta y_w, y_p^{-1} = \delta y_p, g^{-1} = \delta g, \alpha = \alpha^* + \delta\alpha$. We have

$$\begin{aligned}
\frac{d\delta\alpha}{d\ell_\tau} &= -2\alpha^*\delta y_w^{-2}, \\
\frac{d\delta y_w}{d\ell_\tau} &= (1-\alpha^* - \frac{1}{z\delta g})\delta y_w, \\
\frac{d\delta y_p^{-1}}{d\ell_\tau} &= [1 - c^2p^2\delta g/(4z)]\delta y_p^{-1}, \\
\frac{d\delta g^{-1}}{d\ell_\tau} &= \frac{8\pi^3}{3\tau_c}(-\delta g^{-2}\delta y_w^2 + \frac{1}{4}c^2p^2\delta y_p^{-2})\sqrt{z}.
\end{aligned} \tag{5.9}$$

We will demonstrate that this fix point will be stable if either $gy_w < \frac{1}{2}cpy_p$ and $\alpha < 1$ or $\alpha > 1$. We first prove the case for $\alpha > 1$. In this case, $\alpha^* > 1$. Therefore, $d\delta y_w/d\ell_\tau = -(\alpha^* - 1 + \frac{1}{z\delta g})\delta y_w$. From this equation, we immediately see that $\delta y_w$ flows to zero. The second term in $d\delta g^{-1}$ will dominate and we will show it does so consistently. Neglecting the first term, $d\delta g^{-1}/d\ell_\tau = \frac{2\pi^3}{3\tau_c}c^2p^2\delta y_p^{-2}\sqrt{z}$. Due to both $\delta g^{-1}$ and $z$ flow to zero, $d\delta y_p^{-1}/d\ell_\tau =$

$\delta y_p^{-1}$. Therefore, we have $\delta y_p^{-1} = e^{\ell_\tau} \sim \tau$. Plugging into the equation for $\delta g^{-1}$, we can see that $\delta g^{-1} \sim \tau^3$. From this, we solve the scaling equation for $\delta y_w$ and find that $\delta y_w \sim e^{-\tau}$. Therefore $\delta g^{-1} \delta y_w \sim \tau^3 e^{-\tau}$ flows to zero while $p\delta y_p^{-1} \sim \tau$ flows to infinity.

In the following, we will show that if $g y_w < \frac{1}{2} cpy_p$ and $\alpha < 1$, this fix point is also stable. We will assume $\delta g \to 0$ and will check this consistently. Following this, $\delta y_p^{-1} \sim \tau$. Under the initial condition $g y_w < \frac{1}{2} cpy_p$, we neglect the first term in $d\delta g^{-1}$ equation and find that $\delta g^{-1} \sim \tau^3$. Following this, $\delta y_w \sim e^{-\tau}$. Therefore the condition $\delta g^{-1} \delta y_w < \frac{1}{2} cp \delta y_p^{-1}$ will be satisfied due to the former goes to zero as $\tau^3 e^{-\tau}$ and the latter goes to infinity as $\tau$.

### 5.3.4 Summary of the flows near the quantum critical point

To summary, we find that the critical point is still $\alpha_c = 1$. For $\alpha < \alpha_c$, a new critical line $g y_w = \frac{1}{2} cpy_p$ arisen. When $\alpha < \alpha_c$, if $g y_w > \frac{1}{2} cpy_p$, the anisotropic fields will be irrelevant; on the other hand, if $g y_w < \frac{1}{2} cpy_p$, the anisotropic fields will be highly relevant. This condition could be understood in terms of bare parameter by noticing that $g = \frac{\sqrt{JC}}{4\pi}$, $y_w = e^{-\Delta_w \tau_c}$, and $y_p = h_p/2$. This critical line is then written as

$$\sqrt{JC} e^{-\Delta_w \tau_c} = \pi c p h_p \tag{5.10}$$

where $\Delta_w$ is the core energy of warps and is propotional to $\alpha$. For very large $h_p$, $h_p \cos(p\theta_i)$ will forces that the angle $\theta_i$ can only take one of the p different states. This will lead the ordered of warps. For small $h_p$, the warps are still favorable and the system will be in the quantum fluctuating regime and anisotropic fields are irrelevant.

For $\alpha > \alpha_c$, the warps will be in ordered state, which will driven the ordered of p-charges. Therefore, in the ordered phase, anisotropic fields are relevant.

In FIG.(5.1), we summary the above expansion analysis. The two critical lines $gy_w = \frac{1}{2}cpy_p$ and $\alpha = 1$ are represented by two dashed lines in the graph. We see from the graph that there are two stable fixed points, corresponding ordered of warps and ordered of p-charges. The quantum critical point $\alpha = 1$ is still unchanged under first order calculations for small $h_p$, while for large $h_p$ the quantum fluctuations will be effected.

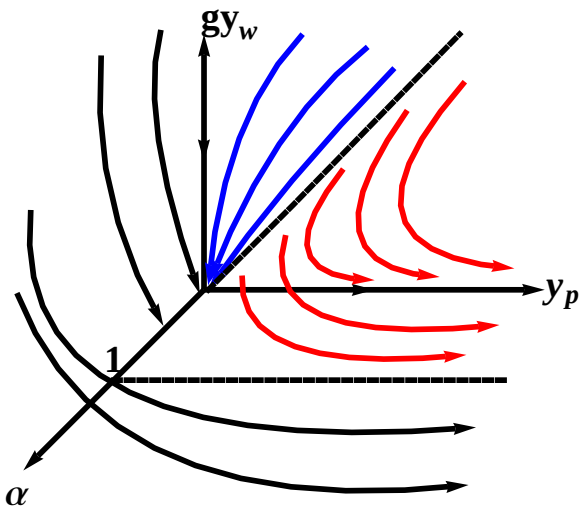


Figure 5.1: The sketch of the flow diagram based on the expansion around fix points near $z^* = \infty$. The two dashed lines represent the critical line $gy_w = \frac{1}{2}cpy_p$ and $\alpha = 1$, respectively.

## 5.4 Summary

From the above analysis, we see that the anisotropic fields will have different effects in dissipative quantum XY model. In the quantum fluctuation regime, small anisotropic fields will not change the quantum criticality, which is dominated by the fluctuation of

warps. But for large anisotropic fields, the quantum fluctuations will be destructed by the ordered of p-charges. In physics, this result is understood due to large symmetry breaking fields will lead the frozen of angle $\theta$. In turn, the frozen of the order parameter will induce the ordered of warps.

# Chapter 6

# Conclusions

The dissipative quantum XY model is first proposed [16, 20] to explain the superconductor to insulator transition in thin superconducting films. Later, the same model but with four-fold anisotropy has also been proposed as a model for the observed magnetic order in underdoped region of the cuprates and the fluctuation of such order in quantum critical region of cuprates[3, 2].

By using renormalization group methods and introducing running dynamical critical exponent to take the anisotropy of space and time into account, we solved the reformulated model of the 2D dissipative quantum XY model. The fixed points in the RG equations of this model corresponding exactly the three distinct phase in quantum Monte Carlo simulation. The quantum critical properties of the transition from disordered phase to ordered phase are studied by expanding the coupling constants near the unstable fixed point. We found the spacial correlation length has logarithmic relation with the temporal correlation function. We also proved that the quantum critical fluctuation can be separate in space

and time. The novel idea of running dynamical critical exponent is quite different with the Hertz-Millis-Moriya Theory by just choosing fixed dynamical critical exponent. The effects of symmetry breaking near quantum critical point have been examined. For small anisotropy fields, the quantum criticality remain the same, while the quantum fluctuations will be destructed for large anisotropy fields.

We also used quantum Monte Carlo simulation to study the transition from ordered phase to disordered phase and ordered phase by fixing $\alpha$, $K_\tau$, and changing $K$. The divergence of temporal correlation length as a function of $(K_c - K)/K_c$ is examined and the power of 0.5 0.6 is extracted from Monte Carlo simulation. Also, from the correlation function of different time and space, the relation of temporal correlation length and spacial correlation length is investigated. $\xi_r \sim \ln \xi_\tau$ is further confirmed through this direction of changing variable. We also found for different $x = 3$ and $x = 4$, $\xi_\tau(\tau, x)$ has the same relation of $(K_c - K)/K_c$ within the numerical uncertainty, this should prove that $\xi_\tau(\tau, x)$ is actually independent of $x$ and imply the separation of correlation function in space and time.

Through finite size scaling, we studied the scaling of static magnetic susceptibility for lattice size $N = 50$ and different $N_\tau$ range from 50 to 200. In terms of ultra-violet cutoff $\tau_c$, the temperature we are studying is from $0.02\tau_c$ to $0.005\tau_c$. If $\tau_c = 20K$, this numerical simulations are in the same temperature range as in experiment. From the simulation, we found that $\chi \sim T^{-1.4}$ which consistent with experiment and we also shown that the theoretical expression $T \log^2(T)$ could also fit the data equally well.

# Bibliography


[1] Vivek Aji, Yan He, and C. M. Varma. Magnetochiral kerr effect with application to the cuprates. *Phys. Rev. B*, 87:174518, May 2013.

[2] Vivek Aji and C. M. Varma. Theory of the quantum critical fluctuations in cuprate superconductors. *Phys. Rev. Lett.*, 99:067003, Aug 2007.

[3] Vivek Aji and C. M. Varma. Quantum criticality in dissipative quantum two-dimensional $xy$ and ashkin-teller models: Application to the cuprates. *Phys. Rev. B*, 79:184501, May 2009.

[4] A. Altland and B.D. Simons. *Condensed Matter Field Theory*. Cambridge books online. Cambridge University Press, 2010.

[5] P. W. Anderson, G. Yuval, and D. R. Hamann. Exact results in the kondo problem. ii. scaling theory, qualitatively correct solution, and some new results on one-dimensional classical statistical models. *Phys. Rev. B*, 1:4464–4473, Jun 1970.

[6] J. Ashkin and E. Teller. Statistics of two-dimensional lattices with four components. *Phys. Rev.*, 64:178–184, Sep 1943.

[7] V. Balédent, B. Fauqué, Y. Sidis, N. B. Christensen, S. Pailhès, K. Conder, E. Pomjakushina, J. Mesot, and P. Bourges. Two-dimensional orbital-like magnetic order in the high-temperature $la_{2-x}sr_xcuo_4$ superconductor. *Phys. Rev. Lett.*, 105:027004, Jul 2010.

[8] J. Bardeen, L. N. Cooper, and J. R. Schrieffer. Theory of superconductivity. *Phys. Rev.*, 108:1175–1204, Dec 1957.

[9] M. T. Béal-Monod and Kazumi Maki. Renormalizability of paramagnon theories. *Phys. Rev. Lett.*, 34:1461–1464, Jun 1975.

[10] J. G. Bednorz and K. A. Müller. Possible hightc superconductivity in the balacuo system. *Zeitschrift für Physik B Condensed Matter*, 64(2):189–193, 1986.

[11] D. Belitz, T. R. Kirkpatrick, and Thomas Vojta. How generic scale invariance influences quantum and classical phase transitions. *Rev. Mod. Phys.*, 77:579–632, Jul 2005.

[12] J. J. Binney, N. J. Dowrick, A. J. Fisher, and M. Newman. *The Theory of Critical Phenomena: An Introduction to the Renormalization Group*. Oxford University Press, Inc., New York, NY, USA, 1992.

[13] Jin Mo Bok, Jong Ju Bae, Han-Yong Choi, Chandra M. Varma, Wentao Zhang, Junfeng He, Yuxiao Zhang, Li Yu, and X. J. Zhou. Quantitative determination of pairing interactions for high-temperature superconductivity in cuprates. *Science Advances*, 2(3), 2016.

[14] Nicholas P. Breznay, Myles A. Steiner, Steven Allan Kivelson, and Aharon Kapitulnik. Self-duality and a hall-insulator phase near the superconductor-to-insulator transition in indium-oxide films. *Proceedings of the National Academy of Sciences*, 113(2):280–285, 2016.

[15] A.O Caldeira and A.J Leggett. Quantum tunnelling in a dissipative system. *Annals of Physics*, 149(2):374 – 456, 1983.

[16] Sudip Chakravarty, Gert-Ludwig Ingold, Steven Kivelson, and Alan Luther. Onset of global phase coherence in josephson-junction arrays: A dissipative phase transition. *Phys. Rev. Lett.*, 56:2303–2306, May 1986.

[17] Sudip Chakravarty, Gert-Ludwig Ingold, Steven Kivelson, and Gergely Zimanyi. Quantum statistical mechanics of an array of resistively shunted josephson junctions. *Phys. Rev. B*, 37:3283–3294, Mar 1988.

[18] B. Fauqué, Y. Sidis, V. Hinkov, S. Pailhès, C. T. Lin, X. Chaud, and P. Bourges. Magnetic order in the pseudogap phase of high-$T_C$ superconductors. *Phys. Rev. Lett.*, 96:197001, May 2006.

[19] Øystein Fischer, Martin Kugler, Ivan Maggio-Aprile, Christophe Berthod, and Christoph Renner. Scanning tunneling spectroscopy of high-temperature superconductors. *Rev. Mod. Phys.*, 79:353–419, Mar 2007.

[20] Matthew P. A. Fisher. Quantum phase slips and superconductivity in granular films. *Phys. Rev. Lett.*, 57:885–888, Aug 1986.

[21] W. M. C. Foulkes, L. Mitas, R. J. Needs, and G. Rajagopal. Quantum monte carlo simulations of solids. *Rev. Mod. Phys.*, 73:33–83, Jan 2001.

[22] M. Gurvitch and A. T. Fiory. Resistivity of $la_{1.825}sr_{0.175}cuo_4$ and $yba_2cu_3o_7$ to 1100 k: Absence of saturation and its implications. *Phys. Rev. Lett.*, 59:1337–1340, Sep 1987.

[23] M. Gurvitch, J. M. Valles, A. M. Cucolo, R. C. Dynes, J. P. Garno, L. F. Schneemeyer, and J. V. Waszczak. Reproducible tunneling data on chemically etched single crystals of $yba_2cu_3o_7$. *Phys. Rev. Lett.*, 63:1008–1011, Aug 1989.

[24] Rui-Hua He, M. Hashimoto, H. Karapetyan, J. D. Koralek, J. P. Hinton, J. P. Testaud, V. Nathan, Y. Yoshida, Hong Yao, K. Tanaka, W. Meevasana, R. G. Moore, D. H. Lu,

S.-K. Mo, M. Ishikado, H. Eisaki, Z. Hussain, T. P. Devereaux, S. A. Kivelson, J. Orenstein, A. Kapitulnik, and Z.-X. Shen. From a single-band metal to a high-temperature superconductor via two thermal phase transitions. *Science*, 331(6024):1579–1583, 2011.

[25] John A. Hertz. Quantum critical phenomena. *Phys. Rev. B*, 14:1165–1184, Aug 1976.

[26] Jorge V. José, Leo P. Kadanoff, Scott Kirkpatrick, and David R. Nelson. Renormalization, vortices, and symmetry-breaking perturbations in the two-dimensional planar model. *Phys. Rev. B*, 16:1217–1241, Aug 1977.

[27] L P Kadanoff. Lattice coulomb gas representations of two-dimensional problems. *Journal of Physics A: Mathematical and General*, 11(7):1399, 1978.

[28] A. Kaminski, S. Rosenkranz, H. M. Fretwell, J. C. Campuzano, Z. Li, H. Raffy, W. G. Cullen, H. You, C. G. Olson, C. M. Varma, and H. Hochst. Spontaneous breaking of time-reversal symmetry in the pseudogap state of a high-tc superconductor. *Nature*, 416(6881):610–613, 2002.

[29] H. Kammerlingh-Onnes. Onset of global phase coherence in josephson-junction arrays: A dissipative phase transition. *Comm. Phys. Lab. Univ. Leiden*, 56:120, June 1911.

[30] Steven Kivelson, Dung-Hai Lee, and Shou-Cheng Zhang. Global phase diagram in the quantum hall effect. *Phys. Rev. B*, 46:2223–2238, Jul 1992.

[31] J M Kosterlitz. The critical properties of the two-dimensional xy model. *Journal of Physics C: Solid State Physics*, 7(6):1046, 1974.

[32] J M Kosterlitz. The d-dimensional coulomb gas and the roughening transition. *Journal of Physics C: Solid State Physics*, 10(19):3753, 1977.

[33] David Landau and Kurt Binder. *A Guide to Monte Carlo Simulations in Statistical Physics*. Cambridge University Press, New York, NY, USA, 2005.

[34] Yuan Li, V. Baledent, G. Yu, N. Barisic, K. Hradil, R. A. Mole, Y. Sidis, P. Steffens, X. Zhao, P. Bourges, and M. Greven. Hidden magnetic excitation in the pseudogap phase of a high-tc superconductor. *Nature*, 468(7321):283–285, 11 2010.

[35] Yen-Hsiang Lin, J. Nelson, and A.M. Goldman. Superconductivity of very thin films: The superconductorinsulator transition. *Physica C: Superconductivity and its Applications*, 514:130 – 141, 2015.

[36] Hilbert v. Löhneysen, Achim Rosch, Matthias Vojta, and Peter Wölfle. Fermi-liquid instabilities at magnetic quantum phase transitions. *Rev. Mod. Phys.*, 79:1015–1075, Aug 2007.

[37] W. L. McMillan. Transition temperature of strong-coupled superconductors. *Phys. Rev.*, 167:331–344, Mar 1968.

[38] A. J. Millis. Effect of a nonzero temperature on quantum critical points in itinerant fermion systems. *Phys. Rev. B*, 48:7183–7196, Sep 1993.

[39] H. A. Mook, Pengcheng Dai, S. M. Hayden, A. Hiess, S-H Lee, and F. Dogan. Polarized neutron measurement of magnetic order in $yba_2cu_3o_{6.45}$. *Phys. Rev. B*, 69:134509, Apr 2004.

[40] T. Moriya and Y. Takahashi. SPIN FLUCTUATIONS IN ITINERANT ELECTRON MAGNETISM. *Journal de Physique Colloques*, 39(C6):C6–1466–C6–1471, 1978.

[41] N. Nagaosa. *Quantum Field Theory in Condensed Matter Physics*. Texts and monographs in physics. Springer, 1999.

[42] David R. Nelson and B. I. Halperin. Solid and fluid phases in smectic layers with tilted molecules. *Phys. Rev. B*, 21:5312–5329, Jun 1980.

[43] M. R. Norman, D. Pines, and C. Kallin. The pseudogap: friend or foe of high t c ? *Advances in Physics*, 54(8):715–733, 2005.

[44] M R Norman and C Ppin. The electronic nature of high temperature cuprate superconductors. *Reports on Progress in Physics*, 66(10):1547, 2003.

[45] A.M. Polyakov. Quark confinement and topology of gauge theories. *Nuclear Physics B*, 120(3):429 – 458, 1977.

[46] V. Privman. *Finite Size Scaling and Numerical Simulation of Statistical Systems*. Singapore: World Scientific, 1990.

[47] Myles A. Steiner, Nicholas P. Breznay, and Aharon Kapitulnik. Approach to a superconductor-to-bose-insulator transition in disordered films. *Phys. Rev. B*, 77:212501, Jun 2008.

[48] Einar B. Stiansen, Iver Bakken Sperstad, and Asle Sudbø. Three distinct types of quantum phase transitions in a (2+1)-dimensional array of dissipative josephson junctions. *Phys. Rev. B*, 85:224531, Jun 2012.

[49] G. A. Thomas, J. Orenstein, D. H. Rapkine, M. Capizzi, A. J. Millis, R. N. Bhatt, L. F. Schneemeyer, and J. V. Waszczak. $ba_2Ycu_3o_{7-\delta}$: Electrodynamics of crystals with high reflectivity. *Phys. Rev. Lett.*, 61:1313–1316, Sep 1988.

[50] Tom Timusk and Bryan Statt. The pseudogap in high-temperature superconductors: an experimental survey. *Reports on Progress in Physics*, 62(1):61, 1999.

[51] C. M. Varma. Non-fermi-liquid states and pairing instability of a general model of copper oxide metals. *Phys. Rev. B*, 55:14554–14580, Jun 1997.

[52] C. M. Varma. Pseudogap phase and the quantum-critical point in copper-oxide metals. *Phys. Rev. Lett.*, 83:3538–3541, Oct 1999.

[53] C. M. Varma. Theory of the pseudogap state of the cuprates. *Phys. Rev. B*, 73:155113, Apr 2006.

[54] C. M. Varma. Quantum criticality in quasi-two-dimensional itinerant antiferromagnets. *Phys. Rev. Lett.*, 115:186405, Oct 2015.

[55] C. M. Varma, P. B. Littlewood, S. Schmitt-Rink, E. Abrahams, and A. E. Ruckenstein. Phenomenology of the normal state of cu-o high-temperature superconductors. *Phys. Rev. Lett.*, 63:1996–1999, Oct 1989.

[56] Chandra Varma. High-temperature superconductivity: Mind the pseudogap. *Nature*, 468(7321):184–185, 11 2010.

[57] Villain, J. Theory of one- and two-dimensional magnets with an easy magnetization plane. ii. the planar, classical, two-dimensional magnet. *J. Phys. France*, 36(6):581–590, 1975.

[58] I M Vishik, W S Lee, R-H He, M Hashimoto, Z Hussain, T P Devereaux, and Z-X Shen. Arpes studies of cuprate fermiology: superconductivity, pseudogap and quasiparticle dynamics. *New Journal of Physics*, 12(10):105008, 2010.

[59] Wikipedia. Angle-resolved photoemission spectroscopy — wikipedia, the free encyclopedia, 2016. [Online; accessed 15-April-2016].

[60] Wikipedia. Quantum monte carlo — wikipedia, the free encyclopedia, 2016. [Online; accessed 16-April-2016].

[61] L. S. Wu, M. S. Kim, K. Park, A. M. Tsvelik, and M. C. Aronson. Quantum critical fluctuations in layered yfe2al10. *Proceedings of the National Academy of Sciences*, 111(39):14088–14093, 2014.

[62] Jing Xia, Elizabeth Schemm, G. Deutscher, S. A. Kivelson, D. A. Bonn, W. N. Hardy, R. Liang, W. Siemons, G. Koster, M. M. Fejer, and A. Kapitulnik. Polar kerr-effect measurements of the high-temperature $yba_2cu_3o_{6+x}$ superconductor: Evidence for broken symmetry near the pseudogap temperature. *Phys. Rev. Lett.*, 100:127002, Mar 2008.

[63] Lijun Zhu, Yan Chen, and Chandra M. Varma. Local quantum criticality in the two-dimensional dissipative quantum xy model. *Phys. Rev. B*, 91:205129, May 2015.

# Appendix A

# Derivation of the Renormalization Group Equations for Warps

Since warps and vortices are orthogonal objects, one may consider the partition function as the product of their partition functions. As in Eq. (**??**) of the text, the action for the warps, $S_w = S_w^0 + S_w'$ consists of two terms,

$$\begin{aligned} S_w &= \alpha \sum_{i \neq j} \rho_w(\boldsymbol{r}_i, \tau_i) \ln \frac{|\tau_i - \tau_j|}{\tau_c} \rho_w(\boldsymbol{r}_i, \tau_j) \delta(\boldsymbol{r}_i - \boldsymbol{r}_j), \\ S_w' &= -\frac{\sqrt{JC}}{4\pi} \sum_{i \neq j} \rho_w(\boldsymbol{r}_i, \tau_i) \frac{1}{\sqrt{v^2(\tau_i - \tau_j)^2 + |\boldsymbol{r}_i - \boldsymbol{r}_j|^2}} \rho_w(\boldsymbol{r}_j, \tau_j), \end{aligned} \tag{A.1}$$

where $v = \sqrt{\frac{Jc^2}{C}}$.

The partition function for warps is

$$\begin{aligned} Z &= \sum_n y_w^{2n} \int_{a_c}^{\infty} \frac{d^2 r_{2n}}{a_c^2} \cdots \int_{a_c}^{+\infty} \frac{d^2 r_1}{a_c^2} \int_0^{\beta} \frac{d\tau_{2n}}{\tau_c} \cdots \int_0^{\tau_2 - \tau_c} \frac{d\tau_1}{\tau_c} \\ &\times \sum_{\{\rho_w = \pm 1\}} \exp\Bigg[ \alpha \sum_{i \neq j} \int d^2 r_i \rho_w(\boldsymbol{r}_i, \tau_i) \ln \frac{|\tau_i - \tau_j|}{\tau_c} \delta(\boldsymbol{r}_i - \boldsymbol{r}_j) \rho_w(\boldsymbol{r}_j, \tau_j) \\ &+ g \sum_{i \neq j} \rho_w(\boldsymbol{r}_i, \tau_i) \frac{1}{\sqrt{v^2(\tau_i - \tau_j)^2 + |\boldsymbol{r}_i - \boldsymbol{r}_j|^2}} \rho_w(\boldsymbol{r}_j, \tau_j) \Bigg]. \end{aligned} \tag{A.2}$$

Here $y$ is the fugacity of the warps, and we have defined $y_w = y a_c^2 \tau_c$, and $g = \frac{\sqrt{JC}}{4\pi}$, and we have normalized the space and time integrals to diminsionless variables in terms of the lattice constant $a$ and the upper cut-off in time, $\tau_c$. We consider only $\rho_w(r, \tau) = \pm 1$, as higher charged warps are unimportant for low energy phenomena.

The first term in the partition function is much more singular than the second term. In the first term warps interact locally in space. We consider renormalization of interactions between a pair of warps due to a pair of virtual warps by summing over all possible interactions between the virtual pair and the others. The renormalized interactions

at longer and longer distances and longer and longer times are found by integrating over spatial scales increasing by $e^{d\ell_r}$ and time-scales increasing by $e^{d\ell_\tau}$. Let the warps be located at $(\boldsymbol{r}_i, \tau_i)$ and $(\boldsymbol{r}_j, \tau_j)$ with charge $\rho_w(\boldsymbol{r}_i, \tau_i) = +1$ and $\rho_w(\boldsymbol{r}_j, \tau_j) = -1$, respectively. The virtual warps pair have $\rho_w(\boldsymbol{r}', \tau') = +1$ and $\rho_w(\boldsymbol{r}'', \tau'') = -1$ and satisfy $a_c < |\boldsymbol{r}' - \boldsymbol{r}''| < a_c e^{dl_r}$ and $\tau_c < |\tau' - \tau''| < \tau_c e^{dl_\tau}$. Let $r_i = (\boldsymbol{r}_i, \tau_i)$ and define,

$$U(r_i, r_j) = \alpha\delta(\boldsymbol{r}_i - \boldsymbol{r}_j) \ln \frac{|\tau_i - \tau_j|}{\tau_c} + g\frac{1}{\sqrt{v^2(\tau_i - \tau_j)^2 + |\boldsymbol{r}_i - \boldsymbol{r}_j|^2}}, \tag{A.3}$$

The effective interaction of the pair of warps is given by

$$e^{-U_{\rm eff}(r_i, r_j)} = < e^{-U(r_i, r_j)} >|_{short} = e^{-U(r_i, r_j) - \delta U(r_i, r_j)}, \tag{A.4}$$

where the expectation value is the statistical average over the partition function in Eq.(A.2) over the integrated short scale.The second equality is due to the effective interaction can be written as the bare interaction plus the renormazed interaction after integrating the virtual pair. To lowest order in $y_w$, we have

$$\begin{aligned} e^{-\delta U(r_i, r_j)} &= \frac{1 + y_w^2 \int \frac{d^2r'}{a_c^2}\frac{d^2r''}{a_c^2}\int \frac{d\tau'}{\tau_c}\int \frac{d\tau''}{\tau_c} e^{-U(r', r'')} \mathrm{e}^{C(r_i, r_i; r', r'') + D(r_i, r_j; r', r'')} + O(y_w^4)}{1 + y_w^2 \int \frac{d^2r'}{a_c^2}\frac{d^2r''}{a_c^2}\int \frac{d\tau'}{\tau_c}\int \frac{d\tau''}{\tau_c} e^{-U(r', r'')} + O(y_w^4)} \\ &= 1 + y_w^2 \int \frac{d^2r'}{a_c}\frac{d^2r''}{a_c}\int \frac{d\tau'}{\tau_c}\int \frac{d\tau''}{\tau_c} e^{-U(r', r'')} \left[ e^{C(r_i, r_i; r', r'') + D(r_i, r_j; r', r'')} - 1 \right] \\ &+ O(y_w^4) \end{aligned} \tag{A.5}$$

where $C(r_i, r_i; r', r'')$ is the contribution from virtual pairs to the interaction of two warps at the same space site, $D(r_i, r_j; r', r'')$is the contribution from virtual pairs to the interaction of two warps at a different time and space site. We divide the term $C$ into five parts:(I).$\boldsymbol{r}_i = \boldsymbol{r}' = \boldsymbol{r}''$;(II).$\boldsymbol{r}_i \neq \boldsymbol{r}', \boldsymbol{r}' = \boldsymbol{r}''$;(III).$\boldsymbol{r}_i \neq \boldsymbol{r}' \neq \boldsymbol{r}''$;(IV).$\boldsymbol{r}_i = \boldsymbol{r}', \boldsymbol{r}' \neq \boldsymbol{r}''$;(V).$\boldsymbol{r}_i = \boldsymbol{r}'', \boldsymbol{r}' \neq \boldsymbol{r}''$. By summing over two possibilities of charge distribution of neutral warps pair, only the first two terms left. We then have

$$\begin{aligned} C_1 &= \left[\alpha \ln \frac{|\tau_i - \tau'|}{|\tau_i - \tau''|}\frac{|\tau_j - \tau''|}{|\tau_j - \tau'|}\right]\delta(\boldsymbol{r}' - \boldsymbol{r}'')\delta(\boldsymbol{r}_i - \boldsymbol{r}'), \\ C_2 &= \frac{g}{\sqrt{(\boldsymbol{r}_i - \boldsymbol{r}')^2 + v^2(\tau_i - \tau')^2}} - \frac{g}{\sqrt{(\boldsymbol{r}_i - \boldsymbol{r}'')^2 + v^2(\tau_i - \tau'')^2}} \\ &\quad - \frac{g}{\sqrt{(\boldsymbol{r}_i - \boldsymbol{r}')^2 + v^2(\tau_j - \tau')^2}} + \frac{g}{\sqrt{(\boldsymbol{r}_i - \boldsymbol{r}'')^2 + v^2(\tau_j - \tau'')^2}}. \end{aligned} \tag{A.6}$$

For $D$ term, we divide the whole space and time into nine piece:(I).$\boldsymbol{r}_i \neq \boldsymbol{r}' \neq \boldsymbol{r}'' \neq \boldsymbol{r}_j$;(II).$\boldsymbol{r}_i = \boldsymbol{r}' \neq \boldsymbol{r}'' \neq \boldsymbol{r}_j$;(III).$\boldsymbol{r}_i = \boldsymbol{r}'' \neq \boldsymbol{r}' \neq \boldsymbol{r}_j$;(IV).$\boldsymbol{r}_j = \boldsymbol{r}' \neq \boldsymbol{r}'' \neq \boldsymbol{r}_i$;(V).$\boldsymbol{r}_j = \boldsymbol{r}'' \neq \boldsymbol{r}' \neq \boldsymbol{r}_i$;(VI).$\boldsymbol{r}_i = \boldsymbol{r}' \neq \boldsymbol{r}'' = \boldsymbol{r}_j$;(VII).$\boldsymbol{r}_i = \boldsymbol{r}'' \neq \boldsymbol{r}' = \boldsymbol{r}_j$;(VIII).$\boldsymbol{r}_i = \boldsymbol{r}' = \boldsymbol{r}'' \neq \boldsymbol{r}_j$;(IX).$\boldsymbol{r}_j = \boldsymbol{r}' = \boldsymbol{r}'' \neq \boldsymbol{r}_i$. Following the same argument, by summing over all charge distribution of neutral pair, only the first term is non-zero.

$$\begin{aligned} D_1 &= \frac{g}{\sqrt{(\boldsymbol{r}_i - \boldsymbol{r}')^2 + v^2(\tau_i - \tau')^2}} - \frac{g}{\sqrt{(\boldsymbol{r}_i - \boldsymbol{r}'')^2 + v^2(\tau_i - \tau'')^2}} \\ &\quad - \frac{g}{\sqrt{(\boldsymbol{r}_j - \boldsymbol{r}')^2 + v^2(\tau_j - \tau')^2}} + \frac{g}{\sqrt{(\boldsymbol{r}_j - \boldsymbol{r}'')^2 + v^2(\tau_j - \tau'')^2}}. \end{aligned} \tag{A.7}$$

Now we evaluate them term by term. For $C_1$, we are trying to find the term proportion to $\ln\frac{\tau_j-\tau_i}{\tau_c}$, and for all $D$ terms we will separate the term proportion to $g/r$. Let us assume $\tau_i < \tau'' < \tau' < \tau_j$. So

$$\begin{aligned}\int\frac{d^2r'}{a_c^2}\frac{d^2r''}{a_c^2}\int\frac{d\tau'}{\tau_c}\frac{d\tau''}{\tau_c}C_1 &= \frac{dl_\tau}{a_c^4}\left[2\alpha\ln\frac{\tau_j-\tau_i}{\tau_c}\right],\\ \int\frac{d^2r'}{a_c^2}\frac{d^2r''}{a_c^2}\int\frac{d\tau'}{\tau_c}\frac{d\tau''}{\tau_c}C_2 &= -4\pi^2(dl_\tau+dl_r)\frac{g}{a_c^2}(\tau_j-\tau_i).\end{aligned} \tag{A.8}$$

and

$$J_1 = \int\frac{d^2r'}{a_c^2}\frac{d^2r''}{a_c^2}\int\frac{d\tau'}{\tau_c}\frac{d\tau''}{\tau_c}D_1 = -4\pi^2(dl_\tau+dl_r)\frac{g}{a_c^2}(\tau_j-\tau_i). \tag{A.9}$$

So, we have

$$\begin{aligned}e^{-\delta U(r_i,r_j)} &= 1+y_w^2\int\frac{d^2r'}{a_c}\frac{d^2r''}{a_c}\int\frac{d\tau'}{\tau_c}\int\frac{d\tau''}{\tau_c}\left[C_1+\frac{1}{2}D_1^2\right]\\ &= 1+2\alpha\frac{y_w^2}{a_c^4}dl_\tau\ln\frac{\tau_j-\tau_i}{\tau_c}+\frac{1}{2}y_w^2\int\frac{d^2r'}{a_c}\frac{d^2r''}{a_c}\int\frac{d\tau'}{\tau_c}\int\frac{d\tau''}{\tau_c}D_1^2\end{aligned} \tag{A.10}$$

Let

$$\begin{aligned}K &= \frac{1}{2}\int\frac{d^2r'}{a_c^2}\frac{d^2r''}{a_c^2}\int\frac{d\tau'}{\tau_c}\int\frac{d\tau''}{\tau_c}D_1^2\\ &= \frac{1}{2}g^2\int\frac{d^2R}{a_c^2}\int\frac{d^2r}{a_c^2}\int\frac{d\tau_s}{\tau_c}\int\frac{d\tau}{\tau_c}\left[\frac{[\boldsymbol{r}\cdot(\boldsymbol{r}_i-\boldsymbol{R})+v^2\tau(\tau_i-\tau_s)]^2}{[(\boldsymbol{r}_i-\boldsymbol{R})^2+v^2(\tau_i-\tau_s)^2]^3}\right.\\ &\quad+\frac{[\boldsymbol{r}\cdot(\boldsymbol{r}_j-\boldsymbol{R})+v^2\tau(\tau_j-\tau_s)]^2}{[(\boldsymbol{r}_j-\boldsymbol{R})^2+v^2(\tau_j-\tau_s)^2]^3}\\ &\quad\left.-2\frac{\boldsymbol{r}\cdot(\boldsymbol{r}_i-\boldsymbol{R})+v^2\tau(\tau_i-\tau_s)}{[(\boldsymbol{r}_i-\boldsymbol{R})^2+v^2(\tau_i-\tau_s)^2]^{3/2}}\frac{\boldsymbol{r}\cdot(\boldsymbol{r}_j-\boldsymbol{R})+v^2\tau(\tau_j-\tau_s)}{[(\boldsymbol{r}_j-\boldsymbol{R})^2+v^2(\tau_j-\tau_s)^2]^{3/2}}\right]\end{aligned} \tag{A.11}$$

where $\tau=\tau'-\tau''$ and $\tau_s=(\tau'+\tau'')/2$. By integrating out the coordinates of center of mass of the virtual pair and longer spatial and time scales, keep the term in order of $O(dl_r)$ and $O(dl_\tau)$, we arrive at

$$K = -\frac{8\pi^3}{3}\frac{g^2}{v\tau_c}\left[(\frac{1}{4}+\frac{v^2}{2v_c^2})dl_\tau+(1+\frac{v^2}{3v_c^2})dl_r\right]\frac{1}{\sqrt{(\boldsymbol{r}_i-\boldsymbol{r}_j)^2+v^2(\tau_i-\tau_j)^2}} \tag{A.12}$$

Combine all terms, we get

$$\begin{aligned}e^{-\delta U(r_i,r_j)} = 1 &+ y_w^2\left\{2\alpha\frac{dl_\tau}{a_c^4}\ln\frac{\tau_j-\tau_i}{\tau_c}-\frac{8\pi^3}{3}\frac{g^2}{v\tau_c}\left[(\frac{1}{4}+\frac{v^2}{2v_c^2})dl_\tau+(1+\frac{v^2}{3v_c^2})dl_r\right]\right.\\ &\times\left.\frac{1}{\sqrt{(\boldsymbol{r}_i-\boldsymbol{r}_j)^2+v^2(\tau_i-\tau_j)^2}}\right\}\end{aligned} \tag{A.13}$$

Re-exponentiate it, we get

$$e^{-U_{\rm eff}} = e^{-U(r_i,r_j)} e^{\left( 2y_w^2 dl_\tau \frac{\alpha}{a_c^4} \ln \frac{\tau_j-\tau_i}{\tau_c} - \frac{8\pi^3}{3}\frac{g^2}{v\tau_c}[(\frac{1}{4}+\frac{v^2}{2v_c^2})dl_\tau + (1+\frac{v^2}{3v_c^2})dl_r] \frac{1}{\sqrt{(\boldsymbol{r}_i-\boldsymbol{r}_j)^2+v^2(\tau_i-\tau_j)^2}} \right)} \tag{A.14}$$

So keeping logarithm correction we get

$$\begin{aligned} \widetilde{\alpha} &= \alpha - 2\alpha \frac{y_w^2}{a_c^4} dl_\tau, \\ \widetilde{g} &= g - \frac{8\pi^3}{3}\frac{g^2}{v\tau_c}\left[ (\frac{1}{4}+\frac{v^2}{2v_c^2})dl_\tau + (1+\frac{v^2}{3v_c^2})dl_r \right]. \end{aligned} \tag{A.15}$$

Now in our renormalized action, the short cutoff becomes $\tau_c e^{dl_\tau}$ and $a_c e^{dl_r}$.

$$\begin{aligned} Z_r &= \sum_n y_w^{2n} \int_{a_c e^{dl_r}}^{+\infty} \frac{d^2 r_{2n}}{a_c^2} \cdots \int_{a_c e^{dl_\tau}} \frac{d^2 r_1}{a_c^2} \int_0^\beta \frac{d\tau_{2n}}{\tau_c} \cdots \int_0^{\tau_2 - \tau_c e^{dl_\tau}} \frac{d\tau_1}{\tau_c} \\ &\times \sum_{\{\rho_w = \pm 1\}} \exp\left[ \widetilde{\alpha} \sum_{i\neq j} \int d^2 r_i \rho_w(\boldsymbol{r}_i,\tau_i) \ln \frac{|\tau_i-\tau_j|}{\tau_c} \delta(\boldsymbol{r}_i - \boldsymbol{r}_j) \rho_w(\boldsymbol{r}_j,\tau_j) \right. \\ &+ \left. \widetilde{g} \sum_{i\neq j} \rho_w(\boldsymbol{r}_i,\tau_i) \frac{1}{\sqrt{v^2(\tau_i-\tau_j)^2 + |\boldsymbol{r}_i-\boldsymbol{r}_j|^2}} \rho_w(\boldsymbol{r}_j,\tau_j) \right]. \end{aligned} \tag{A.16}$$

We need rescale $\boldsymbol{r} \to \boldsymbol{r} e^{-dl_r}$ and $\tau \to \tau e^{-dl_\tau}$ to get back the original action. Doing so we have

$$\begin{aligned} Z_r &= \sum_n y_w^{2n} e^{4ndl_r} e^{2ndl_\tau} \int_{a_c}^{+\infty} \frac{d^2 r_{2n}}{a_c^2} \cdots \int_{a_c} \frac{d^2 r_1}{a_c^2} \int_0^\beta \frac{d\tau_{2n}}{\tau_c} \cdots \int_0^{\tau_2-\tau_c} \frac{d\tau_1}{\tau_c} \\ &\sum_{\{\rho_w=\pm 1\}} \exp\left[ \widetilde{\alpha} \sum_{i\neq j} \int d^2 r_i \rho_w(\boldsymbol{r}_i,\tau_i) \ln \frac{|\tau_i-\tau_j| e^{dl_\tau}}{\tau_c} \delta(\boldsymbol{r}_i-\boldsymbol{r}_j) \rho_w(\boldsymbol{r}_j,\tau_j) \right. \\ &+ \left. \widetilde{g} \sum_{i\neq j} \rho_w(\boldsymbol{r}_i,\tau_i) \frac{e^{-dl_r}}{\sqrt{v^2 e^{2dl_\tau - 2dl_r}(\tau_i-\tau_j)^2 + |\boldsymbol{r}_i-\boldsymbol{r}_j|^2}} \rho_w(\boldsymbol{r}_j,\tau_j) \right]. \end{aligned} \tag{A.17}$$

This will contribute extra correction to $g$, $y_w$, and $v$

$$\begin{aligned} dg &= -g dl_r, \\ dy_w &= \left\{ (1-\alpha) dl_\tau + (2-g) dl_r \right\} y_w, \\ dv &= (dl_\tau - dl_r) v. \end{aligned} \tag{A.18}$$

Finally, we arrive our renormalization equations for warps by adding up the contribution from renormalization and rescaling

$$\begin{aligned} d\alpha &= -2\alpha\frac{y_w^2}{a_c^4}dl_\tau, \\ dg &= -gdl_r - \frac{8\pi^3}{3}\frac{g^2}{v\tau_c}\left[(\frac{1}{4}+\frac{v^2}{2v_c^2})dl_\tau + (1+\frac{v^2}{3v_c^2})dl_r\right], \\ dy_w &= \left\{(1-\alpha)dl_\tau + (2-g)dl_r\right\}y_w, \\ dv &= (dl_\tau - dl_r)v. \end{aligned} \tag{A.19}$$

# Appendix B

# Derivation of $C^{v}_{i\mu,j\nu}$

Follow the same procedure as we did in calculating the contribution from warps, we will get(to get the final result, there are some tricks need to be done, which can be found in the paper by Jose[26])

$$C^{v}_{i\mu,j\nu} = \exp\Big( - \frac{J^2}{2} a \ln \frac{|\boldsymbol{r}_i - \boldsymbol{r}_j|}{a_c} \Big) \tag{B.1}$$

where

$$a = \int_{a_c}^{+\infty} \frac{d\boldsymbol{r}}{a_c^2} \langle \rho_v(0)\rho_v(r)\rangle \tag{B.2}$$

$\langle \rho_v(0)\rho_v(r)\rangle$ is the correlation function of vortices and is defined with respect to the action of vortices, which is given by

$$\langle \rho_v(0)\rho_v(r)\rangle = -2y_v^2 \Big(\frac{r}{a_c}\Big)^{-J/2\pi} \tag{B.3}$$

so we get

$$C^{v}_{i\mu,j\nu} = (\frac{a_c}{|\boldsymbol{r}_i - \boldsymbol{r}_j|})^{-J^2 y_v^2} \tag{B.4}$$

# Appendix C

# Derivation of $C^{\mathbf{sw}}_{i\mu,j\nu}$

The contribution from spin wave can be calculated in the same way as the above. But we can derive it in a much more straight forward way by noticing that the action of spin wave is given by

$$S_{\rm sw} = \frac{1}{L^2\beta}\sum_{ln}((C/c)\omega_n^2 + Jck_l^2 + \alpha|\omega_n|k_l^2)\theta(\boldsymbol{k}_l,\omega_n)\theta(-\boldsymbol{k}_l,-\omega_n) \tag{C.1}$$

so

$$C^{\rm sw}_{i\mu,j\nu} = \langle {\rm e}^{i(\theta_{i\mu}-\theta_{j\nu})}\rangle_{\rm sw} = {\rm e}^{-\frac{1}{2}\langle\theta_{i\mu}\theta_{j\nu}\rangle_{\rm sw}} \tag{C.2}$$

Because the spin wave action is quadratic, we have

$$\begin{aligned}\langle\theta_{i\mu}\theta_{j\nu}\rangle_{\rm sw} &= \frac{1}{L^2\beta}\sum_{ln}\frac{{\rm e}^{i\boldsymbol{k}_l\cdot\boldsymbol{r}-i\omega_n\tau}}{Jck_l^2+(C/c)\omega_n^2+\alpha|\omega_n|k_l^2}\\ &= \int_{-\infty}^{\infty}\frac{d\omega}{2\pi}\int\frac{d\boldsymbol{k}}{(2\pi)^2}\frac{{\rm e}^{i\boldsymbol{k}\cdot\boldsymbol{r}-i\omega\tau}}{Jck^2+(C/c)\omega^2+\alpha|\omega|k^2}\end{aligned} \tag{C.3}$$

We use $\boldsymbol{r} = \boldsymbol{r}_i - \boldsymbol{r}_j$ and $\tau = \tau_\mu - \tau_\nu$ to simplify notation and we convert the summation into integration under the limit $T \to 0$. We have

$$C^{\rm sw}_{i\mu,j\nu} = {\rm e}^{-\int_{-\infty}^{\infty}\frac{d\omega}{2\pi}\int\frac{d\boldsymbol{k}}{(2\pi)^2}\frac{{\rm e}^{i\boldsymbol{k}\cdot\boldsymbol{r}-i\omega\tau}}{Jck^2+(C/c)\omega^2+\alpha|\omega|k^2}} \tag{C.4}$$

# Appendix D

# Fourier Transform of the Linear Coupling Term

The linear coupling term between warps and p-charges is given by

$$\frac{1}{L^2\beta}\sum_{\boldsymbol{k},\omega} Gc^2 2p\pi J\frac{k}{\omega}\rho_w(\boldsymbol{k},\omega)\rho_q(-\boldsymbol{k},-\omega) \tag{D.1}$$

where $G=\frac{1}{(C/c)\omega^2+Jck^2}$. The Fourier transformation of this coupling term is then given by

$$\begin{aligned}
\mathcal{G} &= \int\frac{d\omega}{2\pi}\int\frac{d^2k}{(2\pi)^2}\frac{c^2 2p\pi J}{(C/c)\omega^2+Jck^2}\frac{k}{\omega}e^{i\boldsymbol{k}\cdot\boldsymbol{r}-i\omega\tau}\\
&= \frac{ic^3p\pi J}{C}\mathrm{sign}(\tau)\int\frac{d^2k}{(2\pi)^2}\frac{1-e^{-vk|\tau|}}{v^2k}e^{i\boldsymbol{k}\cdot\boldsymbol{r}}\\
&= \frac{ic^3pJ}{2Cv^2}\mathrm{sign}(\tau)\int_0^{+\infty}dk(1-e^{-vk|\tau|})J_0(kr)\\
&= \frac{ic^3pJ}{2Cv^2}\mathrm{sign}(\tau)(\frac{1}{|\boldsymbol{r}|}-\frac{1}{\sqrt{r^2+v^2\tau^2}}) = \frac{icp}{2}\mathrm{sign}(\tau)(\frac{1}{|\boldsymbol{r}|}-\frac{1}{\sqrt{r^2+v^2\tau^2}})
\end{aligned} \tag{D.2}$$

where $v=\sqrt{Jc^2/C}$. To derivate the above equality, we used

$$\begin{aligned}
\int\frac{d\omega}{2\pi}\frac{1}{\omega^2+a^2}\frac{1}{\omega}e^{-i\omega\tau} &= \frac{i\mathrm{sign}(\tau)(1-e^{-a|\tau|})}{2a^2},\\
\int_0^{2\pi}dxe^{ia\cos(x)} &= 2\pi J_0(x),\\
\int_0^{+\infty}dxJ_0(x) &= 1,\\
\int_0^{\infty}dxe^{-ax}J_0(x) &= \frac{1}{\sqrt{1+a^2}}.
\end{aligned} \tag{D.3}$$

wherer $J_0(x)$ is the zeroth order Bessel function.

# Appendix E

# Derivation of the Renormalization Group Equations for Warps and p-Charges

Since there is no coupling between p-charges and vortices, one may consider renormalization of warps and p-charges together. The action for the warps and p-charges is given by,

$$\begin{aligned} S_{wp} &= \alpha \sum_{i\neq j} \rho_w(\boldsymbol{r}_i,\tau_i)\delta(\boldsymbol{r}_i-\boldsymbol{r}_j)\ln\frac{|\tau_i-\tau_j|}{\tau_c}\rho_w(\boldsymbol{r}_j,\tau_j) + \ln(y_w)\sum_i |\rho_w(\boldsymbol{r}_i,\tau_i)|^2 \\ &+ g\sum_{i\neq j}\rho_w(\boldsymbol{r}_i,\tau_i)\frac{1}{\sqrt{|\boldsymbol{r}_i-\boldsymbol{r}_j|^2+v^2(\tau_i-\tau_j)^2}}\rho_w(\boldsymbol{r}_j,\tau_j) \\ &+ \frac{c^2p^2}{4g}\sum_{i\neq j}\rho_q(\boldsymbol{r}_i,\tau_i)\frac{1}{\sqrt{|\boldsymbol{r}_i-\boldsymbol{r}_j|^2+v^2(\tau_i-\tau_j)^2}}\rho_q(\boldsymbol{r}_j,\tau_j) + \ln(y_p)\sum_i |\rho_q(\boldsymbol{r}_i,\tau_i)|^2 \\ &+ \frac{icp}{2}\sum_{i\neq j}\rho_w(\boldsymbol{r}_i,\tau_i)\left[\frac{sign(\tau_i-\tau_j)}{|\boldsymbol{r}_i-\boldsymbol{r}_j|} - \frac{sign(\tau_i-\tau_j)}{\sqrt{|\boldsymbol{r}_i-\boldsymbol{r}_j|^2+v^2(\tau_i-\tau_j)^2}}\right]\rho_q(\boldsymbol{r}_j,\tau_j) \quad \text{(E.1)} \end{aligned}$$

where $g=\frac{\sqrt{JC}}{4\pi}$, $v=\sqrt{\frac{Jc^2}{C}}$, $y_w$ and $y_p$ are fugacity of warps and p-charges which take into account the core-energy of the topological defects.

The first term in the partition function is much more singular than the other terms. In the first term warps interact locally in space. Follow the same procedure as in appendix A, we consider renormalization of interactions between a pair of warps due to a pair of virtual warps and p-charges by summing over all possible interactions between the virtual pairs and the others. The renormalized interactions at longer and longer distances and longer and longer times are found by integrating over spatial scales increasing by $e^{d\ell_r}$ and time-scales increasing by $e^{d\ell_\tau}$. Let the warps be located at $(\boldsymbol{r}_i,\tau_i)$ and $(\boldsymbol{r}_j,\tau_j)$ with charge $\rho_w(\boldsymbol{r}_i,\tau_i)=+1$ and $\rho_w(\boldsymbol{r}_j,\tau_j)=-1$, respectively. The virtual warps pair have $\rho_w(\boldsymbol{r}',\tau')=+1$ and $\rho_w(\boldsymbol{r}'',\tau'')=-1$, as well as the virtual p-charges pair, $\rho_q(\boldsymbol{r}',\tau')=+1$ and $\rho_q(\boldsymbol{r}'',\tau'')=-1$. Both of the warps pair and p-charges pair satisfy $a_c<|\boldsymbol{r}'-\boldsymbol{r}''|<a_c e^{dl_r}$

and $\tau_c < |\tau' - \tau''| < \tau_c e^{dl_\tau}$. Let $r_i = (\boldsymbol{r}_i, \tau_i)$ and define,

$$\begin{aligned} U^w(r_i, r_j) &= \alpha\delta(\boldsymbol{r}_i - \boldsymbol{r}_j) \ln \frac{|\tau_i - \tau_j|}{\tau_c} + g\frac{1}{\sqrt{v^2(\tau_i - \tau_j)^2 + |\boldsymbol{r}_i - \boldsymbol{r}_j|^2}}, \\ U^q(r_i, r_j) &= \frac{c^2p^2}{4g}\frac{1}{\sqrt{v^2(\tau_i - \tau_j)^2 + |\boldsymbol{r}_i - \boldsymbol{r}_j|^2}} \end{aligned} \tag{E.2}$$

The effective interaction of the pair of warps is given by

$$e^{-U^w_{\rm eff}(r_i,r_j)} = < e^{-U^w(r_i,r_j)} >|_{short} = e^{-U^w(r_i,r_j) - \delta U^w(r_i,r_j)}, \tag{E.3}$$

where the expectation value is the statistical average over the partition function over the integrated short scale.The second equality is due to the effective interaction can be written as the bare interaction plus the renormalazied interaction after integrating the virtual pair. To lowest order in $y_w$ and $y_p$, we have

$$\begin{aligned} e^{-\delta U^w(r_i,r_j)} &= \frac{1 + y_w^2 \int \frac{d^2r'}{a_c^2}\frac{d^2r''}{a_c^2}\int \frac{d\tau'}{\tau_c}\frac{d\tau''}{\tau_c} e^{-U^w(r',r'')} \mathrm{e}^{C(r_i,r_i;r',r'') + D(r_i,r_j;r',r'')}}{1 + y_w^2 \int \frac{d^2r'}{a_c^2}\frac{d^2r''}{a_c^2}\int \frac{d\tau'}{\tau_c}\frac{d\tau''}{\tau_c} e^{-U^w(r',r'')} + y_p^2 \int \frac{d^2r'}{a_c^2}\frac{d^2r''}{a_c^2}\int \frac{d\tau'}{\tau_c}\frac{d\tau''}{\tau_c} e^{-U^q(r',r'')}} \\ &+ \frac{y_p^2 \int \frac{d^2r'}{a_c^2}\frac{d^2r''}{a_c^2}\int \frac{d\tau'}{\tau_c}\frac{d\tau''}{\tau_c} e^{-U^q(r',r'')} \mathrm{e}^{E(r_i,r_j;r',r'')}}{1 + y_w^2 \int \frac{d^2r'}{a_c^2}\frac{d^2r''}{a_c^2}\int \frac{d\tau'}{\tau_c}\frac{d\tau''}{\tau_c} e^{-U^w(r',r'')} + y_p^2 \int \frac{d^2r'}{a_c^2}\frac{d^2r''}{a_c^2}\int \frac{d\tau'}{\tau_c}\frac{d\tau''}{\tau_c} e^{-U^q(r',r'')}} \\ &= 1 + y_w^2 \int \frac{d^2r'}{a_c^2}\frac{d^2r''}{a_c^2}\int \frac{d\tau'}{\tau_c}\int \frac{d\tau''}{\tau_c} e^{-U^w(r',r'')}\left[e^{C(r_i,r_i;r',r'') + D(r_i,r_j;r',r'')} - 1\right] \\ &+ y_p^2 \int \frac{d^2r'}{a_c^2}\frac{d^2r''}{a_c^2}\int \frac{d\tau'}{\tau_c}\int \frac{d\tau''}{\tau_c} e^{-U^q(r',r'')}\left[e^{E(r_i,r_j;r',r'')} - 1\right] \end{aligned} \tag{E.4}$$

where $C(r_i, r_i; r', r'')$ is the contribution from the virtual warps pair to the interaction of two warps at the same space site, $D(r_i, r_j; r', r'')$is the contribution from the virtual warps pair to the interaction of two warps at a different time and space site. $E(r_i, r_j; r', r'')$ is the contribution from the virtual p-charges pair to the interaction of two warps at a different time and space. We divide the term $C$ into five parts:(I).$\boldsymbol{r}_i = \boldsymbol{r}' = \boldsymbol{r}''$;(II).$\boldsymbol{r}_i \neq \boldsymbol{r}', \boldsymbol{r}' = \boldsymbol{r}''$;(III).$\boldsymbol{r}_i \neq \boldsymbol{r}' \neq \boldsymbol{r}''$;(IV).$\boldsymbol{r}_i = \boldsymbol{r}', \boldsymbol{r}' \neq \boldsymbol{r}''$;(V).$\boldsymbol{r}_i = \boldsymbol{r}'', \boldsymbol{r}' \neq \boldsymbol{r}''$. By summing over two possibilities of charge distribution of neutral warps pair, only the first two terms left. We then have

$$\begin{aligned} C_1 &= \left[\alpha \ln \frac{|\tau_i - \tau'|}{|\tau_i - \tau''|}\frac{|\tau_j - \tau''|}{|\tau_j - \tau'|}\right]\delta(\boldsymbol{r}' - \boldsymbol{r}'')\delta(\boldsymbol{r}_i - \boldsymbol{r}'), \\ C_2 &= \frac{g}{\sqrt{(\boldsymbol{r}_i - \boldsymbol{r}')^2 + v^2(\tau_i - \tau')^2}} - \frac{g}{\sqrt{(\boldsymbol{r}_i - \boldsymbol{r}'')^2 + v^2(\tau_i - \tau'')^2}} \\ &- \frac{g}{\sqrt{(\boldsymbol{r}_i - \boldsymbol{r}')^2 + v^2(\tau_j - \tau')^2}} + \frac{g}{\sqrt{(\boldsymbol{r}_i - \boldsymbol{r}'')^2 + v^2(\tau_j - \tau'')^2}}. \end{aligned} \tag{E.5}$$

For $D$ term, we divide the whole space and time into nine piece:(I).$\boldsymbol{r}_i \neq \boldsymbol{r}' \neq \boldsymbol{r}'' \neq \boldsymbol{r}_j$;(II).$\boldsymbol{r}_i = \boldsymbol{r}' \neq \boldsymbol{r}'' \neq \boldsymbol{r}_j$;(III).$\boldsymbol{r}_i = \boldsymbol{r}'' \neq \boldsymbol{r}' \neq \boldsymbol{r}_j$;(IV).$\boldsymbol{r}_j = \boldsymbol{r}' \neq \boldsymbol{r}'' \neq \boldsymbol{r}_i$;(V).$\boldsymbol{r}_j = \boldsymbol{r}'' \neq \boldsymbol{r}' \neq \boldsymbol{r}_i$;(VI).$\boldsymbol{r}_i = \boldsymbol{r}' \neq \boldsymbol{r}'' = \boldsymbol{r}_j$;(VII).$\boldsymbol{r}_i = \boldsymbol{r}'' \neq \boldsymbol{r}' = \boldsymbol{r}_j$;(VIII).$\boldsymbol{r}_i = \boldsymbol{r}' = \boldsymbol{r}'' \neq \boldsymbol{r}_j$;(IX).$\boldsymbol{r}_j = \boldsymbol{r}' =$

$\boldsymbol{r}'' \neq \boldsymbol{r}_i$. Following the same argument, by summing over all charge distribution of neutral pair, only the first term is non-zero.

$$\begin{aligned} D_1 = \quad & \frac{g}{\sqrt{(\boldsymbol{r}_i-\boldsymbol{r}')^2+v^2(\tau_i-\tau')^2}} - \frac{g}{\sqrt{(\boldsymbol{r}_i-\boldsymbol{r}'')^2+v^2(\tau_i-\tau'')^2}} \\ & -\frac{g}{\sqrt{(\boldsymbol{r}_j-\boldsymbol{r}')^2+v^2(\tau_j-\tau')^2}} + \frac{g}{\sqrt{(\boldsymbol{r}_j-\boldsymbol{r}'')^2+v^2(\tau_j-\tau'')^2}}. \end{aligned} \tag{E.6}$$

For the $E$ term, we have

$$\begin{aligned} E \;=\; & -\frac{icp}{2}\Big\{ \frac{\mathrm{sign}(\tau_i-\tau')}{|\boldsymbol{r}_i-\boldsymbol{r}'|} - \frac{\mathrm{sign}(\tau_i-\tau')}{\sqrt{|\boldsymbol{r}_i-\boldsymbol{r}'|^2+v^2(\tau_i-\tau')^2}} - \frac{\mathrm{sign}(\tau_i-\tau'')}{|\boldsymbol{r}_i-\boldsymbol{r}''|} \\ & + \frac{\mathrm{sign}(\tau_i-\tau'')}{\sqrt{|\boldsymbol{r}_i-\boldsymbol{r}''|^2+v^2(\tau_i-\tau'')^2}} - \frac{\mathrm{sign}(\tau_j-\tau')}{|\boldsymbol{r}_j-\boldsymbol{r}'|} + \frac{\mathrm{sign}(\tau_j-\tau')}{\sqrt{|\boldsymbol{r}_j-\boldsymbol{r}'|^2+v^2(\tau_j-\tau')^2}} \\ & + \frac{\mathrm{sign}(\tau_j-\tau'')}{|\boldsymbol{r}_j-\boldsymbol{r}''|} + \frac{\mathrm{sign}(\tau_j-\tau'')}{\sqrt{|\boldsymbol{r}_j-\boldsymbol{r}''|^2+v^2(\tau_j-\tau'')^2}} \Big\} \end{aligned} \tag{E.7}$$

The virtual p-charges pair is located in between the two warps, so $\tau_i < \tau', \tau'' < \tau_j$. The above expression can be simplified

$$\begin{aligned} E \;=\; & \frac{icp}{2}\Big\{ -\frac{1}{|\boldsymbol{r}_i-\boldsymbol{r}'|} + \frac{1}{\sqrt{|\boldsymbol{r}_i-\boldsymbol{r}'|^2+v^2(\tau_i-\tau')^2}} + \frac{1}{|\boldsymbol{r}_i-\boldsymbol{r}''|} \\ & - \frac{1}{\sqrt{|\boldsymbol{r}_i-\boldsymbol{r}''|^2+v^2(\tau_i-\tau'')^2}} - \frac{1}{|\boldsymbol{r}_j-\boldsymbol{r}'|} + \frac{1}{\sqrt{|\boldsymbol{r}_j-\boldsymbol{r}'|^2+v^2(\tau_j-\tau')^2}} \\ & + \frac{1}{|\boldsymbol{r}_j-\boldsymbol{r}''|} + \frac{1}{\sqrt{|\boldsymbol{r}_j-\boldsymbol{r}''|^2+v^2(\tau_j-\tau'')^2}} \Big\} \end{aligned} \tag{E.8}$$

The evaluation of $C$ and $D$ follow the same procedure as in appendix A. We focus on $E$ term due to the coupling between warps and p-charges. Defining the center of mass coordinate $\boldsymbol{R} = (\boldsymbol{r}' + \boldsymbol{r}'')/2$, $\boldsymbol{r} = \boldsymbol{r}' - \boldsymbol{r}''$, $\tau_s = (\tau' + \tau'')/2$ and $\tau = \tau' - \tau''$, we have

$$\begin{aligned} E \;=\; & \frac{icp}{2}\Big\{ -\frac{1}{|\boldsymbol{r}_i-\boldsymbol{R}-\boldsymbol{r}/2|} + \frac{1}{\sqrt{|\boldsymbol{r}_i-\boldsymbol{R}-\boldsymbol{r}/2|^2+v^2(\tau_i-\tau_s-\tau/2)^2}} \\ & + \frac{1}{|\boldsymbol{r}_i-\boldsymbol{R}+\boldsymbol{r}/2|} - \frac{1}{\sqrt{|\boldsymbol{r}_i-\boldsymbol{R}+\boldsymbol{r}/2|^2+v^2(\tau_i-\tau_s+\tau/2)^2}} \\ & - \frac{1}{|\boldsymbol{r}_j-\boldsymbol{R}-\boldsymbol{r}/2|} + \frac{1}{\sqrt{|\boldsymbol{r}_j-\boldsymbol{R}-\boldsymbol{r}/2|^2+v^2(\tau_j-\tau_s-\tau/2)^2}} \\ & + \frac{1}{|\boldsymbol{r}_j-\boldsymbol{R}+\boldsymbol{r}/2|} + \frac{1}{\sqrt{|\boldsymbol{r}_j-\boldsymbol{R}+\boldsymbol{r}/2|^2+v^2(\tau_j-\tau_s+\tau/2)^2}} \Big\} \end{aligned} \tag{E.9}$$

Due to $a_c < |\boldsymbol{r}| < a_c e^{dl_r}$ and $\tau_c < \tau < \tau_c e^{dl_\tau}$, we could expand for small $\boldsymbol{r}$ and $\tau$. Therefore we get,

$$\begin{aligned} E \;=\; & \frac{icp}{2}\Big\{ -\frac{\boldsymbol{r}\cdot(\boldsymbol{r}_i-\boldsymbol{R})}{|\boldsymbol{r}_i-\boldsymbol{R}|^3} + \frac{\boldsymbol{r}\cdot(\boldsymbol{r}_i-\boldsymbol{R}) + v^2\tau(\tau_i-\tau_s)}{[|\boldsymbol{r}_i-\boldsymbol{R}|^2+v^2(\tau_i-\tau_s)^2]^{3/2}} \\ & - \frac{\boldsymbol{r}\cdot(\boldsymbol{r}_j-\boldsymbol{R})}{|\boldsymbol{r}_j-\boldsymbol{R}|} + \frac{\boldsymbol{r}\cdot(\boldsymbol{r}_j-\boldsymbol{R}) + v^2\tau(\tau_j-\tau_s)}{[|\boldsymbol{r}_j-\boldsymbol{R}|^2+v^2(\tau_j-\tau_s)^2]^{3/2}} \Big\} \end{aligned} \tag{E.10}$$

Therefore the contribution to effective two warps interaction from p-charges is

$$\begin{aligned} J_p &= y_p^2 \int \frac{d^2r'}{a_c}\frac{d^2r''}{a_c}\int\frac{d\tau'}{\tau_c}\int\frac{d\tau''}{\tau_c}e^{-U^q(r',r'')}\left[e^{E(r_i,r_j;r',r'')}-1\right] \\ &= y_p^2 \int \frac{d^2R}{a_c}\frac{d^2r}{a_c}\int\frac{d\tau_s}{\tau_c}\int\frac{d\tau}{\tau_c}\left[E+\frac{1}{2}E^2\right], \end{aligned} \tag{E.11}$$

in which we transformed the integration to center of mass integration. The angle integration of $\boldsymbol{R}$ will immediately gives

$$y_p^2 \int \frac{d^2R}{a_c}\frac{d^2r}{a_c}\int\frac{d\tau_s}{\tau_c}\int\frac{d\tau}{\tau_c}E = 0 \tag{E.12}$$

Therefore we have

$$\begin{aligned} J_p &= \frac{y_p^2}{2} \int \frac{d^2R}{a_c^2}\frac{d^2r}{a_c^2}\int\frac{d\tau_s}{\tau_c}\int\frac{d\tau}{\tau_c}E^2 \\ &= -\frac{c^2p^2y_p^2}{4} \int \frac{d^2R}{a_c^2}\frac{d^2r}{a_c^2}\int\frac{d\tau_s}{\tau_c}\int\frac{d\tau}{\tau_c}\left[\frac{\boldsymbol{r}\cdot(\boldsymbol{r}_i-\boldsymbol{R})\boldsymbol{r}\cdot(\boldsymbol{r}_j-\boldsymbol{R})}{|\boldsymbol{r}_i-\boldsymbol{R}|^3|\boldsymbol{r}_j-\boldsymbol{R}|^3}\right. \\ &\quad \left.+\frac{[\boldsymbol{r}\cdot(\boldsymbol{r}_i-\boldsymbol{R})+v^2\tau(\tau_i-\tau_s)][\boldsymbol{r}\cdot(\boldsymbol{r}_j-\boldsymbol{R})+v^2\tau(\tau_j-\tau_s)]}{[|\boldsymbol{r}_i-\boldsymbol{R}|^2+v^2(\tau_i-\tau_s)^2]^{3/2}[|\boldsymbol{r}_j-\boldsymbol{R}|^2+v^2(\tau_j-\tau_s)^2]^{3/2}}\right] \end{aligned} \tag{E.13}$$

in which we used the angle integration of $\boldsymbol{R}$ is zero again. Let

$$\begin{aligned} I &= \int \frac{d^2R}{a_c^2}\frac{d^2r}{a_c^2}\int\frac{d\tau_s}{\tau_c}\int\frac{d\tau}{\tau_c}\frac{\boldsymbol{r}\cdot(\boldsymbol{r}_i-\boldsymbol{R})\boldsymbol{r}\cdot(\boldsymbol{r}_j-\boldsymbol{R})}{|\boldsymbol{r}_i-\boldsymbol{R}|^3|\boldsymbol{r}_j-\boldsymbol{R}|^3}, \\ K &= \int \frac{d^2R}{a_c^2}\int\frac{d^2r}{a_c^2}\int\frac{d\tau_s}{\tau_c}\int\frac{d\tau}{\tau_c}\left[\frac{\boldsymbol{r}\cdot(\boldsymbol{r}_i-\boldsymbol{R})+v^2\tau(\tau_i-\tau_s)}{[|\boldsymbol{r}_i-\boldsymbol{R}|^2+v^2(\tau_i-\tau_s)^2]^{3/2}}\right. \\ &\quad \left.\times\frac{\boldsymbol{r}\cdot(\boldsymbol{r}_j-\boldsymbol{R})+v^2\tau(\tau_j-\tau_s)}{[|\boldsymbol{r}_j-\boldsymbol{R}|^2+v^2(\tau_j-\tau_s)^2]^{3/2}}\right] \end{aligned} \tag{E.14}$$

Defining the center of mass of the warps $\boldsymbol{X} = (\boldsymbol{r}_i+\boldsymbol{r}_j)/2$, $\boldsymbol{x} = \boldsymbol{r}_i - \boldsymbol{r}_j$, $\tau_X = (\tau_i+\tau_j)/2$,

and $\tau_x = \tau_i - \tau_j$, we have

$$\begin{aligned}
I &= \int \frac{d^2R}{a_c^2}\frac{d^2r}{a_c^2}\int\frac{d\tau_s}{\tau_c}\int\frac{d\tau}{\tau_c}\frac{\boldsymbol{r}\cdot(\boldsymbol{X}-\boldsymbol{x}/2-\boldsymbol{R})\boldsymbol{r}\cdot(\boldsymbol{X}+\boldsymbol{x}/2-\boldsymbol{R})}{|\boldsymbol{X}-\boldsymbol{x}/2-\boldsymbol{R}|^3|\boldsymbol{X}+\boldsymbol{x}/2-\boldsymbol{R}|^3} \\
&= \int \frac{d^2R}{a_c^2}\frac{d^2r}{a_c^2}\int\frac{d\tau_s}{\tau_c}\int\frac{d\tau}{\tau_c}\frac{\boldsymbol{r}\cdot(\boldsymbol{R}+\boldsymbol{x}/2)\boldsymbol{r}\cdot(\boldsymbol{R}-\boldsymbol{x}/2)}{|\boldsymbol{R}+\boldsymbol{x}/2|^3|\boldsymbol{R}-\boldsymbol{x}/2|^3}, \\
K &= \int \frac{d^2R}{a_c^2}\int\frac{d^2r}{a_c^2}\int\frac{d\tau_s}{\tau_c}\int\frac{d\tau}{\tau_c}\left[\frac{\boldsymbol{r}\cdot(\boldsymbol{X}-\boldsymbol{x}/2-\boldsymbol{R})+v^2\tau(\tau_X-\tau_x/2-\tau_s)}{[|\boldsymbol{X}-\boldsymbol{x}/2-\boldsymbol{R}|^2+v^2(\tau_X-\tau_x/2-\tau_s)^2]^{3/2}}\right. \\
&\quad \left.\times\frac{\boldsymbol{r}\cdot(\boldsymbol{X}+\boldsymbol{x}/2-\boldsymbol{R})+v^2\tau(\tau_X+\tau_x/2-\tau_s)}{[|\boldsymbol{X}+\boldsymbol{x}/2-\boldsymbol{R}|^2+v^2(\tau_X+\tau_x/2-\tau_s)^2]^{3/2}}\right] \\
&= \int \frac{d^2R}{a_c^2}\int\frac{d^2r}{a_c^2}\int\frac{d\tau_s}{\tau_c}\int\frac{d\tau}{\tau_c}\left[\frac{\boldsymbol{r}\cdot(\boldsymbol{R}+\boldsymbol{x}/2)+v^2\tau(\tau_s+\tau_x/2)}{[|\boldsymbol{R}+\boldsymbol{x}/2|^2+v^2(\tau_s+\tau_x/2)^2]^{3/2}}\right. \\
&\quad \left.\times\frac{\boldsymbol{r}\cdot(\boldsymbol{R}-\boldsymbol{x}/2)+v^2\tau(\tau_s-\tau_x/2)}{[|\boldsymbol{R}-\boldsymbol{x}/2|^2+v^2(\tau_s-\tau_x/2)^2]^{3/2}}\right]
\end{aligned} \tag{E.15}$$

In the above, we changed variables $\boldsymbol{R}\to\boldsymbol{R}-\boldsymbol{X}$ and $\tau_s\to\tau_s-\tau_X$. The result for $K$ can be found in Appendix A, which is

$$K = \frac{8\pi^3}{3}\frac{1}{v\tau_c}\left[(\frac{1}{4}+\frac{v^2}{2v_c^2})dl_\tau + (1+\frac{v^2}{3v_c^2})dl_r\right]\frac{1}{\sqrt{(\boldsymbol{r}_i-\boldsymbol{r}_j)^2+v^2(\tau_i-\tau_j)^2}} \tag{E.16}$$

Carrying out the angle integration of $\boldsymbol{r}$ will leads to

$$I = \int_0^{+\infty}\frac{RdR}{a_c^2}\int_0^{2\pi}d\theta\int\frac{r^3dr}{a_c^4}\int\frac{d\tau_s}{\tau_c}\int\frac{d\tau}{\tau_c}\frac{R^2-x^2/4}{[(R^2+x^2/4)^2-R^2x^2\cos^2\theta]^{3/2}} \tag{E.17}$$

This integration turns to be zero by doing the $R$ integral first. In summary, we have

$$\begin{aligned}
e^{-\delta U^w(r_i,r_j)} &= 1+y_w^2\int\frac{d^2r'}{a_c^2}\frac{d^2r''}{a_c^2}\int\frac{d\tau'}{\tau_c}\int\frac{d\tau''}{\tau_c}\left[C_1+\frac{1}{2}D_1^2\right] \\
&\quad +\frac{y_p^2}{2}\int\frac{d^2R}{a_c^2}\frac{d^2r}{a_c^2}\int\frac{d\tau_s}{\tau_c}\int\frac{d\tau}{\tau_c}E^2 \\
&= 1+2\alpha\frac{y_w^2}{a_c^4}dl_\tau\ln\frac{\tau_j-\tau_i}{\tau_c}-\frac{8\pi^3}{3}\frac{g^2y_w^2}{v\tau_c}\left[(\frac{1}{4}+\frac{v^2}{2v_c^2})dl_\tau+(1+\frac{v^2}{3v_c^2})dl_r\right] \\
&\quad \times\frac{1}{\sqrt{(\boldsymbol{r}_i-\boldsymbol{r}_j)^2+v^2(\tau_i-\tau_j)^2}} \\
&\quad +\frac{2\pi^3c^2p^2}{3}\frac{y_p^2}{v\tau_c}\left[(\frac{1}{4}+\frac{v^2}{2v_c^2})dl_\tau+(1+\frac{v^2}{3v_c^2})dl_r\right]\frac{1}{\sqrt{(\boldsymbol{r}_i-\boldsymbol{r}_j)^2+v^2(\tau_i-\tau_j)^2}}
\end{aligned} \tag{E.18}$$

Re-exponentiate it, we get

$$
\begin{aligned}
e^{-U^w_{\rm eff}} &= e^{-U^w(r_i,r_j)} e^{\left(2y_w^2 dl_\tau \frac{\alpha}{a_c^4} \ln\frac{\tau_j-\tau_i}{\tau_c} - \frac{8\pi^3}{3}\frac{g^2y_w^2}{v\tau_c}[(\frac{1}{4}+\frac{v^2}{2v_c^2})dl_\tau+(1+\frac{v^2}{3v_c^2})dl_r]\frac{1}{\sqrt{(\boldsymbol{r}_i-\boldsymbol{r}_j)^2+v^2(\tau_i-\tau_j)^2}}\right)} \\
&\quad \times e^{\left(\frac{2\pi^3 c^2p^2}{3}\frac{y_p^2}{v\tau_c}\left[(\frac{1}{4}+\frac{v^2}{2v_c^2})dl_\tau+(1+\frac{v^2}{3v_c^2})dl_r\right]\frac{1}{\sqrt{(\boldsymbol{r}_i-\boldsymbol{r}_j)^2+v^2(\tau_i-\tau_j)^2}}\right)}
\end{aligned}
\tag{E.19}
$$

So keeping logarithm correction we get

$$
\begin{aligned}
\widetilde{\alpha} &= \alpha - 2\alpha\frac{y_w^2}{a_c^4}dl_\tau, \\
\widetilde{g} &= g - \frac{8\pi^3}{3}\frac{g^2y_w^2}{v\tau_c}\left[(\frac{1}{4}+\frac{v^2}{2v_c^2})dl_\tau+(1+\frac{v^2}{3v_c^2})dl_r\right] \\
&\quad +\frac{2\pi^3c^2p^2}{3}\frac{y_p^2}{v\tau_c}\left[(\frac{1}{4}+\frac{v^2}{2v_c^2})dl_\tau+(1+\frac{v^2}{3v_c^2})dl_r\right].
\end{aligned}
\tag{E.20}
$$

The effective interaction for p-charges can be calculated by following the same produce as above. Let the p-charges be located at $(\boldsymbol{r}_i,\tau_i)$ and $(\boldsymbol{r}_j,\tau_j)$ with charge $\rho_q(\boldsymbol{r}_i,\tau_i) = +1$ and $\rho_q(\boldsymbol{r}_j,\tau_j) = -1$, respectively. The virtual warps pair have $\rho_w(\boldsymbol{r}',\tau') = +1$ and $\rho_w(\boldsymbol{r}'',\tau'') = -1$, as well as the virtual p-charges pair, $\rho_q(\boldsymbol{r}',\tau') = +1$ and $\rho_q(\boldsymbol{r}'',\tau'') = -1$. Both of the warps pair and p-charges pair satisfy $a_c < |\boldsymbol{r}'-\boldsymbol{r}''| < a_c e^{dl_r}$ and $\tau_c < |\tau'-\tau''| < \tau_c e^{dl_\tau}$. The effective interaction of p-charges is given by

$$
e^{-U^p_{\rm eff}(r_i,r_j)} = < e^{-U^p(r_i,r_j)} >|_{short} = e^{-U^p(r_i,r_j)-\delta U^p(r_i,r_j)}.
\tag{E.21}
$$

To lowest order in $y_w$ and $y_p$, we have

$$
\begin{aligned}
e^{-\delta U^p(r_i,r_j)} &= \frac{1+y_w^2\int\frac{d^2r'}{a_c^2}\frac{d^2r''}{a_c^2}\int\frac{d\tau'}{\tau_c}\frac{d\tau''}{\tau_c}e^{-U^w(r',r'')}{\rm e}^{E(r_i,r_i;r',r'')}}{1+y_w^2\int\frac{d^2r'}{a_c^2}\frac{d^2r''}{a_c^2}\int\frac{d\tau'}{\tau_c}\frac{d\tau''}{\tau_c}e^{-U^w(r',r'')}+y_p^2\int\frac{d^2r'}{a_c^2}\frac{d^2r''}{a_c^2}\int\frac{d\tau'}{\tau_c}\frac{d\tau''}{\tau_c}e^{-U^q(r',r'')}} \\
&\quad +\frac{y_p^2\int\frac{d^2r'}{a_c^2}\frac{d^2r''}{a_c^2}\int\frac{d\tau'}{\tau_c}\frac{d\tau''}{\tau_c}e^{-U^q(r',r'')}{\rm e}^{D'(r_i,r_j;r',r'')}}{1+y_w^2\int\frac{d^2r'}{a_c^2}\frac{d^2r''}{a_c^2}\int\frac{d\tau'}{\tau_c}\frac{d\tau''}{\tau_c}e^{-U^w(r',r'')}+y_p^2\int\frac{d^2r'}{a_c^2}\frac{d^2r''}{a_c^2}\int\frac{d\tau'}{\tau_c}\frac{d\tau''}{\tau_c}e^{-U^q(r',r'')}} \\
&= 1+y_w^2\int\frac{d^2r'}{a_c^2}\frac{d^2r''}{a_c^2}\int\frac{d\tau'}{\tau_c}\int\frac{d\tau''}{\tau_c}e^{-U^w(r',r'')}\left[e^{E(r_i,r_i;r',r'')}-1\right] \\
&\quad +y_p^2\int\frac{d^2r'}{a_c^2}\frac{d^2r''}{a_c^2}\int\frac{d\tau'}{\tau_c}\int\frac{d\tau''}{\tau_c}e^{-U^q(r',r'')}\left[e^{D'(r_i,r_j;r',r'')}-1\right]
\end{aligned}
\tag{E.22}
$$

Following the same analysis before, we have

$$
\begin{aligned}
e^{-\delta U^p(r_i,r_j)} &= 1+\frac{y_w^2}{2}\int\frac{d^2r'}{a_c^2}\frac{d^2r''}{a_c^2}\int\frac{d\tau'}{\tau_c}\int\frac{d\tau''}{\tau_c}E^2(r_i,r_j;r',r'') \\
&\quad +\frac{y_p^2}{2}\int\frac{d^2r'}{a_c^2}\frac{d^2r''}{a_c^2}\int\frac{d\tau'}{\tau_c}\int\frac{d\tau''}{\tau_c}D'^2(r_i,r_j;r',r'')
\end{aligned}
\tag{E.23}
$$

with

$$D' = \frac{c^2p^2/4g}{\sqrt{(\boldsymbol{r}_i-\boldsymbol{r}')^2+v^2(\tau_i-\tau')^2}} - \frac{c^2p^2/4g}{\sqrt{(\boldsymbol{r}_i-\boldsymbol{r}'')^2+v^2(\tau_i-\tau'')^2}} - \frac{c^2p^2/4g}{\sqrt{(\boldsymbol{r}_j-\boldsymbol{r}')^2+v^2(\tau_j-\tau')^2}} + \frac{c^2p^2/4g}{\sqrt{(\boldsymbol{r}_j-\boldsymbol{r}'')^2+v^2(\tau_j-\tau'')^2}}. \quad \text{(E.24)}$$

Define the center of mass of the virtual p-charges pair, $\boldsymbol{R} = (\boldsymbol{r}'+\boldsymbol{r}'')/2$, $\boldsymbol{r} = \boldsymbol{r}'-\boldsymbol{r}''$, $\tau_s = (\tau'+\tau'')/2$ and $\tau = \tau'-\tau''$ and integrating the center of mass coordinates, we will have

$$e^{-\delta U^p(r_i,r_j)} = 1 - \frac{\pi^3}{6}\frac{c^4p^4y_p^2}{vg^2\tau_c}\left[(\frac{1}{4}+\frac{v^2}{2v_c^2})dl_\tau + (1+\frac{v^2}{3v_c^2})dl_r\right]\frac{1}{\sqrt{(\boldsymbol{r}_i-\boldsymbol{r}_j)^2+v^2(\tau_i-\tau_j)^2}} + \frac{2\pi^3}{3}\frac{c^2p^2y_w^2}{v\tau_c}\left[(\frac{1}{4}+\frac{v^2}{2v_c^2})dl_\tau + (1+\frac{v^2}{3v_c^2})dl_r\right]\frac{1}{\sqrt{(\boldsymbol{r}_i-\boldsymbol{r}_j)^2+v^2(\tau_i-\tau_j)^2}} \quad \text{(E.25)}$$

Re-exponentiate it, we get

$$e^{-U^p_{\text{eff}}} = e^{-U^p(r_i,r_j)}e^{\left(-\frac{\pi^3}{6}\frac{c^4p^4y_p^2}{vg^2\tau_c}[(\frac{1}{4}+\frac{v^2}{2v_c^2})dl_\tau+(1+\frac{v^2}{3v_c^2})dl_r]\frac{1}{\sqrt{(\boldsymbol{r}_i-\boldsymbol{r}_j)^2+v^2(\tau_i-\tau_j)^2}}\right)} \times e^{\left(\frac{2\pi^3}{3}\frac{c^2p^2y_w^2}{v\tau_c}[(\frac{1}{4}+\frac{v^2}{2v_c^2})dl_\tau+(1+\frac{v^2}{3v_c^2})dl_r]\frac{1}{\sqrt{(\boldsymbol{r}_i-\boldsymbol{r}_j)^2+v^2(\tau_i-\tau_j)^2}}\right)} \quad \text{(E.26)}$$

So keeping logarithm correction we get

$$\widetilde{g^{-1}} = g^{-1} - \frac{2\pi^3}{3}\frac{c^2p^2y_p^2}{vg^2\tau_c}\left[(\frac{1}{4}+\frac{v^2}{2v_c^2})dl_\tau + (1+\frac{v^2}{3v_c^2})dl_r\right] + \frac{8\pi^3}{3}\frac{y_w^2}{v\tau_c}[(\frac{1}{4}+\frac{v^2}{2v_c^2})dl_\tau + (1+\frac{v^2}{3v_c^2})dl_r]. \quad \text{(E.27)}$$

This equation is exactly the same as we got by consider the effective interaction for warps. This should be due to the duality in the warps and p-charges problem. Considering $y_p \to y_w$, $y_w \to y_p$, and $g \to \frac{c^2p^2}{4g}$, the action for warps and p-charges remain the same. Therefore, one do not need to introduce a new coupling constant for $1/g$ which is required for general problems. This duality is first derived by Jose et al [26]. Later, a general model has been considered by Kadanoff[27]. Nelson et al [42] also proved such duality in a special problem, see (A27) in [42].

Now in our renormalized action, the short cutoff becomes $\tau_c e^{dl_\tau}$ and $a_c e^{dl_r}$. We need rescale $\boldsymbol{r} \to \boldsymbol{r}e^{-dl_r}$ and $\tau \to \tau e^{-dl_\tau}$ to get back the original action. Doing so we will

get extra contributions to coupling constants $g$, $y_w$, $y_p$, $v$, and $g^{-1}$,

$$\begin{aligned} dg &= -g dl_r, \\ dg^{-1} &= -g^{-1} dl_r, \\ dy_w &= \left\{ (1-\alpha) dl_\tau + (2-g) dl_r \right\} y_w, \\ dy_p &= \left\{ dl_\tau + (2 - \frac{p^2}{4g}) dl_r \right\} y_p d, \\ dv &= (dl_\tau - dl_r) v. \end{aligned} \tag{E.28}$$

Finally, we arrive our renormalization equations for warps and p-charges by adding up the contribution from renormalization and rescaling,

$$\begin{aligned} d\alpha &= -2\alpha \frac{y_w^2}{a_c^4} dl_\tau, \\ dg &= -\frac{8\pi^3}{3} \frac{g^2}{v\tau_c} \left[ (\frac{1}{4} + \frac{v^2}{2v_c^2}) dl_\tau + (1 + \frac{v^2}{3v_c^2}) dl_r \right] \\ &\quad + \frac{2\pi^3}{3} \frac{c^2 p^2}{v g^2 \tau_c} \left[ (\frac{1}{4} + \frac{v^2}{2v_c^2}) dl_\tau + (1 + \frac{v^2}{3v_c^2}) dl_r \right], \\ dy_w &= \left\{ (1-\alpha) dl_\tau + (2-g) dl_r \right\} y_w, \\ dy_p &= (2 - \frac{c^2 p^2}{4g}) y_p dl_r, \\ dv &= (dl_\tau - dl_r) v. \end{aligned} \tag{E.29}$$